MODELING AND MEASUREMENT OF A NEUTRON GENERATOR DRIVEN SUB-CRITICAL ASSEMBLY USED FOR ISOTOPE PRODUCTION

A Thesis

by

MATTHEW ALEXANDER BOYD

Submitted to the Office of Graduate and Professional Studies of
Texas A&M University
in partial fulfillment of the requirements for the degree of

MASTER OF SCIENCE

Chair of Committee,	Craig Marianno
Committee Members,	John Ford
	Marvin Adams
	Charles M. Folden III
Head of Department,	Michael Nastasi

December 2020

Major Subject: Nuclear Engineering

ABSTRACT

The primary objective of this research was to provide a validated model of Global Medical Isotope Systems' (GMIS) sub-critical assembly used for isotope production. This model would provide estimates of dose calculations, radioisotope production rates, and neutron flux and energy spectrum

A system model was constructed using Monte Carlo N Particle Version 6.1 (MCNP). An initial MCNP model replicated lithium irradiations for tritium production GMIS performed in 2016. MCNP estimated a production rate of 2.259±0.021 Bq g^{-1} h^{-1} compared to GMIS' reported rate of 1.48-1.96 MBq g^{-1} h^{-1}. Exterior dose measurements were performed to provide initial validation of the MCNP model. The MCNP model and empirical dose agreed within 1σ error for three of five measurements; the other two agreed within a factor of 2. Further validation work was performed using activation wires and the neutron unfolding code SAND-II. The planned series of measurements was cut short by equipment failure and system decommissioning limiting available data. Integral fluxes from MCNP and SAND-II agreed within 20% for three of four cases, the fourth differed by a factor of 2.

Using the MCNP model, the subcritical multiplication factor was calculated to be 0.25430 ± 0.00090 corresponding to a system power of 9.78 ± 0.05 mW at standard operating parameters. This corresponds to a total 7 day ^{99}Mo activity production of 11.70±0.02 MBq. This indicates that the system is not a viable method for producing the isotopes of interest as currently designed.

ACKNOWLEDGEMENTS

I'd like to thank my advisor Dr. Craig Marianno for his continuing patience and support during this project and my graduate studies. Dr. Ray Keegan was invaluable to this research and provided reliable voice of sanity during data analysis. Dr. Glenn Scheitrum provided an excellent example of some of the best qualities of an American Engineer, including his willingness to teach a clueless graduate student how to weld.

To my family and friends, without whom this would have been impossible.

Thank You.

CONTRIBUTORS AND FUNDING SOURCES

Contributors

This work was supervised by a thesis committee consisting of Professor Craig Marianno [advisor], Professor Marvin Adams, and Professor John Ford of the Department of Nuclear Engineering and Professor Charles M. Folden III of the Department of Chemistry.

Dr. Francis Tsang provided general information on the GMIS system and initial estimates of neutron flux and isotope production rates. The detailed SolidWorks model of the system discussed in Chapter 2 was provided by Dr. Glenn Scheitrum. The lithium irradiation and liquid scintillation measurements referenced in Chapter 3 were performed by Dr. Francis Tsang and Dr. Edward Masoulf. Dr. Raymond Keegan was instrumental in the foil activation work in Chapter 3 as the administratively required second operator. He provided invaluable assistance with sample preparation, gamma spectroscopy measurements, initial installation and operation of the SANDII code, and performing the sample irradiations. Other members of the GMIS science team included Dr. Zane Wilson, Dr. Erik Johnstone, and Arabelle Campo.

All other work conducted for the thesis was completed by the student independently.

Funding Sources

Graduate study was supported by funding from Dr. Craig Marianno from Texas A&M University and GMIS.

NOMENCLATURE

BHDPE	Borated High Density Polyethylene (5% B)
CTO	Chief Technical Officer
D-D	Deuterium Deuterium Fusion
D-T	Deuterium Tritium Fusion
DU	Depleted Uranium ($^{235}U \leq .0.7\%.$)
FWHM	Full Width at Half Maximum
GAO	Government Accountability Office
GMIS	Global Medical Isotope Systems
HDPE	High Density Polethylene
HEU	Highly Enriched Uranium ($^{235}U \geq 20\%$)
LET	Linear Energy Transfer
LEU	Low Enriched Uranium ($^{235}U \leq 20\%$)
MDA	Minimum Detectable Activity
MCNP	Monte Carlo N Particle Code
MSTS	Mission Support and Test Services, LLC
NNSA	National Nuclear Security Administration
NNSS	Nevada National Security Site
NORM	Naturally Occurring Radioactive Materials
NU	Natural Uranium ($^{235}U=0.7\%$)
SRIM	Stopping Range Ions in Matter

TABLE OF CONTENTS

Page

ABSTRACT ii

ACKNOWLEDGEMENTS iii

CONTRIBUTORS AND FUNDING SOURCES iv

NOMENCLATURE v

TABLE OF CONTENTS vi

LIST OF FIGURES viii

LIST OF TABLES x

1. INTRODUCTION 1

2. BACKGROUND 4

2.1. Prototype System Description 4
2.1.1. Physical Description 4
2.1.2. Neutron Generators 11
2.1.3. GMIS Reported Parameters 13
2.2. Sub-Critical Multiplication 14
2.3. Monte Carlo Methods 18
2.3.1. MCNP 18
2.3.2. MCNP Tallies 20
2.3.3. Variance Reduction Techniques 21
2.3.4. MCNP outputs 24
2.4. Foil Activation 25
2.4.1. Theory 25
2.4.2. Unfolding Code 28

3. METHODOLOGY 31

3.1. MCNP Model Development 31
3.1.1. Lithium Irradiation 31
3.1.2. Exterior Dose Measurements 34
3.2. Activation wires 38

3.2.1. Foil Selection 39
3.2.2. Irradiation Measurement Campaign 44
3.2.3. Neutron Generator Yield Calculations 56
3.2.4. MCNP Model Wire Activation 58
3.2.5. MCNP Source Efficiency 60

4. RESULTS 62

4.1. Wire Spectroscopy and Saturated Activity Results 62
4.2. MCNP Reaction Rate Results 71
4.3. Unfolded Neutron Energy Spectra 73
4.4. Source Efficiency, System Power, and ^{99}Mo production 83

5. CONCLUSIONS 88

REFERENCES 90

APPENDIX A SAMPLE MCNP CODE 93

APPENDIX B ADDITIONAL ACTIVATION WIRE SPECTRA 108

LIST OF FIGURES

Page

Figure 2.1 SolidWorks Model of the GMIS Prototype. 5

Figure 2.2 Model of a DD-108 neutron generator with labeled major components. 7

Figure 2.3 Photograph of the GMIS neutron generator and support features in shielding enclosure. 8

Figure 2.4 Photograph of the uranium target boxes and reflectors surrounding the neutron generator within the shielding enclosure. 9

Figure 2.5 Positions of uranium target boxes. 10

Figure 2.6 : D-D and D-T fusion reaction cross-sections [mb] versus energy [keV] 12

Figure 2.7 Particle history for neutron incident on fissionable slab [*18*] 19

Figure 3.1 Vertical and horizontal cuts of the MCNP model. 33

Figure 3.2 Planned activation measurement campaign irradiation sites. 45

Figure 3.3 HPGE efficiency curve from a 118800 s calibration using a 34.66 kBq ^{152}Eu source in contact with the center of the detector endcap. 50

Figure 3.4 Sample calibration and background spectra taken on 6 December 2018 50

Figure 3.5 Estimated target D-D neutron yield. 58

Figure 4.1 Activated Co wire spectra on 23 February 2018 after 160 min irradiation at position 1 in full cavity. 63

Figure 4.2 Activated Al and In wire spectra on 23 February 2018 after 270 min irradiation at position 1 in full cavity. 64

Figure 4.3 Bare Dy-Al and Mn wire spectra on 26 February 2018 after 160 min irradiation at position 1 in full cavity. 65

Figure 4.4 Cd(Dy-Al) and bare Mn wire spectra on 26 February 2018 after 160 min irradiation at position 1 in full cavity. 66

Figure 4.5 SANDII-SNL unfolded neutron spectra. The position 1 wires are shown in blue, position 2 wires are shown in orange, empty cavity lines are dashed, and uranium cavity lines are solid. 74

Figure 4.6 MCNP neutron flux spectra for system with DU target boxes. 76

Figure 4.7 MCNP neutron flux spectra for empty cavity system. 76

Figure 4.8 Combined MCNP neutron flux spectra for empty (dashed) and full (solid) cavity. Position 1 is plotted in blue. Position 2 is plotted in orange. 77

Figure 4.9 MCNP and SANDII neutron flux spectra for full cavity at position 1.MCNP is in blue; SANDII is in red. 80

Figure 4.10 MCNP and SANDII neutron flux spectra for full cavity at position 2. MCNP is in orange, SANDII is in magenta. 80

Figure 4.11 MCNP and SANDII neutron flux spectra for empty cavity at position 1. MCNP is in blue; SANDII is in Red. 81

Figure 4.12 MCNP and SANDII neutron flux spectra for empty cavity at position 2. MCNP is in orange; SAND II is in magenta. 81

Figure 4.13 Estimated system ^{99}Mo production as a function of time without reflectors in blue, with reflectors in magenta. 85

LIST OF TABLES

Page

Table 3.1 Simulated and empirical neutron dose rates....35

Table 3.2 Activation wire materials, reactions, γ energies, and half-lives....42

Table 3.3 Activation Wire Minimal Detectable Activities....56

Table 4.1 Recorded spectral features from activation wire spectra....67

Table 4.2 Mean saturation activities and neutron flux by product nuclide....70

Table 4.3 MCNP reaction rates and saturation activities....72

Table 4.4 Integral MCNP and SANDII Fluxes....79

Table 4.5 MCNP estimates and derived system parameters....83

1. INTRODUCTION

Over 10,000 hospitals globally use radioisotopes in medicine; the most popular radioisotope, ^{99m}Tc ($T_{1/2}$=6 hours) a daughter of ^{99}Mo ($T_{1/2}$=66 hours), is used in over 40 million procedures annually and accounts for almost 80% of all nuclear medicine procedures worldwide. [1] The annual world market for ^{99}Mo is over $550 million per year and the use of radiopharmaceuticals in diagnosis is increasing at rate of over 10% per year. [1] Despite being the largest single user of ^{99m}Tc, the United States currently imports the entirety of its supply. [2] The current supply chain relies heavily on aging nuclear reactors. In 2018, roughly 85% of the world supply of ^{99}Mo was produced in three reactors: High Flux Reactor in the Netherlands (40%), BR-2 in Belgium, and Opal in Australia (24%). [1]

A series of incidents in 2008 and the shutdown of two reactors for maintenance in 2009-2010 resulted in severe ^{99}Mo shortages revealing the fragility of the supply chain. [1-3] The United States is particularly susceptible as its entire supply relies on international air transportation. In the past, this has been disrupted by logistical problems, such as customs delays or pilots denying additional freight weight, inclement weather or other natural phenomena, and terrorist attacks. [3] In 2013, Congress passed the American Medical Isotopes Production Act, to ensure a reliable U.S. supply of ^{99}Mo and eliminate the export of highly enriched uranium (HEU, ^{235}U≥20%) for the production of medical isotopes. [3]

Several United States private-sector companies are developing production capabilities for ^{99}Mo through a variety of different methods. The National Nuclear Security Administration (NNSA) currently has cooperative agreements that provide up to $25 million in matching funds with three partners: NorthStar, SHINE Medical Technologies, and General Atomics.[4] NorthStar is pursuing two methods: (1) neutron capture of ^{98}Mo in a research reactor, and (2) photon-induced transmutation of ^{100}Mo using photons produced from electron accelerators. SHINE Medical Technologies is developing a deuterium-tritium accelerator to induce fission in a sub-critical low enriched uranium (LEU, $^{235}U \leq 20\%$) uranyl sulfate solution to produce fission-based ^{99}Mo. General Atomics intends to produce fission-based ^{99}Mo from a LEU target using selective gas extraction technology. Others such as Coqui Radiopharmaceuticals and Flibe Energy intend to build new reactors to produce ^{99}Mo. [3] Global Medical Isotopes Systems (GMIS) is pursuing a sub-critical accelerator driven system to produce fission-based ^{99}Mo using natural (NU, $^{235}U=0.7\%$) or depleted uranium (DU, $^{235}U \leq .0.7\%$.)

GMIS constructed a prototype facility in Henderson, NV utilizing an Adelphi DD109 neutron generator and DU. This prototype was to be used to demonstrate the production of ^{99}Mo from uranium fission and other radioisotopes of interest including ^{3}H from irradiation of lithium metal. This research was focused on quantifying the behavior of the GMIS system.

The primary objective of this research was to provide a validated model of GMIS's sub-critical assembly and provide estimates of (1) dose calculations, (2) radioisotope production rates, and (3) neutron flux and energy spectrum. This was

accomplished using MCNP6, a general purpose Monte Carlo N-Particle code used for neutron, photon, and electron transport.[5] A MCNP6.1 model of the GMIS prototype system in varying configurations was constructed. The model was validated by measuring neutron fluxes using activation wires at various locations within the prototype system. Neutron flux spectra were estimated using neutron unfolding codes.

2. BACKGROUND

2.1. Prototype System Description

The GMIS prototype consisted of a subcritical assembly arranged around a neutron generator to produce and extract ^{99}Mo through neutron induced fission in uranium and a proprietary in-situ chemical process. Based on a request from the NNSA through the Nevada National Security Site (NNSS), GMIS was additionally interested in producing tritium from irradiation of lithium metal or lithium carbonate in the system. A physical description of the sub-critical assembly and generator are given in section 2.1.1. Details of the generator's operation are discussed in section 2.1.2. Prior to this research, GMIS had performed little research to quantify the system. A summary of GMIS reported measurements and parameter estimates is included in section 2.1.3

2.1.1. Physical Description

The GMIS prototype consisted of depleted uranium arranged around an Adelphi DD109 neutron generator. The system was oriented along cardinal directions. A SolidWorks model of the system may be seen in Figure 2.1 with the east and north walls removed. There are some additional features not shown, such as cables, pumps, and piping, that present additional minor opportunities for neutron scattering or absorption. The entire system was contained within laminated shielding, with cavity dimensions of 60.96 cm X 60.96 cm X 121.92 cm and exterior dimensions of 96.52 cm X 96.52 cm X 147.32 cm. The side and top shields were composed of seven layers: three inner layers of borated high density polyethylene (BHPDE), one middle layer of stainless steel (SS316),

and three outer layers of virgin high density polyethylene (HDPE). The base shielding consists of three layers of BHPDE resting on a SS316 pallet. An overhead crane allowed movement of the shielding and other system components.

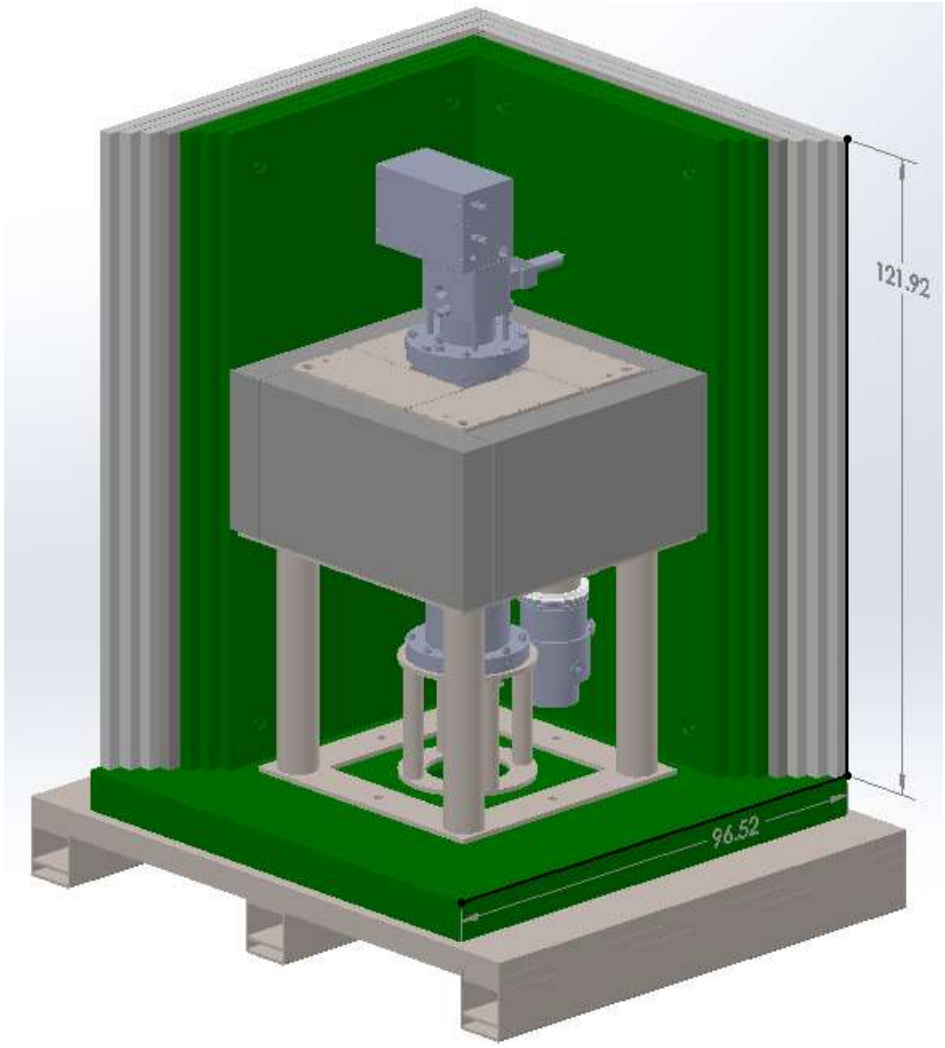

Figure 2.1 SolidWorks Model of the GMIS Prototype**.** The east (left), north (right), and top shielding layers are removed. The neutron generator is mounted in the center with four SS316 boxes containing the DU sheets arranged around it. The boxes are surrounded by four DU reflectors. Piping and connections are not shown. Displayed dimensions are in cm. The inner cavity dimensions are 60.96 cm X 60.96 cm X 121.92 cm. The exterior shielding dimensions are 96.52 cm X 96.52 cm X 147.32 cm.

The neutron generator head consists of an acceleration chamber, ion source, magnetron box, and microwave tuner. A detailed rendering of a DD108 generator with the attached magnetron may be seen in Figure 2.2. The generator head is located in the center of the system resting on a stainless steel (SS316) ring stand; it is vertically oriented to save space. The stand is 22.86 cm tall with a 15.24 cm interior diameter and 25.40 cm exterior diameter. The acceleration chamber is cylindrical in shape 57.67 cm long with an exterior diameter of 15.24 cm. The ion source, microwave tuner, and magnetron box extend above the acceleration chamber; there is 6.68 cm clearance between the top of magnetron box and the interior shielding ceiling. The generator sits in a circular cut out of a SS316 table surrounded by four stainless boxes (30.23 cm X 15.24 cm X 31.12 cm) which contain the DU metal target material. HV voltage cabling, coolant plumbing, and vacuum plumbing connect to the generator through a gap in the base. A photograph of the system absent all uranium content is included in Figure 2.3. Control wiring connects

through cutouts in the top southwest corner of the shielding to the magnetron and waveguide. The deuterium gas feed enters the ion source from the east wall.

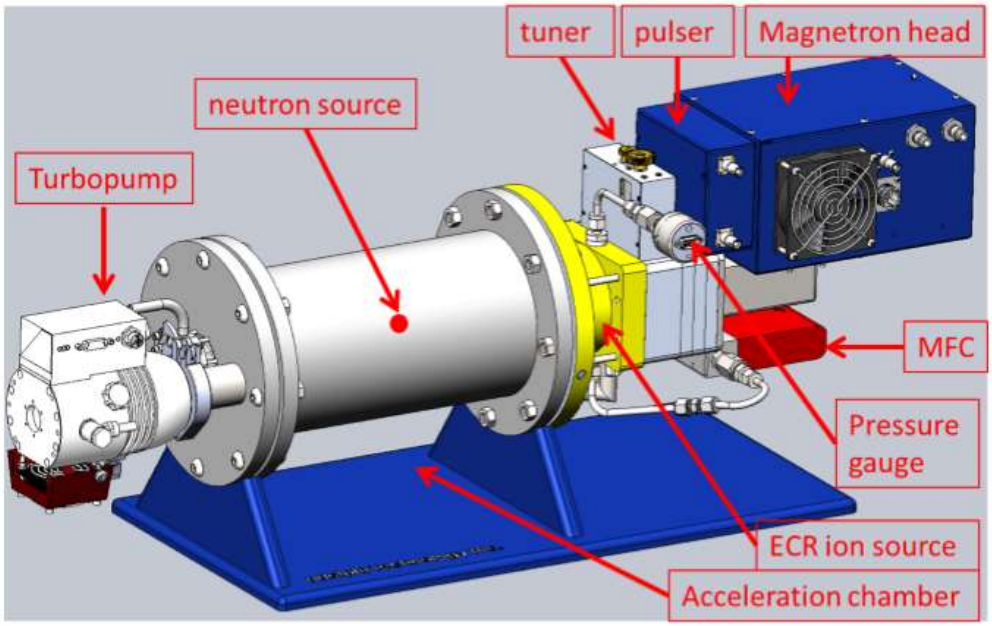

Figure 2.2 Model of a DD-108 neutron generator with labeled major components**.** The DD-108 is similar to the DD-109 used in this research. [6]

The system does not utilize traditional fuel pin design; instead, it relies on thin sheets (29.595 cm X 0.0762 cm X 27.940 cm) of DU metal in order to maximize surface area for the chemical extraction process used to extract ^{99}Mo. The boxes are surrounded by DU metal reflectors (53.09 cm X 7.37 cm X 30.48 cm). The DU boxes and reflectors rest on a SS316 table so that the midline of the DU sheets is level with the apex of the neutron generator target wedge. The generator's ion source and wave guide extend above the top level of the DU boxes. A photograph of the target boxes and uranium reflectors is included in Figure 2.4.

Figure 2.3 Photograph of the GMIS neutron generator and support features in shielding enclosure**.** The dashed line marks the apex of the generator's target and the mid-line of the absent uranium system elements. The east and top shielding layers are removed. The inner cavity dimensions are 60.96 cm X 60.96 cm X 121.92 cm. The exterior shielding dimensions (including removed lid) are 96.52 cm X 96.52 cm X 147.32 cm.

Figure 2.4 Photograph of the uranium target boxes and reflectors surrounding the neutron generator within the shielding enclosure. The east wall is removed. Approximate total uranium mass is 395 kg for the target sheets and 904 kg for the reflectors.

The DU target boxes did not have a consistent number of DU sheets. The initial sheets were sandblasted after being rolled which resulted in warping. Only 50 sheets could be fit in the first box. The next round of sheets was rolled with ribbing to minimize contact between the sheets to maximize solution flow during the chemical extraction stage. Only 79 sheets could be fit into the containing box. Further refinement in production methodology allowed 101 sheets to be fitted in each of the remaining two boxes. Each box was designated by number and location as shown in Figure 2.5. The sheets were inserted so that a 2.54 cm gap was located at the top of the box. Plumbing connections allow for a chemical extractant including nitric acid to wash over the plates; the extractant is then pumped out of the irradiation cavity for processing. The target plates are expected to last several hundred production and extraction cycles. Small cutouts in the base of the shielding, the center of the north wall, and the top and bottom northwest corners offered potential radiation streaming paths through the shielding.

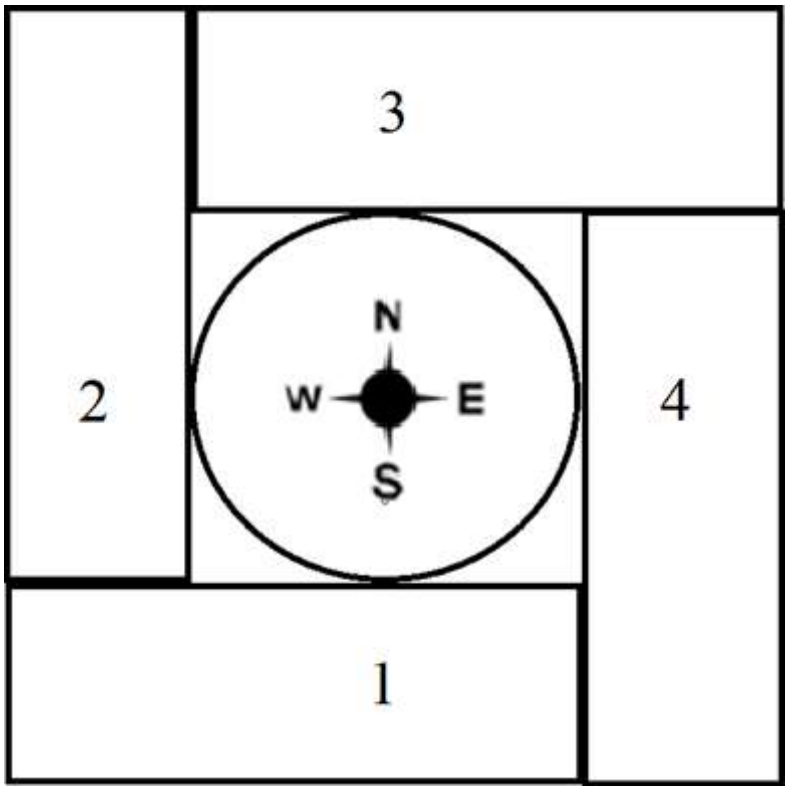

Figure 2.5 Positions of uranium target boxes**.**
Numbers were assigned clockwise beginning from the south. Each box contained a variable number of uranium target sheets: Box 1 had 50, Box 2 had 101, Box 3 had 101, and Box 4 had 79 sheets.

GMIS was also interested in using the system for tritium production from either natural lithium metal or enriched ^{6}Li carbonate. To test the efficiency of this system for tritium production, target box 1 was temporarily replaced with a HDPE block 12.54 cm X 30.48 cm X 30.48 cm to form a moderated zone. Four 12.7 cm deep holes with 5.70 cm diameters and 7.62 cm center to center distances were drilled into the HDPE block to hold lithium samples in sealed borosilicate glass jars. The first hole was on the central axis of the block 3.81 cm from the edge. Target box 4 was replaced with target box 3, leaving an air gap in position 3, which was intended to form a fast neutron zone.

2.1.2. Neutron Generators

There are multiple ways of producing neutrons. Some of the most prolific are fission, fusion, and spallation. Neutron generators offer one potential set of sources, relying on fusion reactions to produce neutrons. Two principal reactions are of interest, deuterium-deuterium (D-D) and deuterium-tritium (D-T) fusion, shown below. [7]

$$ {}^{2}_{1}\mathrm{D} + {}^{2}_{1}\mathrm{D} \rightarrow \begin{matrix} {}^{3}_{2}\mathrm{He} + \mathrm{n} + 3.27\ \mathrm{MeV} \quad (50\%) \\ {}^{3}_{1}\mathrm{T} + {}^{1}_{1}\mathrm{H} + 4.03\ \mathrm{MeV} \quad (50\%) \end{matrix} $$

$$ {}^{2}_{1}\mathrm{D} + {}^{3}_{1}\mathrm{T} \rightarrow {}^{4}_{2}\mathrm{He} + \mathrm{n} + 17.59\ \mathrm{MeV} $$

In both reactions, the neutrons are produced almost monoenergetically, at 2.45 MeV and 14.1 MeV for D-D and D-T respectively if the kinetic energy of the ions is comparatively small. Most commercially available neutron generators operate on similar principles: fusion reactions are induced by the collision of accelerated deuterium/and or tritium ions. Typically, a small accelerator (~100 keV) bombards a deuterium or tritium implanted target with an ion beam resulting in fusion. [7] Traditional designs used a TiD_2 or TiT_2 target resulting in a limited operational lifetime due to outgassing of the hydrogen isotope from the target due to the high power density of ion beam. [9] Recent developments have enabled much longer lifetime designs due to self-loading targets. Due to the large differences in the cross-section for fusion reactions, D-T neutron generators possess an inherent advantage in terms of raw neutron output emitting a factor of ~10^2 times n s^{-1} more than for identically sized D-D generators, see Figure 2.6. D-D and D-T generators with respective yields of up to 10^{12} n s^{-1} and 10^{14} n s^{-1} are commercially available.[7,8]

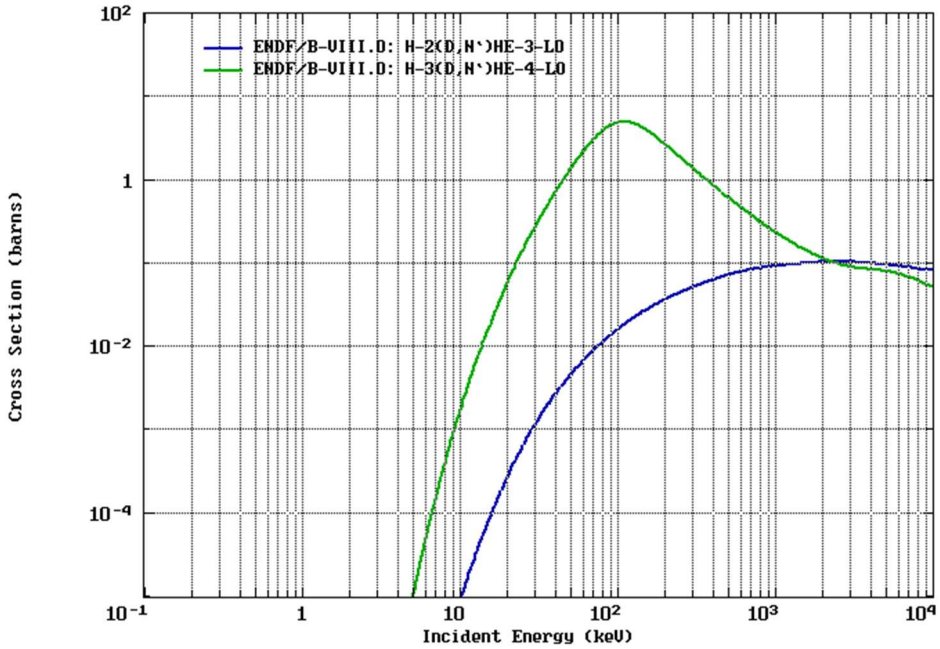

Figure 2.6 : D-D and D-T fusion reaction cross-sections [b] versus energy [keV] At a typical neutron generator accelerator energy of 120 keV, the D-T cross-section is 10^2 times higher than D-D. [9]

The GMIS prototype uses an Adelphi Technology, Inc. DD109 generator. The generator consists of an acceleration chamber, electron-cyclotron resonance plasma ion source, magnetron, and microwave tuner. Injected deuterium gas is ionized by the magnetron forming a plasma source; ions are accelerated from this plasma towards a negatively biased titanium coated copper target (~120 kV). The titanium layer is thick enough to completely stop the impinging beam. Initial D^+ ions strike the target implanting and forming titanium hydrate; subsequent D^+ ions strike the implanted ones with sufficient energy to cause the fusion reaction. A significant amount of heat is deposited in the target during operation, this heat can result in outgassing of the implanted deuterium ions lowering the neutron yield. This heat is removed by flowing

cooling fluid (Flourinert® FC-3283) through microchannels in the target. The nominal yield of the DD109 generator is $3x10^9$ n s^{-1} at max power.

2.1.3. GMIS Reported Parameters

Prior to this research, GMIS performed very little research in attempt to quantify the prototype system. No baseline operational curve has been established for the generator to relate operational parameters to neutron yield. Reported in-house dose measurements using a Bonner sphere before complete shielding installation correlated a beam power measurement of 1800 W to a generator production of $3x10^9$ n s^{-1}. However, GMIS personnel were initially mistaken about the operating principles of the generator, reporting that neutrons were emitted from a non-existent plasma created in the target wedge. No in-system detectors were available to monitor operational neutron flux. Operating procedure required dose measurements to be taken at several locations, typically exterior walls and entryways over 3 m from the generator, to ensure the dose rates to public and operators were below threshold limits. These readings were typically instrument minimum readings or otherwise undistinguishable from background, rendering them useless for validation purposes.

GMIS did provide a handful of self-reported measurement and parameter values. A 2015 analysis performed by Pacific Northwest National Lab confirmed the presence of ^{99}Mo/^{99}Tc in the GMIS extractant solution. In August 2016, GMIS self-reported a total system production of 7400 MBq of ^{99}Mo after 4 hours of irradiation based on a measured activity of 27 kBq of ^{99}Mo in a 1 mL recovered sample.[10] On March 17,

2017 GMIS reported tritium production rates of 1.48-1.96 MBq g^{-1} per hour of irradiation from lithium metal to the Government Accountability Office (GAO). The GAO identified GMIS technology as an alternative method for tritium production pending independent verification.[11] GMIS' chief technical officer Dr. Francis Tsang claimed that these results were due to the efficiency of the fast neutrons emitted by the generator for driving fission reactions in the ^{238}U. [12] As a result, Dr. Tsang estimated the system had an unspecified "very high k_{eff} (>0.95)" to explain high production rates. [12]In May 2017, Dr. Tsang specified a $k_{eff,}$ of 0.975 with a multiplication factor of 40. [13]

2.2. Sub-Critical Multiplication

A nuclear reactor is a system which initiates, maintains, and controls the nuclear fission chain reaction. Neutrons released from the fissioning nuclei may induce further fissions in fissile or fissionable nuclei which in turn release further neutrons, which may induce further fissions, and so on. [14] In a critical system, the production and loss of neutrons are exactly balanced. In phase space (energy *E,* space $\boldsymbol{r}$, angle Ω), this balance is described with the Boltzmann equation:

$$\begin{aligned} &-\Omega\nabla\phi_0(r,E) - \Sigma_0(r,E)\phi_0(r,E) \\ &+\iint \Sigma_0(r,E')f_0(\boldsymbol{r};\Omega',E'\rightarrow\Omega,E)\ \times\phi_0(\boldsymbol{r},\Omega',E')d\Omega'dE' \\ &+\frac{\chi(E)}{4\pi}\times\iint \nu\Sigma_{0,f}(E')\phi_0(\boldsymbol{r},\Omega',E')d\Omega'dE' = 0 \end{aligned} \qquad \text{(Eq. 1)}$$

where ϕ_0 is the neutron flux, Σ_0 is the total macroscopic cross-section, $\Sigma_{0,f}$ is the fission macroscopic cross-section, $\chi(E)$ is the energy-dependent probability density function for

produced neutrons, and f_0 is the probability of a neutron scattering from Ω', E' to Ω, E. If a neutron energy group is assumed, this may be rewritten in matrix form as Eq. 2:

$$L_0\boldsymbol{\phi}_0 + P_0\boldsymbol{\phi}_0 = 0 \qquad \text{(Eq. 2)}$$

where ϕ_0 is the multigroup neutron flux vector, L_0 is the destruction operator accounting for leakage, absorption, and scattering, while P_0 is the production operator. For the critical system in fundamental mode, this may be written using the effective multiplication factor, k_{eff}, as Eq. 3:

$$L_0\boldsymbol{\phi}_0 = \frac{1}{k_{eff}} P_0\boldsymbol{\phi}_0 \qquad \text{(Eq. 3)}$$

Taking the inner product $\langle .,. \rangle$, which indicates integrating over space and energy, k_{eff} may be rewritten as Eq 4.:

$$k_{eff} = \frac{\langle P_0\boldsymbol{\phi}_0 \rangle}{\langle L_0\boldsymbol{\phi}_0 \rangle} \qquad \text{(Eq. 4)}$$

Conceptually, this factor may be understood to be the number of fission neutrons produced per neutron lost.

If the system is made subcritical with an external neutron source $S(E, \boldsymbol{r}, \Omega)$ present, the steady state balance equation becomes Eq. 5:

$$L_S\boldsymbol{\phi}_S + P_S\boldsymbol{\phi}_S + \boldsymbol{S} = 0 \qquad \text{(Eq. 5)}$$

where $\boldsymbol{\phi}_S$ is the multigroup neutron flux in the subcritical system with the source present. Combining the concept of the multiplication factor expressed in Eq. 4 with Eq. 5, a subcritical multiplication factor k_s may be written as Eq. 6:

$$k_s = \frac{\langle P_s\boldsymbol{\phi}_s \rangle}{\langle L_s\boldsymbol{\phi}_s \rangle} = \frac{\langle P_s\boldsymbol{\phi}_s \rangle}{\langle P_s\boldsymbol{\phi}_s \rangle + \langle \boldsymbol{S} \rangle} \qquad \text{(Eq. 6)}$$

This is conceptually equivalent to the k_{eff} of the critical system in Eq. 4; it is number of fissions neutrons produced per lost neutron. It is directly related to the neutron multiplication *M* in the subcritical assembly according to Eq. 7:

$$M = \frac{1}{1 - k_s} \qquad (Eq. 7)$$

It follows that the total rate *N* at which neutrons are being born in the system from both the external source and fission is given by Eq. 8:

$$\mathrm{N=S \cdot M=} \frac{\mathrm{S}}{(1 - k_{\mathrm{s}})} \qquad (Eq. 8)$$

Thus the production rate of the next generation of neutrons in the system is given by $N \cdot k_{\mathrm{s}}$ with the resulting fission rate given by $N \cdot k_{\mathrm{s}}/v$ where v is the average number of neutrons released per fission. If the primary source of fissions is assumed to be ^{235}U, then the average subcritical power of the reactor, P, may be approximated by Eq. 9 where ε_f is the energy released per fission. [15]

$$\mathrm{P=} \frac{S\, k_s}{v(1 - k_s)} \varepsilon_f \qquad (\mathrm{Eq.}\ 9)$$

If the subcritical system is close to the critical state, then $\boldsymbol{\phi}_S \approx \boldsymbol{\phi}_0$ and it may be expected that $k_s \approx k_{eff}$. However, if the system is more deeply subcritical, the steady state flux $\boldsymbol{\phi}_S$ is significantly different from the critical system flux $\boldsymbol{\phi}_0$. The relationship between k_s and k_{eff} must be further derived.

If the adjoint flux and operators from Eq. 3, are multiplied from the left by $\boldsymbol{\phi}_S$, Eq. 10 is obtained:

$$\langle \boldsymbol{\phi}_S , L^{\dagger}\boldsymbol{\phi}_0^{\dagger} \rangle = \frac{1}{k_{eff}} \langle \boldsymbol{\phi}_S , P^{\dagger}\boldsymbol{\phi}_0^{\dagger} \rangle \qquad \text{(Eq. 10)}$$

Which through the properties of adjoint operators, may be rearranged as Eq. 11:

$$\frac{\langle \boldsymbol{\phi}_0^{\dagger} , L\, \boldsymbol{\phi}_S \rangle}{\langle \boldsymbol{\phi}_0^{\dagger} , P\, \boldsymbol{\phi}_S \rangle} = \frac{1}{k_{eff}} \qquad \text{(Eq. 11)}$$

Similarly, by multiplying Eq. 5 from the left by the adjoint flux $\boldsymbol{\phi}_0^{\dagger}$ yields Eq. 12:

$$\langle \boldsymbol{\phi}_0^{\dagger} , L\, \boldsymbol{\phi}_S \rangle = \langle \boldsymbol{\phi}_0^{\dagger} , P\, \boldsymbol{\phi}_S \rangle + \langle \boldsymbol{\phi}_0^{\dagger}, \boldsymbol{S} \rangle \qquad \text{(Eq. 12)}$$

Dividing Eq. 12 by $\langle \boldsymbol{\phi}_0^{\dagger} , P\, \boldsymbol{\phi}_S \rangle$ gives Eq. 13:

$$\frac{\langle \boldsymbol{\phi}_0^{\dagger} , L\, \boldsymbol{\phi}_S \rangle}{\langle \boldsymbol{\phi}_0^{\dagger} , P\, \boldsymbol{\phi}_S \rangle} = 1 + \frac{\langle \boldsymbol{\phi}_0^{\dagger}, \boldsymbol{S} \rangle}{\langle \boldsymbol{\phi}_0^{\dagger} , P\, \boldsymbol{\phi}_S \rangle} \qquad \text{(Eq. 13)}$$

At this point, it is useful to introduce the external source efficiency φ^* defined in Eq. 14:

$$\varphi^* \equiv \frac{\langle \boldsymbol{\phi}_0^{\dagger} , \mathbf{S} \rangle}{\langle \boldsymbol{S} \rangle} \Big/ \frac{\langle \boldsymbol{\phi}_0^{\dagger} , P\, \boldsymbol{\phi}_S \rangle}{\langle P\, \boldsymbol{\phi}_S \rangle} \qquad \text{(Eq. 14)}$$

The external source efficiency is the ratio of average external source importance to the average fission importance. This represents how 'useful' a source neutron is for causing fission. When $\varphi^* > 1$, source neutrons are better at causing further fissions than neutrons coming from fission; if $\varphi^* < 1$, source neutrons are less efficient than fission neutrons in causing further fission. Combining Eq. 11, Eq 13, and Eq. 14, the relationship between k_{eff} and k_s is given by Eq. 15:

$$\left(1 - \frac{1}{k_{eff}}\right) = \varphi^* \left(1 - \frac{1}{k_s}\right) \qquad \text{(Eq. 15)}$$

Using this relationship, the system power P may be rewritten in terms of k_{eff} and φ^* as Eq. 16:

$$P=\frac{S\,\varphi^*\,k_{eff}}{v\left(1-k_{eff}\right)}\varepsilon_f \qquad \text{(Eq. 16)}$$

The calculation of k_{eff} or k_s may be accomplished using Monte Carlo methods executed by computer codes.

2.3. Monte Carlo Methods

Monte Carlo methods are frequently used in nuclear applications such as radiation shielding, dosimetry, nuclear criticality, radiation transport, and neutron physics analysis. [5,16,17] Monte Carlo methods obtain answers by inferring the average behavior of particles in the system by sampling a large number of individually simulated particle histories. The disadvantage of this approach is that due to its statistical nature, it does not provide an exact solution to the problem. All results are estimates with associated statistical precision (uncertainties); long calculations can be required if very small uncertainties are required. Due to the large number of trials required for an adequate solution, the simulations are usually performed on a computer using a dedicated code. The code used for this research was Monte Carlo N-Particle transport code version 6.1, or MCNP6.1. [5]

2.3.1. MCNP

MCNP6.1 can be used to model radiation transport of 37 different particle types including neutrons, photons, electrons, or coupled problems through a universe composed of user-defined cells. In particle transport, particles are followed from their

source throughout their life to their death. Each individual event in this process is simulated sequentially, probability distributions are randomly sampled using transport data at every step to determine the outcome. MCNP randomly samples between 0 and 1 to determine what, if any, interaction occurs based on physics (rules) and transport data (probabilities).[5] Any additional particles created during transport are banked for later analysis. Figure 2.7 illustrates a sample particle history for a neutron incident on a slab of fissionable material in analog Monte Carlo.

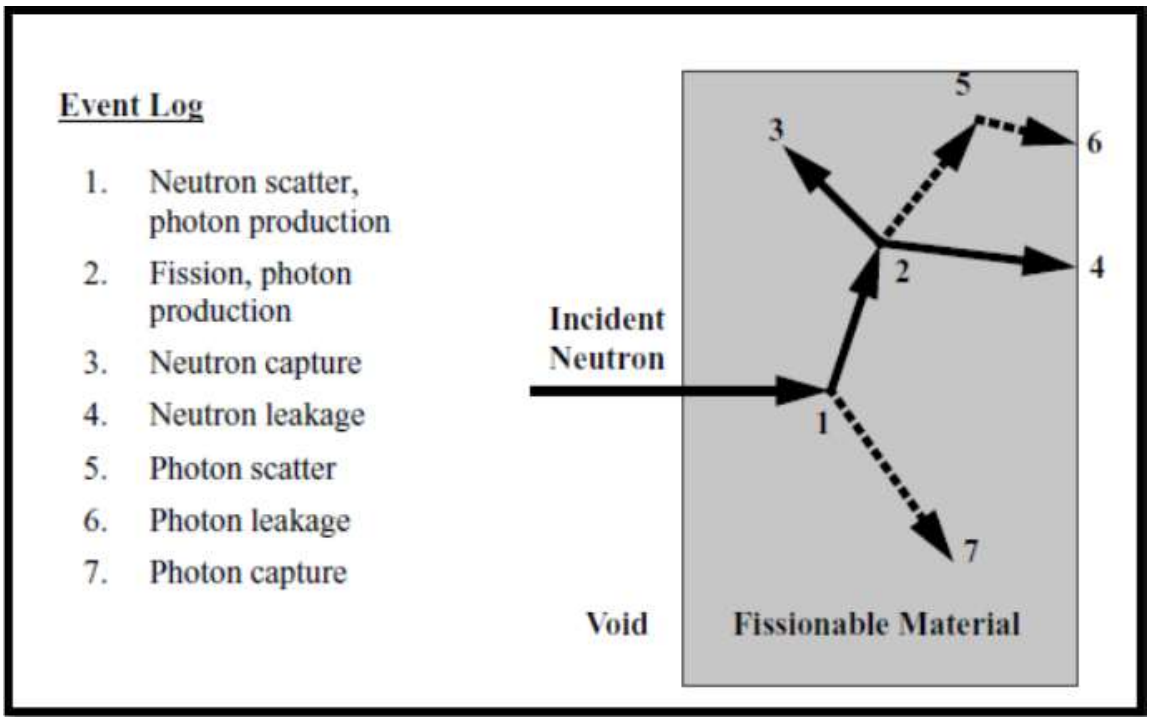

Figure 2.7 Particle history for neutron incident on fissionable slab **[18]**.

From Figure 2.7, an incident neutron, emitted from a source or previous event, undergoes an interaction at event 1which is randomly determined to be a scattering collision. The neutron scatters in a direction that is randomly selected from the physical

scattering distribution; the location of the next event is randomly determined based on the total cross-section of the material. A photon is also created and banked for later transport; note that particles are followed in a 'last in, first out' order. At event 2, the neutron causes fission resulting in its termination and the birth of two new neutrons and a photon. One neutron is followed immediately, the other neutron and photon are banked for later analysis. In event 3, the first neutron is captured and terminated. The banked neutron is selected and leaks out of the slab at event 4. The photon produced in event 2 scatters in event 5 and leaks out in event 6. The photon produced in event 1 is now retrieved and followed to its death in a capture at event 7. The record of all seven events is one particle history. As more histories are collected, the associated particle distributions are more completely described. Once the particle distributions are sufficiently well known, quantities of interest, such as particle fluxes, and the associated uncertainties of the results are tallied.

For any problem, MCNP requires the user to input certain standard information such as problem geometry, material specifications, source location/distributions, desired tallies, and any variance reduction techniques to improve statistics or efficiencies. The initial development of the MCNP input is discussed in section 3.1. A brief discussion of the tallies and variance reduction techniques useful to this research is presented in the following subsections.

2.3.2. MCNP Tallies

MCNP has seven standard tallies that can be applied to a problem. [5] The relevant tallies for this research were the flux averaged over a cell (F4) and the flux at a

point (F5). The F4 tally calculates the volumetric flux by summing the track length of all particles crossing a cell of volume V. If $\Phi(\boldsymbol{r}, E, \boldsymbol{\Omega}, \mathrm{t})$ is the energy and angular distribution of the flux as a function of position and the time dependence is suppressed, the normal case in MCNP calculations, the F4 tally is described by Eq. 17.

$$F4 = \frac{1}{V}\int_V dV \int_E dE \int_{4\pi} d\boldsymbol{\Omega}\, \Phi(\boldsymbol{r}, E, \boldsymbol{\Omega}) \qquad \text{(Eq. 17)}$$

The F5 tally calculates the flux at a specific point r_p using a deterministic estimate discussed in section 2.3.3.4. In both cases, the output of the tally is units of particles cm^{-2} (source particle)$^{-1}$. A steady-state flux solution can be obtained by having a source with units of particles per unit time.

Tallies maybe modified by the use of an FM card. In general, any quantity of the form $\mathrm{FM} = C \int \Phi(E) f(E) dE$ where $\Phi(E)$ is the energy-dependent flux, C is a constant multiplier, and $f(E)$ is any product or summation of quantities cross-section libraries or a user-supplied response function, can be tallied. [5] For example, reaction rates in reactions cm^{-3} may be obtained by setting *C* as the number density of a material and *f(E)* as the reaction cross section.

2.3.3. Variance Reduction Techniques

For many problems, such as deep penetration and shielding calculations, variance reduction is required not only to speed up the calculation but to arrive at any meaningful result. [5] The most basic method is to simply not model parts of the problem that do not significantly contribute to the solution. This includes unimportant aspects of the geometry or particles that fall below relevant energy thresholds. More complicated

methods involve population control to control the number of samples taken, modifying sampling methods to increase the number of tallies per particle, or using quasi-deterministic methods to circumvent the random walk process.

2.3.3.1. Geometry Splitting and Russian Roulette

Geometry splitting with Russian roulette is a population control technique and one of the most commonly used methods.**[5]** Every particle in MCNP has a weight, a measure of its statistical importance. The user may designate each cell with an importance level. Particles moving from regions of higher importance to lower importance undergo Russian roulette. Some particles are killed, but survivors have their weight increased. When particles move from a lower importance cell to a higher importance cell, it is split into two or more particles with less weight. As result, more time is spent sampling in important regions in the geometry. This technique reduces the variance but increases the run time per history.**[16]** It is particularly useful in ensuring sufficient particles track through the shielding layers for exterior tallies to have good statistics.

2.3.3.2. Implicit Capture

Implicit capture methods adjust the sampling of a problem. When a particle collides with a nuclide, there is chance it is absorbed. In analog Monte Carlo, the particle is killed with this outcome; with implicit capture, the particle is never killed by absorption. **[5]** Instead the weight is reduced by the absorption probability. If the particle's weight drops below a specified cutoff, Russian roulette results in either the particle's death or an increase in weight to a specified level. This allows important

particles to survive and continue contributing to tallies until deemed no longer useful. It is not appropriate for low-energy particles where the microscopic absorption is nearly equal to the total cross-section. Implicit capture will reduce variance but increase the time per history, while analog capture produces the reverse. Implicit capture is useful for dealing with neutrons in absorbing materials.

2.3.3.3. Source Biasing

The angular and energy distributions of a source can be biased in MCNP. This adjusts the sampling of the problem, allowing the code to focus on sampling the regions of interest with appropriate weight. For DD/DT neutron generators, the source energy is discrete so only directional biasing is relevant. Biasing the angular distribution is useful for directing source particles towards detector tally regions or away from leakage prone directions. This reduces the number of particles required to achieve sufficient statistics.

2.3.3.4. Point Detector Tally

Point detector tallies provide a fast way to measure particle fluxes at specific points in space. The probability of a given particle transports precisely to that point is vanishingly small.**[5]** A point detector tally is a 'next-event estimator'. With every collision in the system, a low weight pseudo-particle is deterministically transported to the point. The result is a tally of the flux as if the 'next event' were a direct trajectory to the point without any other collisions. If the problem is rotationally symmetrical, a ring detector may be used instead. These tallies are useful for obtain quick flux estimates with fewer histories.

2.3.4. MCNP outputs

MCNP is capable of solving problems through either a fixed source calculation or through a criticality estimate. If a problem is run in a fixed source mode, a user-defined source is run for a user-selected number of histories. If the problem is run in criticality mode (kcode), the code flow is iterative instead. The user specifies a number histories per cycle, an initial k_{eff} guess, a number of cycles to skip before k_{eff} values are accumulated, and the total number of cycles in the problem. An initial spatial distribution of neutrons will be transported through the problem, any fission events will be treated as capture with the location stored for the next cycle. These fission sites will be the starting sites for neutrons in the next cycle. The energy of each neutron will be always be randomly sampled from a Watt fission spectrum. After an initial number of cycles are skipped, k_{eff} values are averaged and tallies are accumulated until the total number of cycles is reached.

Criticality calculations can only estimate k_{eff} for a driven system not k_s since it does not account for the energy-dependent fission efficiency of the driving neutrons. Since the fixed source calculations account for the efficiency of the source neutrons for causing fission, it is possible to calculate the k_s and φ^* using a combination of fixed source and kcode calculations. Eq. 15 may be rewritten as Eq. 18.

$$\varphi^* = \left(\frac{1-k_{eff}}{k_{eff}}\right) \frac{\langle P_S \boldsymbol{\phi}_S \rangle}{\langle \boldsymbol{S} \rangle} \qquad \text{(Eq. 18)}$$

$\langle P_S \boldsymbol{\phi}_S \rangle$ is the total production of neutrons by fission in the source driven system and can be determined using a fixed source calculation. A criticality mode calculation can be

used to determine k_{eff} for the same system. The results may combined to estimate the φ^*according to Eq. 18.

In either mode once the particle distributions are sufficiently well known, quantities of interest, such as particle fluxes in a given cell, and the associated uncertainties of the results are tallied. In fixed source calculations, the tallies are normalized per starting particles, i.e., source strength; in criticality problems, tallies are normalized per fission neutron generation, i.e., per reactor power. Possible tally quantities include reaction and dose rates, quantities that were used to validate the MCNP model generated in this research through direct measurements and foil activation.

2.4. Foil Activation

2.4.1. Theory

The neutron flux and its energy spectrum within a system are parameters of particular importance in determining isotope production rates. These parameters may be determined via interactions. A sample of material can be exposed to a flux of neutrons over some time period and then removed and counted. The measured radiations may be used to deduce information about both the number and energy of neutrons in the system. [19] The most common approach is to use a thin foil or wire so as not to perturb the neutron flux. In this case, the activation reaction rate R [s^{-1}] occurs in the foil according to Eq. 19.

$$R = \varphi \sum V \qquad \text{(Eq. 19)}$$

Here φ is the average neutron flux over the foil volume [n cm^{-2} s^{-1}]; $\sum$ is the macroscopic activation cross section averaged over the neutron spectrum [cm^{-1}], and V is

the foil volume [cm^3]. As the foil is irradiated, the newly activated species immediately begins to decay at the rate λN where λ is the decay constant and N is the total number of radioactive nuclei present. If the neutron flux is assumed to be constant and there is no 'burnup' or decrease in target nuclei over the measurement, R may also be assumed to be constant. The rate of change in N is given by Eq. 20 with the solution Eq. 21 and resulting foil activity A given by Eq. 22.

$$\frac{dN}{dt} = R - \lambda N \qquad \text{(Eq. 20)}$$

$$N(t) = \frac{R}{\lambda}(1 - e^{-\lambda t}) \qquad \text{(Eq. 21)}$$

$$A(t) = R(1 - e^{-\lambda t}) \qquad \text{(Eq. 22)}$$

The induced activity is time dependent and approaches an asymptote, the saturated activity A_∞, after an infinitely long irradiation yielding Eq. 23.

$$A_\infty = R = \varphi \sum V \qquad \text{(Eq. 23)}$$

If an irradiation is performed over an interval t_0, the foil has acquired an activity A_0 given by Eq. 24.

$$A_0 = A_\infty(1 - e^{-\lambda t_0}) \qquad \text{(Eq. 24)}$$

If the activated foil is transferred to a counting system and counted over an interval from t_1 to t_2, number of counts C is given by Eq. 25.

$$C = \epsilon \int_{t_1}^{t_2} A_0 \, e^{-\lambda(t - t_0)} dt + B$$

$$= \epsilon \frac{A_0}{\lambda} e^{\lambda t_0}\left(e^{-\lambda t_1} - e^{-\lambda t_2}\right) + B \qquad \text{(Eq. 25)}$$

Here ϵ is the total efficiency of the counting system and B is the number of background counts expected over the interval from t_1 to t_2. Eqs. 24 and 25 may be combined to yield the saturated activity:

$$A_\infty = \frac{\lambda(C-B)}{\epsilon(1-e^{-\lambda t_0})e^{\lambda t_0}(e^{-\lambda t_1}-e^{-\lambda t_2})} \qquad \text{(Eq. 26)}$$

This may be used to calculate the magnitude of the neutron flux φ from Eq. 23.

Activation foils are integrating detectors and give no information about time variations in the neutron flux. However, they are generally small, low cost, insensitive to gamma radiation, and require no signal connections. Accordingly, they are useful for measuring the spatial variations of steady-state neutron fluxes inside a reactor. The use of several different materials for activation detectors allows additional information about the neutron energy spectrum to be deduced.

Each material and its associated reactions will possess different cross-sections that are dependent on neutron energy. Cross-sections for (n, γ) reactions are typically largest at thermal energies; materials with a strong preference for these reactions act as slow neutron detectors. Many of these materials also possess strong resonances in their cross-sections at particular neutron energies between 1 and 1000 eV. The contributions of thermal and resonance neutrons may be separated through the cadmium difference method. Cadmium possesses a strong radiative capture cross section below 0.5 eV and a very low cross section above that energy. A small thickness of cadmium, 0.5 mm, is sufficient to preferentially absorb the majority of thermal neutrons but allow fast neutrons without significant attenuation. **[*16*]** If two identical foils are prepared, one

covered with cadmium the other uncovered, the uncovered foil will respond to both thermal and resonance neutrons while the covered foil will only respond to resonance neutrons. The difference between the activations in the two foils will yield the thermal neutron contribution. Other materials have a strong preference for (n, p), (n, α), or (n, 2n) reactions; these reactions typically require a minimum neutron energy enabling them to act as threshold detectors for fast neutrons. Each material will respond to a different range of neutron energies. If a set of various activation foils is irradiated in a given neutron field, differences in cross-sections enable a neutron energy spectrum to be unfolded using a computer code such as SAND-II. **[*15*]**

2.4.2. Unfolding Code

The computer code SAND-II was used to assist this research. The software provides a 'best fit' neutron flux spectrum for a given set of infinitely dilute foil activities. [21] An initial approximate spectrum is iteratively perturbed to yield a solution spectrum that produces calculated activities similar to those measured within a given error limit. This solution is either a flux for steady-state neutron environments or a time-integrated flux (fluence) for a pulsed environments.

The code uses a discrete interval description of the neutron energy range rather than a continuous representation by an analytical function. A total of 620 intervals are used to cover the energy range between 10^{-10} and 18 MeV, 45 per decade up to 1 MeV and 170 between 1 and 18 MeV.[21] The code essentially solves for 621 unknown (solution differential flux values) in a system of *n* linear activity equations, where *n* is the number of foils used. The solution will not be unique since number of equations is

much smaller than the number of unknowns (n<<621). The appropriateness of the solution depends on the initial approximation based on available physical information.

The mathematical procedure may be summarized by the following equations:

$$\Phi_j^{k+1} = \Phi_j^k e^{C_j^k} \quad \text{(Eq. 27)}$$

$$C_j^k = \frac{\sum_{i=1}^{n} W_{ij}^k \ln\left(\frac{A_i}{A_i^k}\right)}{\sum_{i=1}^{n} W_{ij}^k \ln\left(\frac{A_i}{A_i^k}\right)} \quad \text{(Eq. 28)}$$

$$W_{ij}^k = \frac{A_{ij}^k}{A_i^k} \quad \text{(Eq. 29)}$$

$$A_{ij}^k = \Phi_j^k \sigma_{ij}\left(E_{j+1} - E_j\right) \quad \text{(Eq. 30)}$$

$$A_i^k = \sum_{j=1}^{m} A_{ij}^k \quad \text{(Eq. 31)}$$

Where:

Φ_j^k = the kth iterative neutron flux density (assumed constant) over the jth energy interval

C_j^k = the kth iterative neutron flux density correction term for the jth energy interval

A_i^k = the calculated saturation activity for the ith detector, based on the kth iterative neutron spectrum

W_{ij}^k = weighting function for the ith foil response over the jth interval

σ_{ij} = averaged constant reaction cross section for the ith foil over the jth energy interval

m= the total number of energy intervals

n= the number foils used

In brief, activities are calculated for each foil based on the iterative spectrum and evaluated cross section library native to the code. Correction factors are obtained by comparing calculated activities to measured activities. An energy weighting function is obtained for each foil based on the differential cross section multiplied by the differential flux calculated at the kth current iteration. The weighting function is used to generate an average correction factor at each energy based on a comparison of the measured and calculated activities and the relative contribution of the flux at a given energy to activity of the foil. The average correction factors are applied to the current k^{th} iterated flux value at each energy to obtain the k+1 flux spectrum. A solution is achieved when the difference between two successive flux values is smaller than a user specified input percentage at all 621 energy points. The resulting solution flux may be compared to one produced from MCNP.

3. METHODOLOGY

3.1. MCNP Model Development

As discussed previously, MCNP is a powerful tool for modeling radiation transport, and calculating derived quantities. Since modeling the transport of neutrons and calculating isotope production rates from fission or direct irradiation was the goal of this research, several MCNP models were developed to provide dose rates and neutron flux estimates for comparisons with experimental data from foil detectors and dosimeters. Sample MCNP code is included in Appendix A.

3.1.1. Lithium Irradiation

The original configuration of the MCNP model was designed to replicate the lithium irradiations performed by GMIS in late 2016. In these irradiations, target position 1 was filled with a HPDE block containing 4 borosilicate jars with 10 g natural lithium (99.99% purity) samples. The samples were formed into rough coils by wrapping lithium foil (3.5 cm X 0.017 cm X 63 cm) around a mandrel. The samples were prepared in a glove box under argon. Target position 3 was left as an air gap to provide a fast neutron region for later experiments; results from this position were not made available. Positions 2 and 4 were filled with target boxes each containing 101 DU sheets. The lithium samples were irradiated at full generator power for 14 hours. The lithium samples were then digested in Perkin Elmer Ultima Gold Ab liquid scintillation cocktail and counted in a Hidex Trialthler on loan from the Remote Sensing Laboratory at the NNSS to obtain tritium activities.

The model to replicate this experiment was constructed of several hundred cells. The dimensions of the generator, uranium assembly, and shielding described in Section 2.1.1 served as the basis for the model's surfaces and cells. The primary features were the SS316 components of the generator housing and support structure, the SS316 boxes with the DU sheets, the DU reflectors, the polyethylene moderating block, the lithium metal coils in borosilicate glass vials, and the laminated shielding. The model coordinate system was centered at the apex of the wedge inside the neutron generator. The model was limited to the exterior surface of the shielding.

Position 1 was replaced with a HDPE block holding 4 lithium samples in borosilicate jars with polyethylene tops; position 4 was replaced with an air gap. The lithium coils were modeled as series of concentric hollow cylinders with expanding radii with the outermost cylinder missing a wedge to match the total circumference to length of the unwound lithium coil. Each cylinder was 0.017 cm thick and 3.5 cm high; the total circumference of all cylinders was 63 cm. Each of the target boxes was modeled with 101 evenly spaced DU sheets with alternating air gaps. The DU targets were modeled separately as perfectly straight sheets despite the known warping. The DU reflectors were split into four 2.54 cm slices to enable importance biasing for better statistics. Features of minor interest, such as the air gaps surrounding the assembly, or thickness, such as the support tables, were modeled as single cells.

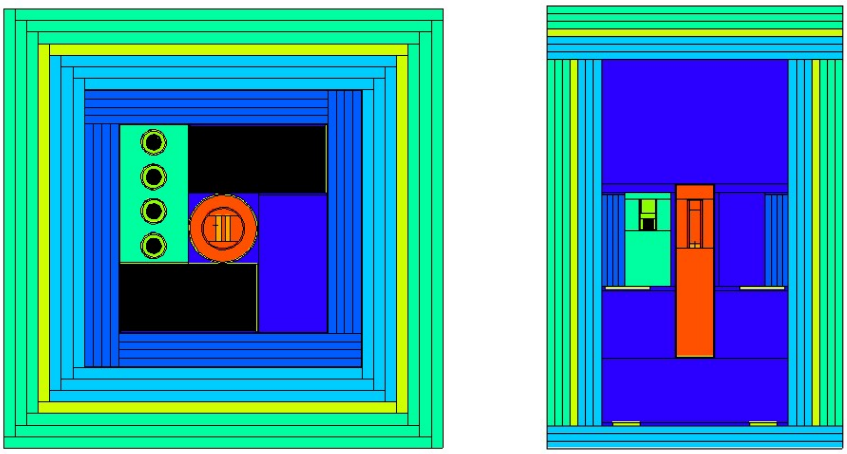

Figure 3.1 Vertical and horizontal cuts of the MCNP model.
Cuts taken at Z=5.0 cm and Y= -4.0 cm to illustrate the lithium coils and major features.

Vertical and horizontal cuts can be seen in Figure 3.1. The vertical cut was taken at 4 cm below the central plane; the horizontal cut was taken at 5 cm above the central plane. These locations were chosen to illustrate the lithium coils in the model. The exterior layers of laminated shielding are visible in both cuts: the HPDE layers are light green, the SS316 is yellow, and the BHPDE is light blue. The uranium reflectors, split into four 2.54 cm slices are dark blue. Air gaps in the system are purple. The SS outlines of the target boxes and support table can be seen in the vertical cut. Due to the large number of cells in the target boxes, the uranium target sheets and air gaps in the target boxes appear as a black box; the same is true of the lithium coils in borosilicate jars due to layering of the lithium cylinders and the surrounding argon atmosphere (light green). The neutron generator can be seen in center of both figures filled with low density deuterium gas (orange). The copper wedge target (tan) is enveloped by a 0.3 cm aluminum shroud (red). Additional information about the structure of the generator was

unknown but should only have a minor effect on the behavior of the model. Material compositions are listed in Appendix B.

The problem was run as a fixed source calculation with a volumetric source for 10 megahistories. Due to misunderstanding about the ion source, GMIS insisted that generator operated by forming a plasma in the gap of the target wedge; neutrons were assumed to be emitted from this plasma. This was implemented in MCNP by defining a box that enveloped the target. Randomly selected points in this box were accepted as source points only if they occurred inside the wedge of target. Neutrons would be emitted isotropically from these points monoenergetically at 2.45 MeV.

Since the goal of this simulation was to estimate the tritium production in the lithium, a series of F4 tallies were used to determine the neutron flux in the lithium coils. The total tritium production in lithium was calculated using an FM card to multiply the obtained neutron flux by the cross-sections for the ^{6}Li(n,t) and ^{7}Li(n,n') reactions. Assuming a source strength of $3x10^{9}$ n s^{-1}, the resulting average tritium production rate was 2.259±0.021 Bq g^{-1} h^{-1} compared to a GMIS reported rate of 1.48-1.96 MBq g^{-1} h^{-1}. The cause of this exceptional disagreement was not immediately apparent. To help determine if the error was in the model or the measurements, a quick validation experiment was performed using exterior dose measurements.

3.1.2. Exterior Dose Measurements

To provide minimal initial validation, neutron dose rates were collected at five points outside the assembly enclosure during operation using a Ludlum Model 2241 neutron dose survey meter. [22] The detector consists of a 2 Atm ^{3}He tube (LND 25185)

in a 22.9 cm diameter cadmium-loaded polyethylene sphere.[23] Dose rates were measured at 5 points outside: center top of the generator shielding, center of the east wall, 98.8±0.5 cm from the center of the east wall, center of the south wall, and 91.5±0.5 cm from center of the south wall. The detector was placed on a rolling cart to maintain a uniform height of 160 cm with the exception of the generator ceiling. The observed dose ranges are listed in Table 3.1 where they are compared to simulated rates from an updated MCNP model.

Table 3.1 Simulated and empirical neutron dose rates

Location	Measured [mR h^{-1}]	Simulated [mR h^{-1}]
East 1	9.5± 0.6	18.44 ± 0.76
East 2	3.4± 0.6	3.27 ± 0.04
South 1	2.4± 0.4	4.78 ± 0.60
South 2	1.3± 0.4	0.96 ± 0.02
Top	23.8± 0.8	24.3± 0.6

The MCNP model required several updates due to physical changes in the system including expansion of the problem area, addition of shielding, correction of the source term, and the reinsertion of the target boxes. The simplest was the expansion of the problem area. The initial model ended at the enclosure walls while dose rates had to be recorded outside the walls. The model was extended an additional 1.2 m in the relevant directions. Similarly, several additional layers of shielding were added to the enclosure: 5.08 cm of BHDPE to both the south and east walls exterior walls with an additional 2.54 cm of HDPE to the south wall. A 2.54 cm layer of BORAL® (borated aluminum) was added to the top layer. These layers were bolted directly onto the preexisting outermost layers. The space directly above the generator was converted to an aluminum

block at 70% of normal density to represent the scattering surfaces present by the magnetron box. Modifications to the source term were required due to a correct understanding of the operation of the generator as outlined in section 2.1.2. The source was changed from a volumetric source contained within the target wedge to a surface source covering the interior area of the target wedge. The internal reconfiguration of the target boxes was necessitated by operator behavior.

After the lithium irradiation, GMIS reconfigured the system for ^{99}Mo test production. The HDPE block was removed and the target boxes were reinserted. Several test runs occurred during this period. In one of them, the stainless steel flex tubing that carried the extractant ruptured due to undetermined causes, likely material fatigue. [12] After this incident, the GMIS CTO erroneously loaded the wrong file for the system plumbing controls: closing several valves and turning off the system pumps. As result, extraction solution was trapped in the target boxes for an extended period of time resulting in a significant increase in pressure from the extraction chemical reaction. The system eventually reached pressure equilibrium when two of the stainless steel target boxes ruptured, sheering off several bolts and releasing the extraction solution. System clean-up required the temporary removal of the target boxes and the DU reflectors. While the sheer mass of the system initially held the target boxes in place, the pressure increase severely warped the sides causing them to bulge out. The resulting warping meant both the target boxes and reflectors could not fit back into the cavity once removed due to the tight spacing. GMIS made the decision to continue doing further

testing with only the target boxes in the system pending completion of a production unit at their Oak Ridge, Tennessee facility.

To account for these changes, the DU reflectors were removed from the MCNP deck and replaced with an air gap. The air and HDPE blocks from the lithium irradiation were replaced with the appropriate target boxes. Despite the warping of the target boxes' exterior and sheets, the MCNP target boxes were not significantly modified as the total mass had not changed. While this method neglected to account for the repositioning of the fissionable material in the boxes, the displacement effects were judged to be minor compared to the removal of the large masses of fissionable material in the reflectors. The problem was run as a fixed source calculation with a surface source for 10^6 histories with an assumed generator source strength of 2.0×10^9 n s^{-1} based on the GMIS operator's estimate. In all cases MCNP tallies passed all 10 statistical tests and errors were below 5%. MCNP estimates are listed in Table 3.1 where they are compared to empirically measured dose rates.

The empirical and simulated dose rates show rough agreement within their estimated error. The empirical dose rates were recorded over a 30 second period at each location with error values estimated from the maximum deviations during that period. Simulated dose rates were calculated using F5 tallies and the ICRP-21 flux-to-dose conversion factors. The estimates for the top and further side measurements all agree within the estimated 1σ error range. The simulation estimates for the two side locations closest to the generator overestimate the empirical dose by a rough factor of 2. The cause of this difference remains unclear. The most likely explanation is an incorrect detector

position for the measurements closest to the wall. The detector position was reported as 'against the wall', the discrepancies could be explained if the position was actually a few inches from the shielding wall. In a subsequent simulation, moving the tally location for East 1 2.54 cm further away from shielding wall resulted in 17% reduction in the dose rate. Alternatively, it is possible that the omission of some potential absorption surfaces in the unmodeled extraction and cooling plumbing of the system resulted in an overestimate of the neutron flux.

However, the goal of these measurements was to provide experimental validation of the initial model to explain the six order of magnitude difference between the GMIS and MCNP estimates for tritium production. Since the MCNP and empirical dose measurements agree well within one order of magnitude, it seems more likely that model was correct and the GMIS estimates were flawed. Further model validation was performed using activation foils described in section 3.2. Subsequent investigation revealed flaws in GMIS' tritium measurement techniques that suggested most of the measured activity was due to chemilumiscnescence caused by placing lithium metal directly in the scintillation cocktail.

3.2. Activation wires

As previously discussed in section 2.4, thin foils or wires may be used as integrating detectors to determine the neutron flux in a system. This may be used to experimentally validate the constructed MCNP model by both comparing simulated and measured wire activation rates. GMIS purchased a Shieldwerx^{TM} SWX-1650 high purity (>99.9%) combination wires kit for activation work that contained 14 materials: Ag, Al,

0.12% Au-Al, Co, Cu, 4.98% Dy-Al, Fe, In, 80% Mn-Cu, Mo, Nb, Ni, Ta, Ti and Cd tubing.

3.2.1. Foil Selection

The GMIS prototype system posed several unique challenges for foil activation measurement campaign. The full energy spectrum of the system needed to be determined while the system was only capable of producing a relatively low neutron flux. As a further constraint, generator run times were limited by staffing requirements and expected generator performance based on prior experience. The longest continual operational period prior to this work was 36 hours; longer irradiation times were assumed not to be feasible. While subsequent gamma spectra measurements could be performed on site, only a single high purity germanium detector (HPGE) was available to count irradiated samples. As a result, several samples needed to be counted at the same time. Foils selected for irradiation and gamma spectra analysis needed to meet the following criteria.

- Wire composition and mass needed to be precisely known. Unknown contaminants would have introduced errors in mass and calculated neutron fluxes. Non-uniform wires would complicate activation analysis. A milligram accurate scale and calibration weight set was available on site.
- Product nuclides needed to emit gamma radiation with sufficient energy separation (~3 keV) based on detector resolution during decay. Several samples needed to be counted at the same time, so competing gammas would complicate analysis.

- The GMIS CTO insisted that there was a strong fast neutron component above the 2.45 MeV DD threshold caused by DT reactions on the residual T products from the initial DD reactions. The reactions of interest needed to cover the full energy range of the system, from thermal to 14.1 MeV, with reactions above 2.45 MeV.
- Cross-section values for the reactions of interest needed to be well known. The cross-section values needed to be large enough to produce significant activity during the irradiation period and subsequent counting time.
- The product nuclides' half-lives ideally needed to be between several minutes and hours. The build-up of activity in the wires occurred at the same rate as its decay. A material irradiated for one half-life would reach 63% of its possible maximum activity; after five half-lives the activity would build up to 97% of the saturation activity. Nuclides with short half-lives would reach equilibrium and saturation activity faster during irradiation. Since on-site counting was available and relatively low neutron fluxes were expected, wires could be quickly transferred for counting without a cooling period minimizing activity loss during transit for short-lived isotopes. Longer-lived nuclides would require prohibitively long irradiation times or produce an insignificant number of decays resulting in poor counting statistics.

Aluminum, cobalt, dysprosium, indium, and manganese wires were selected from the available materials for initial irradiation. Aluminum, cobalt, and indium were chosen because they offered thermal and threshold reactions. Dysprosium was selected for its

large thermal cross-section and its usefulness as an epithermal detector with a cadmium cover. Manganese was chosen as an additional thermal and epithermal detector. Material properties, reactions of interest, and expected product photon energies are summarized in Table 3.2.

Material	Reactions	Energy Region	γ Energy [kev]	Half-life (s)
Al	$^{27}Al(n,\gamma)\,^{28}Al$	Thermal	1778.99 (100%)	134.484
	$^{27}Al(n,\alpha)\,^{24}Na$	Fast: 3.8 MeV	1368.63 (99.99%)	$5.38524x10^{4}$
			2754.01 (99.86%)	
	$^{27}Al(n,p)\,^{27}Mg$	Fast: 4.9 MeV	843.76 (71.80%)	567.5
			1014.52 (28.20%)	
Dy-Al (4.98% Dy)	$^{164}Dy(n,\gamma)\,^{165}Dy$	Thermal Epithermal	94.70 (3.805%)	8402
			361.68 (0.904%)	
			633.42 (0.613%)	
Co	$^{59}Co(n,\gamma)\,^{60m}Co$	Thermal	58.60 (2.07%)	628.02
	$^{59}Co(n,\alpha)\,^{56}Mn$	Fast: 5.2 MeV	846.76 (98.85%)	9284.04
			1810.73 (26.89%)	
			2113.09 (14.23%)	
Indium	$^{113}In(n,\gamma)\,^{114m}In$	Thermal	190.27 (16.08%)	$4.278x10^{6}$
	$^{113}In(n,\gamma)\,^{114}In$	Thermal	1299.83 (0.140%)	71.9
	$^{115}In(n,\gamma)\,^{116m}In$	Thermal	1293.56 (84.88%)	$1.954x10^{5}$
			1097.28 (58.57%)	
			416.90 (27.25%)	
			2112.29 (15.11%)	
			818.68 (12.13%)	
			1507.59 (9.93%)	
	$^{115}In(n,n')\,^{115m}In$	Fast: 0.5 MeV	336.24 (48.20%)	$1.615x10^{4}$
Mn-Cu 81.3% Mn	$^{55}Mn(n,\gamma)\,^{56}Mn$	Thermal	846.76 (98.85%)	9284.04
		Epithermal	1810.73 (26.89%)	
			2113.09 (14.23%)	

Table 3.2 Activation wire materials, reactions, γ energies, and half-lives
Material compositions, reactions of interests, activation energy range, product gamma ray energies, and product half-lives for activation wires used in this research. For reactions with multiple photon energies, only lines with intensities above 5% are listed. [19,24,25]

Aluminum, cobalt, and indium acted as combination fast and thermal detectors. Aluminum possessed three reactions of interest: $^{27}Al(n,\gamma)^{28}Al$, $^{27}Al(n,\alpha)^{24}Na$, and $^{27}Al(n,p)^{27}Mg$. The thermal $^{27}Al(n,\gamma)^{28}Al$ reaction had the advantage of a 2.241(1) min half-life allowing it to quickly reach saturation activity. [24] $^{27}Al(n,\alpha)^{24}Na$ and $^{27}Al(n,p)^{27}Mg$ are threshold reactions at 3.8 and 4.9 MeV respectively, useful for measuring fast neutron reaction rates. [19] The $^{27}Al(n,p)^{27}Mg$ was judged more useful for the GMIS system as the 9.458(12) min half-life allowed it to reach saturation activity in reasonable irradiation times for the generator while the 14.997(12) h half-life for $^{27}Al(n,\alpha)^{24}Na$ was prohibitively long. Cobalt had two reactions of interest: $^{59}Co(n,\gamma)^{60m}Co$ and $^{59}Co(n,\alpha)^{56}Mn$. Cobalt was chosen for its short half-life: 10.467(6) min for the thermal $^{59}Co(n,\gamma)^{60m}Co$ and 2.5789(1)h for the 5.2 MeV $^{59}Co(n,\alpha)^{56}Mn$ threshold reaction. However, the $^{59}Co(n,\alpha)^{56}Mn$ and $^{55}Mn(n,\gamma)^{56}Mn$ reactions shared a product so two wires could not be irradiated at the same time. Indium offered two primary reactions of interest, one thermal, $^{115}In(n,\gamma)^{116m}In$, and one fast, $^{115}In(n,\gamma)^{115m}$. The thermal reaction offered a relatively large cross section and short half-life, 160 b and 54.29(17) min respectively. The fast reaction offered two major advantages: a low threshold energy of 0.5 MeV and a short half-life of 4.5 h. The 0.5 MeV threshold was below the 2.45 MeV neutrons from the DD generator but still well above thermal and epithermal levels enabling direct measurement. Indium also presented competing thermal reactions from $^{113}In(n,\gamma)^{114m}In$ and $^{113}In(n,\gamma)^{114}In$ which possessed unfavorable half-lives or low cross-sections. Dysprosium was chosen as thermal and epithermal detector. The $^{164}Dy(n,\gamma)^{165}Dy$ reaction offered an excellent thermal cross-section over

800 b with a short 2.334(1)h half-life and when covered in a cadmium tube provided an estimate of the epithermal flux. Manganese similarly functioned as a thermal and epithermal detector due to the $^{55}Mn(n,\gamma)^{56}Mn$ reaction's resonance integral at 337 eV. Manganese also offered a comparable half-life of 2.5789(1) h to dysprosium which meant the materials could be irradiated and counted simultaneously and then directly compared.

3.2.2. Irradiation Measurement Campaign

After the materials were selected a measurement campaign was planned. The initial version identified eight sites for wires: four on the surface of the generator and four on the exterior sides of the target boxes. The sites would be measured twice, once in an empty cavity and once in the fully loaded system. All sites were located along the cardinal axes at a height level with the apex of the generator target corresponding to the midpoint of the DU target sheets. Each site was assigned a number and a full set of foils would be irradiated at each site, see Figure 3.2.

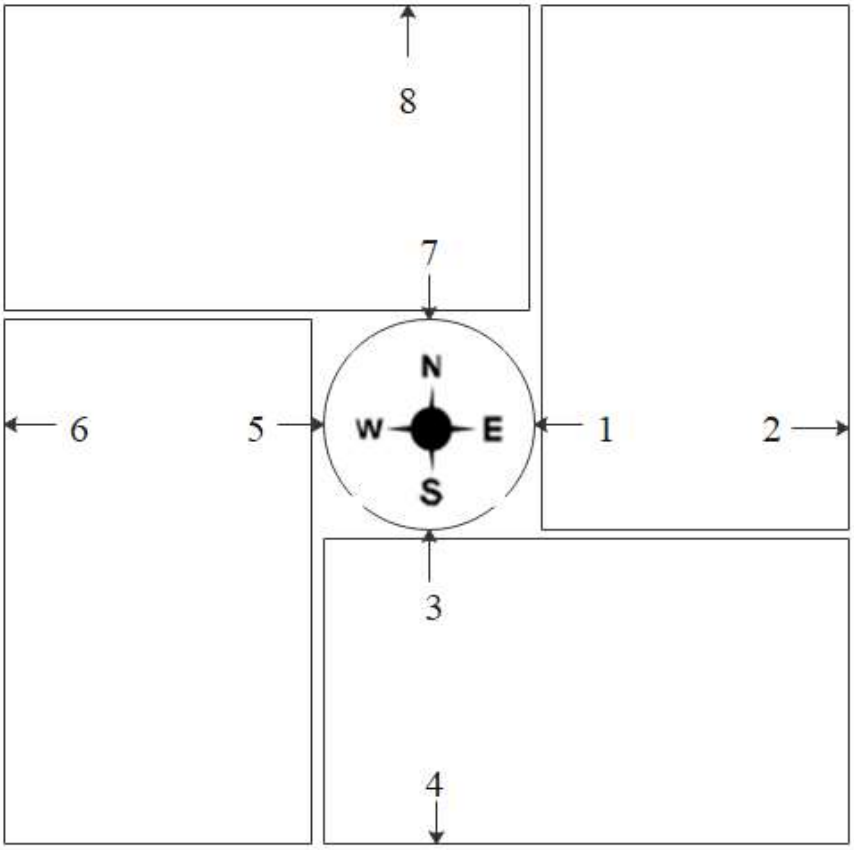

Figure 3.2 Planned activation measurement campaign irradiation sites**.** Separate full sets of wires would be irradiated at each position sequentially. Vertical level was even with the apex of the generator target corresponding to the midpoint of the DU sheets.

Each set of foils would be irradiated for a total of 30 h. This period was chosen for several reasons. It maximized the induced activity in the longer product half-life reactions while still being within the known operating limits of the generator. The aluminum, cobalt, and indium wires would be irradiated for the full duration. This would allow the cobalt and indium reactions of interest to reach saturation activity while the $^{27}Al(n,\alpha)^{24}Na$ reaction would only reach 86%. The period would also allow for the

irradiation of multiple dysprosium and manganese wires at each site. After 10 h, dysprosium and manganese wires would reach 98.6% and 97.9% of saturation activity respectively. Bare and cadmium-covered wires would be irradiated at the same time to ensure both were exposed to the same flux. The cadmium-covered wires would be counted first for one half-life followed by the bare wires as the bare wires were expected to have a high saturation activity. This arrangement would allow for direct comparison to determine the cadmium ratio. It would also prevent the manganese and cobalt activities from conflicting with each other.

Unfortunately, a series of mechanical and logistical failures resulted in drastic modification to this plan. Due to manufacturing delays, the on-site HPGE detector was not received in June 2017 as originally scheduled but installed on 1 December 2017. Attempts to secure alternative or off-site equipment during the interim period failed due to a lack of availability in the area and funding. While awaiting delivery, GMIS continued working on projects for other costumers including the lithium irradiation for Mission Support and Test Servics, LLC (MSTS) the operating contractor of the NNSS. Two samples of natural lithium (2.15 g and 2.25 g) were irradiated in a vacuum tight steel container for 6 h. During the course of this work, the generator overheated and failed due to a lack of Flourinert® coolant in September 2017. While all remaining on-hand coolant was used to refill the generator; general supplier shortages prevented ordering replacement coolant. The generator continued to behave somewhat erratically after this event, experiencing sudden drops and surges in beam power which indicated varying neutron output. Independent analysis of the lithium using liquid scintillation

counting was performed by the University of Nevada, Las Vegas Radiochemistry department with the assistance of GMIS personnel at the direction of MSTS. UNLV reported tritium formation rates of 49.2 kBq to 190.6 kBq g^{-1} hr^{-1}. MCNP results remained unchanged and still differed by 4 to 5 orders of magnitude. Due to extensive concerns raised by scientists at Los Alamos National Laboratory about neutron economy, MSTS directed GMIS to perform a direct measurement of tritium production from $LiCO_3$ in the gaseous phrase using an Overhoff Model 311 tritium monitor that had previously been purchased for the project.

In preparation from this measurement campaign, extensive document review of the GMIS records by the Author and Dr. Raymond Keegan in October 2017 revealed significant errors by the GMIS staff in calculations for the ^{99}Mo yield estimate of 7400 MBq. Measurements had been performed with 2”X4”X16” NaI(Tl) detector using a single point energy calibration from a ^{137}Cs and no efficiency calibration resulting in a misidentified ^{99}Tc peak. This was compounded by further calculation errors. Assuming a 37 kBq ^{137}Cs source, no efficiency correction for the difference in energies, and a correctly identified peak, the actual production may be to estimated closer to 148 Bq. As a result of these findings, GMIS temporarily stopped all other work pending internal review.

GMIS resumed work in December 2017 with a significantly lower estimate of the neutron flux in the system and a heavy emphasis on the lithium irradiation direct gaseous measurement. The lowered flux estimate resulted in an estimated irradiation time of over 100 hours with the polyethylene block in place to meet the Overhoff's

minimum detectable activity. As a result, activation work was administratively limited to single shifts with the requirement that some additional time was put on the lithium sample during each shift. Additionally, the system was not designed for repeated reconfiguration. To gain access to remove the HDPE block, the top and east shielding walls had to be removed along with one of the target boxes. As only a single hand powered crane was available, this process took an estimated 0.5 to 1 h at the beginning and end of every activation cycle. Total run time was thus limited to <8 h requiring massive reductions to planned irradiation times. Shortened run times also resulted in short count times as the detector was needed to count the fresh samples from the system sooner. As further constraint, GMIS intended to shutter its Las Vegas operations and relocate the generator to its Oak Ridge facility in mid 2018.

Planned irradiations times were reduced for all materials. The plan was optimized to acquire as much data as possible before system relocation rather than maximize induced activities. After configuring the system, the generator would be run for 30 minutes to ensure a stable output. As activation wires were integral detectors, wild variations in generator neutron output would complicate steady state neutron flux analysis. After achieving stability, the aluminum, cobalt, and indium wires would be run simultaneously. The aluminum wire would be removed after 30 min. This was to allow the $^{27}Al(n,p)^{27}Mg$ reaction to reach 96% full activity. The cobalt wire would be replaced after 160 min (one half-life), reaching 63% full activities, with a bare dysprosium wire. The bare dysprosium and indium wires would be removed together at the 270 min mark and replaced with cadmium-covered dysprosium and bare manganese wires, which

would be irradiated for 160 min. Cadmium-covered dysprosium was preferred over manganese due to the larger cross-section differences between thermal and epithermal neutrons. The system would then be rebuilt for lithium irradiation. Wire activation would still occur at all 8 sites in sequential order.

The on-site HPGE, a mechanically cooled ORTEC GEM50-83, was installed on 1 December 2017 and chilled to operating temperatures. The ORTEC Gammavision software package was used to record all spectra.[26] The detector was energy calibrated to a 3 MeV scale using a 34.66 kBq ±3% ^{152}Eu source, assay date of 1 October, 2017 NIST traceable SN AK-7791. An extended 118,800 s efficiency calibration was conducted using the same source centered directly on the plastic shield of the detector end-cap; see Figure 3.3 for the resulting efficiency curve. Wire counts were performed in the same geometry. 600 s background counts and calibration checks with the ^{152}Eu source were performed on the day of every wire activation measurement. A 120 min background recorded during system operation revealed no significant effect on background count rates from the generator's operation. A sample background and calibration spectra may be seen in Figure 3.4. Activation spectra are included in Appendix C.

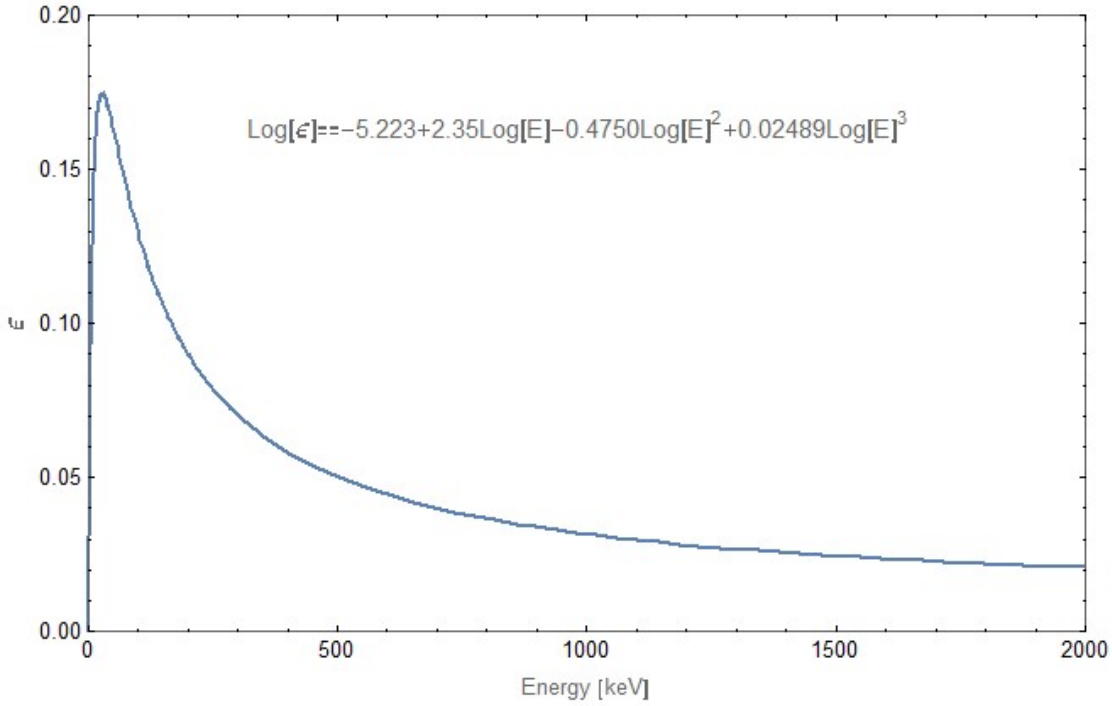

Figure 3.3 HPGE efficiency curve from a 118,800 s calibration using a 34.66 kBq ^{152}Eu source in contact with the center of the detector end-cap**.**

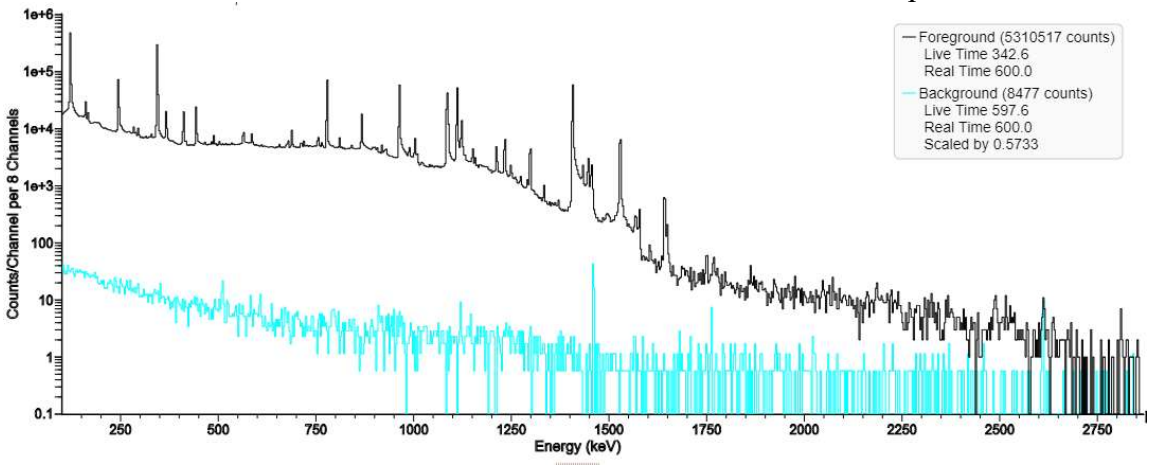

Figure 3.4 Sample calibration and background spectra taken on 6 December 2018. Background spectrum was normalized to the same live time as the calibration spectrum to facilitate easy comparison.

Activation wires were prepared in advance. Wires were cleaned with isopropyl alcohol and handled with tweezers and gloves to avoid contamination. Approximately, 2 cm lengths of wire were cut and weighed on a mass balance accurate to 1 mg. For cadmium-covered wires, a slightly oversized section of cadmium tubing was cut. One end was crimped with pliers, the wire inserted into the tube, and the other end was crimped shut. The ends were folded over to ensure complete coverage of the contained wire. Wires were laid length-wise in the bottom of individual paper envelopes, 5.72 cm X 8.89 cm, and sealed with scotch tape. A hole was punched in each envelope through which a zip tie was threaded to permit rapid removal from the generator cavity.

For all irradiations performed in this work the generator was operated at accelerating voltages between 110 to 125 kV, typically 120 kV. The operators attempted to maintain a constant power level primarily through adjustments to the deuterium gas flow rate. If the generator drifted above or below the target power, the mass flow would be increased or decreased as needed. However, long term drifts in the power level would exceed the dynamic control range offered by this technique periodically requiring adjustments to the accelerating voltage. These adjustments were performed in 5 kV steps.

Wire activation work began on 5 December 2017. The system was reconfigured for activation work and operated for one hour to ensure system stability at a consistent power level of 1600 ± 20 W measured from deuteron beam current and target accelerating potential. The generator was then shut off and the aluminum, cobalt, and indium wires were mounted on the east side of the generator, position 1. The envelopes

were secured to the generator surface using electrical tape. The aluminum and cobalt wires were respectively placed a few millimeters above and below the direct centerline on the generator to ensure the wires did not directly overlap; the indium was directly on the marked centerline. The generator was run for 30 minutes at 1600 ± 20W then stopped. The aluminum wire was removed, immediately transferred to the HPGE, and counted for 4,200 s. Irradiation was successfully resumed immediately and continued until 150 min after the initial start time. The generator was stopped and the cobalt wire removed and counted for 6,180 s. Irradiation was resumed until 270 min after initial start; the indium wire was removed and counted for 16,200 s. Midway through this count, manganese and cadmium covered dysprosium wires were inserted into the reactor cavity at position 1 and irradiated for 160 min before being counted for 9,600 s. The wires were replaced with manganese and bare dysprosium wires which were irradiated for 240 min, then counted for 9,600 s. On 6 December 2017 manganese and dysprosium wires, both bare and cadmium covered, were placed on the east wall, position 2, of the empty cavity for 160 min irradiation times and 9,600 s count times. Deviations from the planned irradiation methodology were due to miscommunication between the author and GMIS staff, resulting in overlap.

Additional validation work was delayed as the generator began to experience random power drops, recovering after a few minutes to a lower power. GMIS continued using the generator for other work that was not as sensitive to fluctuations in neutron fluxes. During this work, the single post RF tuner used to modulate the power from the magnetron failed catastrophically. The on-hand replacement tuner failed after several

days of operation. The cause was determined to be reflected power from metallization build-up on the ceramic window between the magnetron and the plasma chamber. Metal fragments from the plasma chamber walls would be gradually deposited on the ceramic changing the RF properties; the resulting reflection caused the tuner burn out. A replacement tuner and ceramic window were sent by the generator manufacturer.

However, the manufacturer erroneously sent both the tuner and window for their updated model of generator. While the tuner was capable of physically interfacing with the system, it did not respond to the software control system. To temporarily overcome this, a direct voltage connection was wired from the control station to the tuner allowing the post position to be manually adjusted by directly applying a voltage signal to the stepper motor. A replacement ceramic window arrived later, but was improperly machined to the wrong diameter and did not fit the DD109 generator causing further delays. The system was not available for activation work until 15 February 2018.

The system was reconfigured with the four DU target boxes in place, but without reflectors due to the previously mentioned swelling. Aluminum, cobalt, and indium wires were prepared and mounted on the generator as previously described. The cobalt wire was removed after 145 min and counted for 6360 s. The generator spontaneously shut down at 263 min, so the aluminum and indium wires were immediately removed and counted together for 16,200 s. The shutdown was determined to have been caused by overheating. The generator was experiencing a slow leak of coolant that accelerated while the generator was operating. Replacement coolant had still not been ordered for the generator. Instead, excess waste Flourinert® that had been recovered after the

generator's exterior resistor bank failed in 2016 was reclaimed. The material was filtered to remove foreign debris then purified through distillation. After refilling with coolant, the generator continued to operate erratically and lower power output. Validation work was paused until the cause could be determined while the $LiCO_3$ irradiation continued. A small coolant leak continued unabated, so the remainder of the reclaimed coolant was added to top off the generator. An alternate coolant fluid was identified by GMIS staff and approved by the generator manufacturer. A major coolant leak occurred on 19 February 2018 when the 1/2" polyethylene return line failed due to degradation and dumped several gallons of coolant on the floor. Remaining polyethylene lines in the system were replaced with stainless steel where practicable while fresh polyethylene lines were used to make bendable joint connections. A mix of original and alternate coolant was required to reach sufficient operating levels. A small dripping coolant leak continued and roughly 2 L of fluid had to be added the next day. Generator output stabilized and activation wire work was resumed on 23 February 2018.

The system was reassembled with the four target boxes and the generator was operated for 30 min at a power level of 1,500± 30 W. Aluminum, cobalt, and indium wires were prepared as before and inserted on the interior east wall of the cavity, position 2. After 160 min, the cobalt wire was removed and counted for 5,245 s. After 247 min, the generator power level dropped to 1,300 W. The aluminum and indium wires were removed rather than irradiated at a varying power level. The two wires were counted for 16,200 s. Validation work continued on 26 February 2018 after the system was allowed to recover. Bare dysprosium and manganese wires were irradiated at

position 3 for 160 min then removed and counted for 9,600 s. These were replaced with cadmium covered dysprosium and bare manganese wires which were irradiated at position 2 for 160 min then removed and counted for 9,600 s. The bare manganese wire was used as a control to ensure the total flux was comparable for the both irradiations. Power levels were maintained at 1,400 ± 30 W throughout both irradiations. No further validation work was performed after this point. GMIS required that the focus be on reaching 200 h of irradiation on the $LiCO_3$ sample. Approximately 190 h were achieved on the sample before subsequent coolant leaks and mechanical failures left the system inoperable pending its decommissioning and removal to the Oak Ridge site in summer 2018.

Spectra were recorded using Gammavision and analyzed using InterSpec. [26,27] Net peak areas were determined assuming a linear continuum. However, some products could not be distinguished from the count continuum and were below the MDA. In practice, the MDA for each peak was calculated for the critical level specific to each spectrum since continuum counts from higher energy photons will effect counts for lower energy peaks.[28] As a useful lower bound, nominal MDAs for each of the product photon lines identified in Table 3.2 were calculated using a 2.304×10^5 s background recorded on 12 January 2018 assuming a 3 keV region for all peaks, see Table 3.3. Saturation activities were calculated using Eq. 26 and net peak areas assuming a linear continuum. Results are discussed in section 4.1.1. Measured wire activities were input into SANDII and used to generate neutron energy spectra. SANDII and MCNP neutron energy spectra are compared in section 4.1.3.

Reaction	Energy [keV]	BKGRD Counts	Eff.	Yield	Count Time [s]	MDA [Bq]	σ_{MDA} [Bq]
$^{27}Al(n,\gamma)\ ^{28}Al$	1778.99	317.7	0.0222	1.0000	4200	0.118	0.002
$^{27}Al(n,\alpha)\ ^{24}Na$	1368.63	808.5	0.0260	0.9999	4200	0.144	0.002
	2754.01	36.7	0.0176	0.9986	4200	0.078	0.003
$^{27}Al(n,p)\ ^{27}Mg$	843.76	2311.2	0.0355	0.7180	4200	0.229	0.002
	1014.52	1684.6	0.0314	0.2820	4200	0.575	0.006
$^{164}Dy(n,\gamma)\ ^{165}Dy$	94.7	23659	0.1336	0.0381	9600	2.222	0.007
	361.68	7245.7	0.0625	0.0090	9600	11.304	0.063
$^{59}Co(n,\gamma)\ ^{60m}Co$	58.6	19466	0.1583	0.0207	9600	3.136	0.011
$^{59}Co(n,\alpha)\ ^{56}Mn$	846.76	2317.3	0.0354	0.9885	9600	0.107	0.001
	1810.73	299.8	0.0220	0.2689	9600	0.262	0.006
	2113.09	373.8	0.0202	0.1423	9600	0.590	0.012
$^{113}In(n,\gamma)\ ^{114m}In$	190.27	16695.7	0.1652	0.1608	16200	0.278	0.001
$^{113}In(n,\gamma)\ ^{114}In$	1299.83	1087.8	0.0268	0.0014	16200	53.810	0.741
$^{115}In(n,\gamma)\ ^{116m}In$	1293.56	1124.7	0.0269	0.8488	16200	0.090	0.001
	1097.28	1581.9	0.0299	0.5857	16200	0.137	0.002
	416.90	5877.2	0.0569	0.2725	16200	0.287	0.002
	2112.29	279.7	0.0202	0.1511	16200	0.366	0.009
	818.68	2266.4	0.0362	0.1213	16200	0.646	0.006
	1507.59	955.3	0.0245	0.0993	16200	0.784	0.011
$^{115}In(n,n')^{115m}In$	336.24	8297.5	0.0656	0.0482	16200	1.664	0.009
$^{55}Mn(n,\ \gamma)\ ^{56}Mn$	846.76	2317.3	0.0354	0.9885	9600	0.107	0.001

Table 3.3 Activation wire minimal detectable activities

Minimal detectable activities for each activation wire reaction calculated from a 2.304×10^5 s background recorded on 12 January 2018. These values are offered as a lower boundary estimate. In the presence of detectable activities, continuum photons from higher energy peaks will raise the MDA values for lower energy peaks. The calculated detector efficiency at each energy and expected yield of each photon energy are also included.

3.2.3. Neutron Generator Yield Calculations

Due to both fluctuations in the generator's output power during activation work and MCNP's normalization to the source strength, it was necessary to estimate the neutron yield as a function of voltage and beam power. Ideally, this would have been

accomplished through empirical measurements. However, the general paucity of available proper neutron detection instrumentation and the eventual mechanical failure of the system rendered this approach impossible. A theoretical yield curve had to be derived instead.

In the case of a monodirectional, monoenergetic beam incident on a target, Eq. 19 may be rewritten as:

$$Y(E) = \varphi\sigma(E)n\Delta x \qquad \text{(Eq. 32)}$$

where *Y(E)* is the energy dependent reaction yield, φ is the flux of incident particles [s^{-1}], $\sigma(E)$is the energy-dependent microscopic reaction cross-section [cm^2], n is the atomic density of the target [atoms cm^{-3}], and Δx is the thickness of the target [cm]. For a thick target, particle energy decreases with target thickness. Converted to differential form with a change of variables, this becomes:

$$\mathrm{d}Y(E) = \varphi\sigma(E)n\mathrm{d}x \qquad \text{(Eq. 33)}$$

$$\mathrm{d}x = \frac{\mathrm{d}x}{\mathrm{d}E}\mathrm{d}E = \frac{\mathrm{d}E}{S(E)} \Rightarrow Y(E_0) = \varphi n \int_{E=0}^{E_0} \frac{\sigma(E)}{S(E)} dE \qquad \text{(Eq. 34)}$$

where $(E) = \frac{\mathrm{d}E}{\mathrm{d}x}$, more commonly known as the linear energy transfer (LET). After assuming a 1:1 Ti:D loading factor for the generator target, LET values for D ions in TiD were calculated using the program SRIM. [29] Using these values and evaluated cross-section data for the D-D reaction, neutron yields were calculated through numerical integration of Eq. 34 from 0 to 200 keV. [9] The target atomic density was estimated to be $n=1.14\times10^{23}$ atoms cm^{-3} based on the size and thickness of the Ti layer

while the flux was set to $\varphi = 6.241 \times 10^{15}$ [D ions s^{-1}], corresponding to 1 mA of beam current. See Figure 3.5 for the resulting curve.

By comparing the measured accelerating voltage and beam power to this curve, the functional neutron yield of the generator during each irradiation could be estimated.

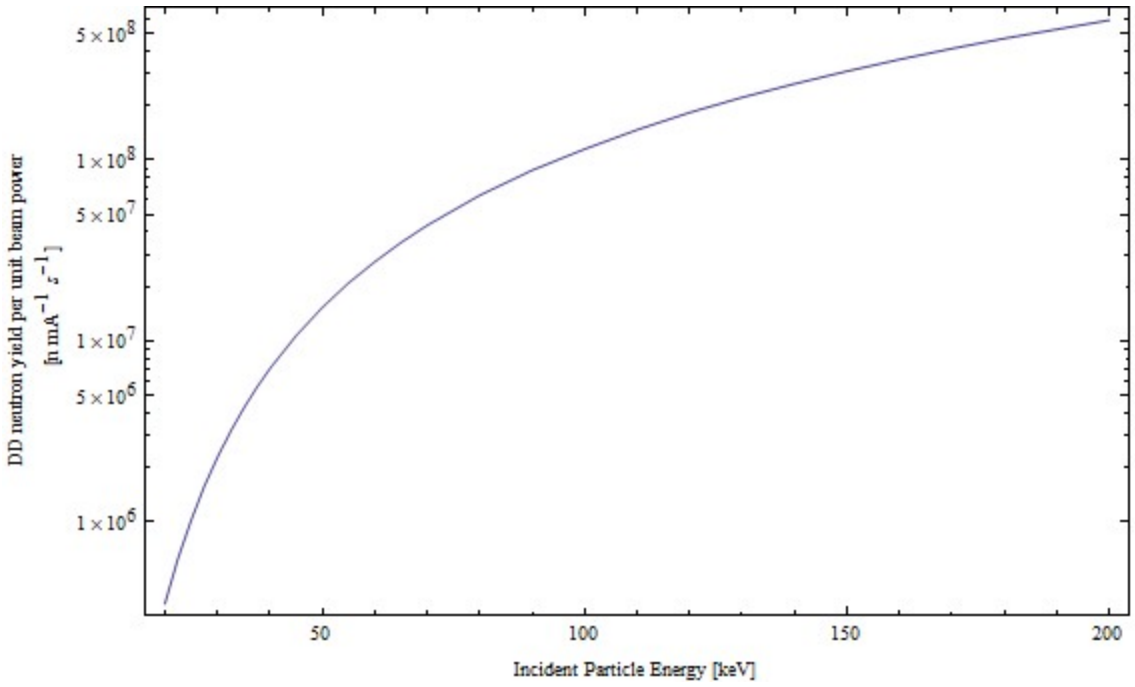

Figure 3.5 Estimated target D-D neutron yield.
Estimated target D-D neutron yield per mA of beam current with incident particle energies between 0 and 200 keV. The generator accelerating potential was held between 110 kV to 125 kV for this research. A 13.3 mA D+ beam accelerated at 120 kV would yield 2.43×10^9 n s^{-1} with a measured beam power of 1600 W.

3.2.4. MCNP Model Wire Activation

The MCNP simulations were performed to provide two different methods of validation: activation rate calculations and full energy spectra. The model was updated to match the physical changes to the system in each irradiation, including the addition of materially accurate wires. The rates for each reaction of interest were estimated directly

using F4 tallies and multipliers when possible; see section 4.2. The full energy neutron spectrum was estimated at each position using the SANDII 620 energy group structure for later comparison; see section 4.3.

The MCNP model was updated to accurately represent the irradiation conditions. Simulations were performed with two system configurations, with and without uranium target boxes, and three wire compositions for a total of six runs. The wire compositions were aluminum, cobalt, and indium; bare dysprosium and manganese; and cadmium-covered dysprosium and manganese. Wire material compositions were obtained from the manufacturer's literature. [25] In both configurations, two identical sets of wires were added at positions 1 and 2 simultaneously. The wires were modeled as perfect 2 cm long cylinders parallel to the X axis (north-south). All wires had diameters of 0.0762 cm except cobalt which had a diameter of 0.0381 cm. The cadmium cover tubes were represented by annular cylinders with respective internal/external diameters of 0.127 cm and 0.229 cm; 0.102 cm caps were included at each end to account for the crimped material to ensure complete thermal neutron coverage making the total length 2.204 cm. Cylinders were inserted 0.115 cm from the nearest system surface, the generator's exterior for position 1 and the east cavity wall for position 2. The indium and dysprosium cylinders were centered at the vertical apex of the generator target; the aluminum and manganese cylinders were placed 0.5 cm above while the cobalt cylinder was place 0.5 cm below. The cylinders were suspended in midair; extraneous features such the envelopes, tape, and zip ties, were not included as minimal effects on the neutron flux did not merit their added complexity.

F4 tallies were used to calculate the energy-dependent neutron flux through each cylinder. Multiplier cards were used to calculate individual isotopes' reaction rates for aluminum, dysprosium, indium, and manganese. Isotopically pure material compositions, scaled to the appropriate atomic density [atoms b^{-1} cm^{-1}] for the given wire's recorded mass and elemental isotopics, were substituted for calculations. Cobalt was not used because the (n,γ) stable and meta-stable products could not be extracted separately. The problem was run as fixed source calculations with a surface source for 200 megahistories. Generator source strength was estimated for each irradiation based on the neutron yield curve developed in Section 3.2.3. Additional error was introduced by the power and voltage fluctuations. A discussion of the results is located in Section 4.2.

3.2.5. MCNP Source Efficiency

Additional MCNP runs were performed to determine the φ^* and k_s for the system. Two configurations were considered: (1) only target boxes present and (2) target boxes and reflectors present. A criticality mode calculation was used to estimate k_{eff} for both configurations using 100 cycles, 2,000 particles per cycle, discarding the first 20 cycles, with an initial k_{eff} estimate of 0.27. A 1 megahistory fixed source calculation was used to calculate the total fissions and total fission neutrons using F4 tallies in all uranium-containing cells for both configurations. Since fixed source problems are normalized to the starting source strength, the MCNP output for total fission neutrons is equivalent to $\langle P_s \boldsymbol{\phi}_s \rangle / \langle \boldsymbol{S} \rangle$. Using these parameters, the source efficiency and system power were calculated using Eq. 8 and Eq. 16 respectively. For calculation purposes, the

average number of neutrons per fission was obtained by dividing the MCNP estimate for fission produced neutrons by the number of fissions. An average fission energy of 196.54 MeV was used, as MCNP results indicated the primary source of fissions was ^{238}U.[9] A source strength of $2.43x10^{9}$ n $s^{-1}$was used based on a 1,600 W generator beam power at standard operating parameters. Results are presented in section 4.4.

4. RESULTS

This chapter presents the results of the activation wire spectroscopy measurements, the MCNP tally results, and the SANDII generated spectra.

4.1. Wire Spectroscopy and Saturated Activity Results

The activation wires were counted immediately after irradiation. Only three isotopes of interest were detected: ^{115m}In, ^{116m}In, and ^{56}Mn. No detectable activity was found from any of the aluminum, cobalt, or dysprosium reactions. Figures 4.1-4.4 show sample spectra from each wire with the nuclides causing major peaks identified. All cobalt wire spectra were indistinguishable from background with no expected peaks visible. The indium and aluminum wire spectra revealed several expected peaks from the ^{115}In(n,γ)^{116m}In and ^{115}In(n,n')^{115m}In reactions but none from the aluminum reactions. Similarly, the manganese and dysprosium-aluminum spectra showed the expected ^{56}Mn peaks but none from dysprosium. Several capture lines from the cadmium cover were also visible in the spectra. Spectral data for the observed peaks are listed in Table 4.1.

.

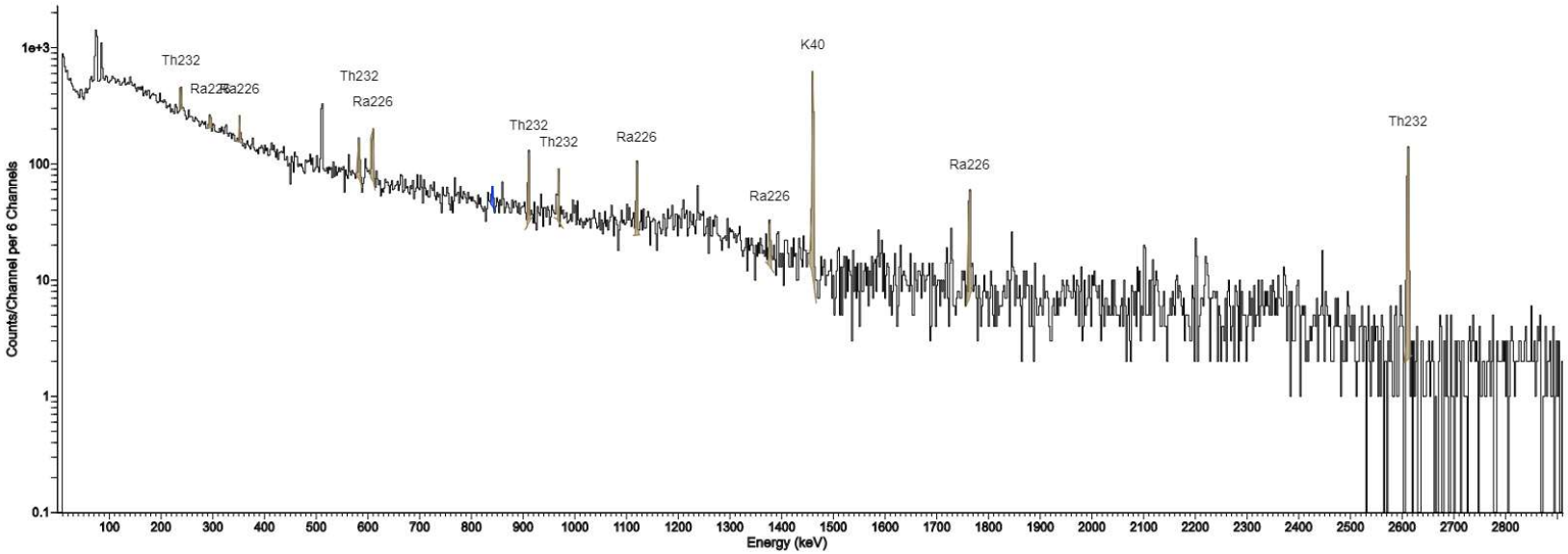

Figure 4.1 Activated Co wire spectra on 23 February 2018 after 160 min irradiation at position 1 in full cavity. There is no detectable activity from the cobalt wire. Identified background peaks from NORM including ^{40}K, ^{232}Th, and ^{226}Ra are present in all subsequent spectra but are most visible here. Additional unlabeled peaks present in all spectra include the xray peaks from the lead shielding between 70 to 100 keV and the 511 keV annihilation peak from pair production.

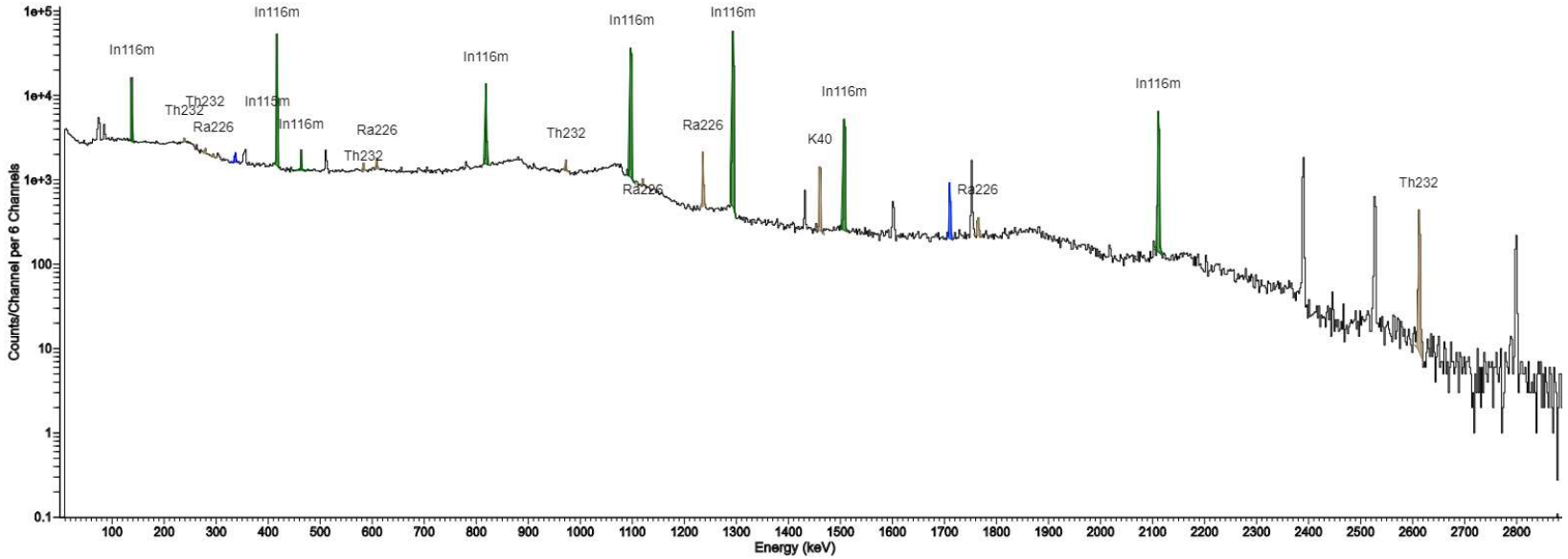

Figure 4.2 Activated Al and In wire spectra on 23 February 2018 after 270 min irradiation at position 1 in full cavity. There is no detectable activity from the aluminum wire. Peaks from ^{116m}In and ^{115m}In are identified and labeled along with several background peaks. Noticeable sum peaks are observed from ^{116m}In at 2390 (1097+1293) keV, 2528 (417+2112) keV, and 2799 (1293+1507) keV.

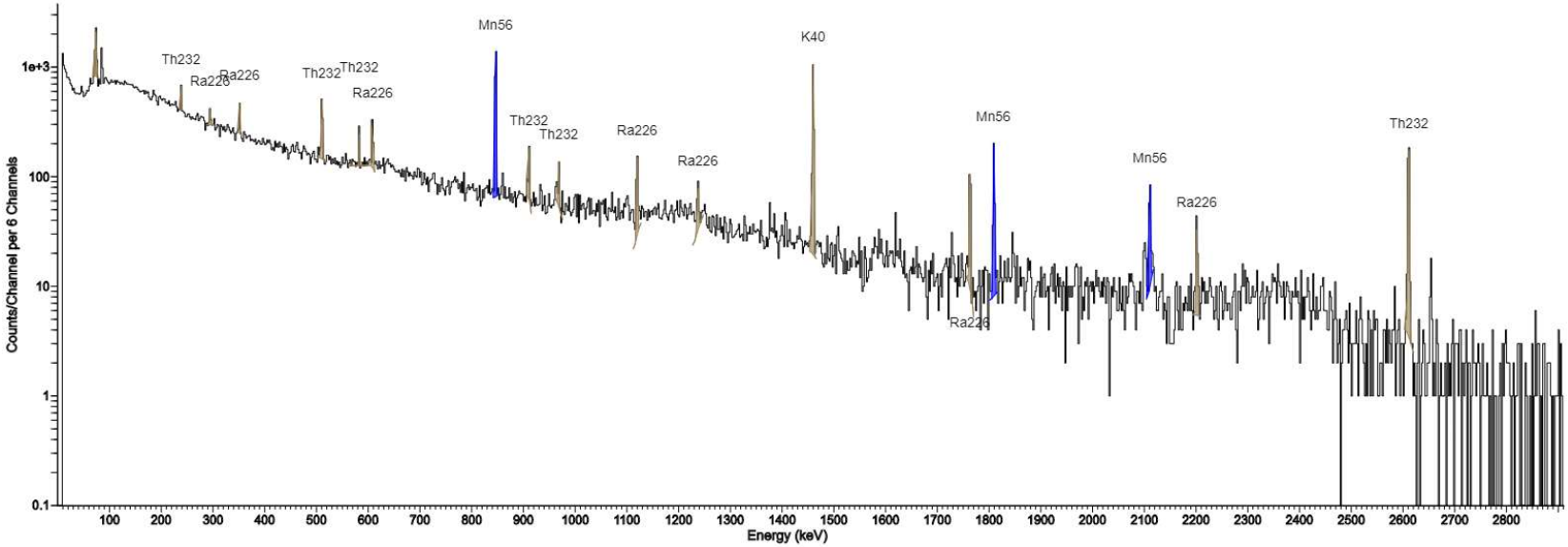

Figure 4.3 Bare Dy-Al and Mn wire spectra on 26 February 2018 after 160 min irradiation at position 1 in full cavity. There is no detectable activity from the Dy-Al wire. Peaks due to ^{56}Mn are identified and labeled along with several background peaks.

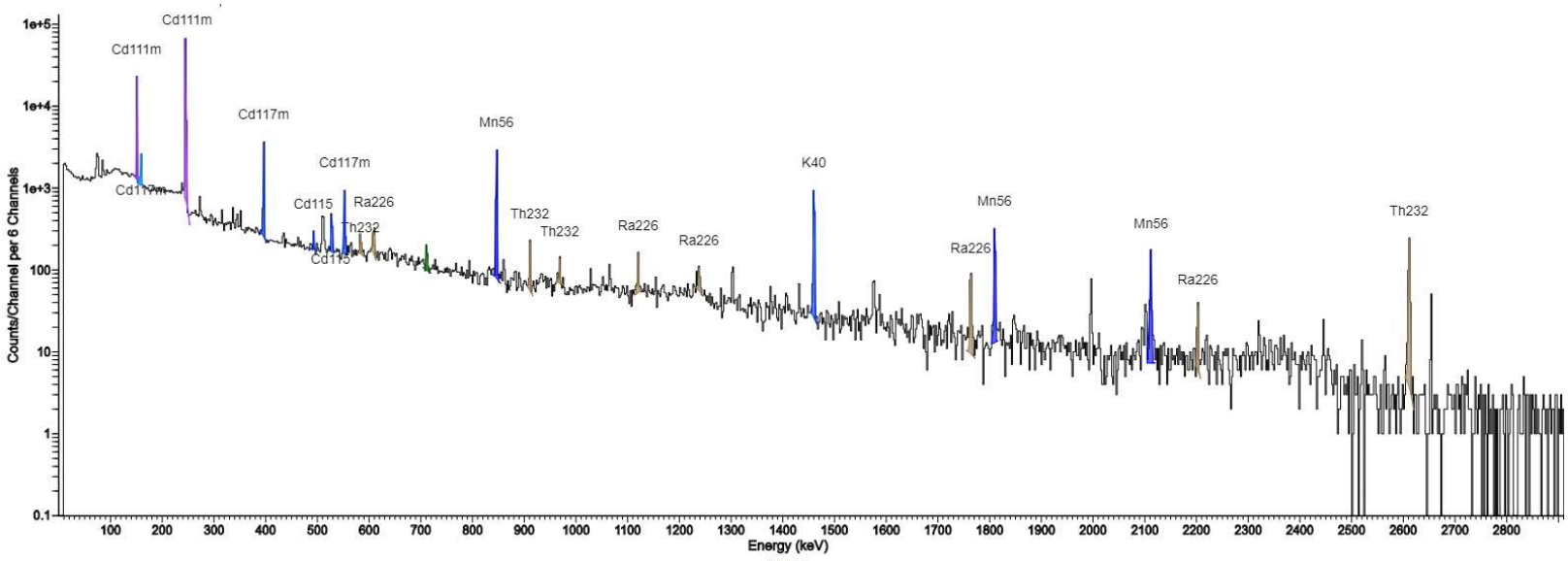

Figure 4.4 Cd(Dy-Al) and bare Mn wire spectra on 26 February 2018 after 160 min irradiation at position 1 in full cavity.. There is no detectable activity from the Dy-Al wire. Peaks due to ^{56}Mn are identified and labeled. Cadmium capture and several peaks are also identified and labeled.

Table 4.1 Recorded spectral features from activation wire spectra

Nuclide	Energy [kev]	Yield	ε	Centroid [keV[	Net Area	$\sigma_{\text{Net Area}}$	FWHM [keV]	Live-Time [s]	Date M-D-Y	T_{irr} [s]	A_∞ [Bq]	$\sigma_{A\infty}$ [Bq]
^{115m}In	336.24	0.458	0.0654	336.28	30781.9	179.4	1.09	16121.62	12-5-17	16200	176.74	8.90
^{116m}In	416.9	0.272	0.0568	416.91	20431.0	147.7	1.16	16121.62	12-5-17	16200	309.52	15.64
^{116m}In	818.68	0.121	0.0362	818.66	4717.1	75.7	1.49	16121.62	12-5-17	16200	252.27	13.25
^{116m}In	1097.28	0.585	0.0299	1097.12	21829.6	151.3	1.63	16121.62	12-5-17	16200	292.36	14.76
^{116m}In	1293.56	0.848	0.0269	1293.25	27205.1	167.1	1.74	16121.62	12-5-17	16200	278.93	14.05
^{116m}In	1507.59	0.099	0.0245	1507.06	3025.8	57.9	1.88	16121.62	12-5-17	16200	291.91	15.63
^{116m}In	2112.29	0.151	0.0202	2110.56	3446.3	60.3	2.23	16121.62	12-5-17	16200	264.75	14.02
^{115m}In	336.24	0.458	0.0654	336.07	1757.9	51.5	1.11	16129.38	12-12-17	16200	10.08	0.58
^{116m}In	416.9	0.272	0.0568	416.65	10982.1	109.3	1.14	16129.38	12-12-17	16200	165.07	8.42
^{116m}In	818.68	0.121	0.0362	818.15	2326.5	54.6	1.36	16129.38	12-12-17	16200	123.44	6.82
^{116m}In	1097.28	0.585	0.0299	1096.44	12247.4	114	1.61	16129.38	12-12-17	16200	162.74	8.28
^{116m}In	1293.56	0.848	0.0269	1292.45	14900.1	123.9	1.72	16129.38	12-12-17	16200	151.57	7.68
^{116m}In	1507.59	0.099	0.0245	1506.14	1678.4	43.4	1.82	16129.38	12-12-17	16200	160.65	9.04
^{116m}In	2112.29	0.151	0.0202	2109.27	1861.4	44.8	2.18	16129.38	12-12-17	16200	141.87	7.87
^{115m}In	336.24	0.458	0.0654	336.42	13110.8	120.7	1.02	16100.69	2-15-18	15793	85.73	4.36
^{116m}In	416.9	0.272	0.0568	417.09	29057.8	175	1.09	16100.69	2-15-18	15793	446.83	22.50
^{116m}In	818.68	0.121	0.0362	819.08	6750.1	90.5	1.4	16100.69	2-15-18	15793	366.42	18.97
^{116m}In	1097.28	0.585	0.0299	1097.71	31505.7	181.8	1.57	16100.69	2-15-18	15793	428.30	21.56
^{116m}In	1293.56	0.848	0.0269	1293.97	39099.8	199.5	1.69	16100.69	2-15-18	15793	406.91	20.45
^{116m}In	1507.59	0.099	0.0245	1507.92	4221.3	67.7	1.82	16100.69	2-15-18	15793	413.37	21.71
^{116m}In	2112.29	0.151	0.0202	2111.86	5187.9	73.5	2.11	16100.69	2-15-18	15793	404.53	21.02

Table 4.1 Cont

Nuclide	Energy [kev]	Yield	ε	Centroid [keV[	Net Area	$\sigma_{\text{Net Area}}$	FWHM [keV]	Live-Time [s]	Date M-D-Y	T_{irr} [s]	A_∞ [Bq]	$\sigma_{A\infty}$ [Bq]
^{115m}In	336.24	0.458	0.0654	336.38	746.8	46.1	0.98	16088.74	2-23-18	16200	4.28	0.34
^{116m}In	416.9	0.272	0.0568	417.03	59806.8	249.3	1.09	16088.74	2-23-18	16200	894.16	44.86
^{116m}In	818.68	0.121	0.0362	818.96	13719.3	129.2	1.39	16088.74	2-23-18	16200	724.09	36.84
^{116m}In	1097.28	0.585	0.0299	1097.56	65070.0	260.6	1.58	16088.74	2-23-18	16200	860.06	43.14
^{116m}In	1293.56	0.848	0.0269	1293.81	80092.0	285.9	1.69	16088.74	2-23-18	16200	810.41	40.62
^{116m}In	1507.59	0.099	0.0245	1507.75	9009.9	98.9	1.85	16088.74	2-23-18	16200	857.83	43.91
^{116m}In	2112.29	0.151	0.0202	2111.65	10450.9	104.8	2.16	16088.74	2-23-18	16200	792.33	40.41
^{56}Mn	846.75	0.9887	0.0354	846.37	2081.9	47.4	1.41	9561	12-5-17	9600	34.99	1.92
^{56}Mn	1810.72	0.2719	0.0220	1809.3	250.7	16.7	2.07	9561	12-5-17	9600	24.63	2.05
^{56}Mn	2113.05	0.1434	0.0202	2110.86	112.4	11.8	1.93	9561	12-5-17	9600	22.83	2.66
^{56}Mn	846.75	0.9887	0.0354	846.73	1881.5	45.3	1.51	9563.5	12-6-17	9600	31.51	1.75
^{56}Mn	1810.72	0.2719	0.0220	1809.73	247.4	16.6	1.98	9563.5	12-6-17	9600	24.23	2.03
^{56}Mn	2113.05	0.1434	0.0202	2111.26	127.7	12.5	2.22	9563.5	12-6-17	9600	25.86	2.84
^{56}Mn	846.75	0.9887	0.0354	847.07	18993.9	139.2	1.42	9555.48	2-26-18	9600	318.50	16.09
^{56}Mn	1810.72	0.2719	0.0220	1810.67	2525.3	51.2	1.94	9555.48	2-26-18	9600	247.59	13.36
^{56}Mn	2113.05	0.1434	0.0202	2112.61	1158.8	34.9	2.12	9555.48	2-26-18	9600	234.91	13.71
^{56}Mn(Cd)	846.75	0.9887	0.0354	846.71	3504.2	60.6	1.43	9553.22	12-5-17	9600	28.90	1.53
^{56}Mn(Cd)	1810.72	0.2719	0.0220	1809.76	457.5	22.3	1.83	9553.22	12-5-17	9600	22.10	1.54
^{56}Mn(Cd)	2113.05	0.1434	0.0202	2111.49	219.7	15.7	2.17	9553.22	12-5-17	9600	21.90	1.91

Table 4.1 Cont

Nuclide	Energy [kev]	Yield	ε	Centroid [keV[	Net Area	$\sigma_{\text{Net Area}}$	FWHM [keV]	Live-Time [s]	Date M-D-Y	T_{irr} [s]	A_∞ [Bq]	$\sigma_{A\infty}$ [Bq]
^{56}Mn(Cd)	846.75	0.9887	0.0354	846.75	3564.6	61.4	1.64	9565.08	12-6-17	9600	29.30	1.55
^{56}Mn(Cd)	1810.72	0.2719	0.0220	1809.7	465.5	22.3	2.08	9565.08	12-6-17	9600	22.30	1.55
^{56}Mn(Cd)	2113.05	0.1434	0.0202	2111.52	233.6	16.1	2.24	9565.08	12-6-17	9600	23.20	1.97
^{56}Mn(Cd)	846.75	0.9887	0.0354	847.02	39962.9	201.5	1.42	9543.76	2-26-18	9600	329.00	16.52
^{56}Mn(Cd)	1810.72	0.2719	0.0220	1810.54	5235	73.8	1.94	9543.76	2-26-18	9600	252.00	13.08
^{56}Mn(Cd)	2113.05	0.1434	0.0202	2112.45	2347.6	49.3	2.12	9543.76	2-26-18	9600	233.00	12.66

Table 4.1 Recorded spectral features from activation wire spectra. The product nuclide with its photo peak energies and associated branching ratios were listed with the detector's calculated efficiency at that energy. A 5% error was assumed for all efficiencies. Reported parameters of the observed peak include centroid, FWHM, and area. The saturation activity was calculated for each peak based on the duration of the irradiation and count period.

Saturation activities were calculated using Eq. 26. The dominating source of error was from the efficiency value, since a 1% change in efficiency value corresponded to a 20% change in the saturation activity uncertainty. The saturation activities values showed strong internal consistency within nuclide and irradiation run, all values agree within 3σ while 76% agree within 2σ or less. Mean saturation activities for each reaction and position were reported in Table 4.2 along with an estimate of the corresponding neutron flux based on average cross section

Nuclide	Position	DU	$\bar{A}_\infty$ [Bq]	$\sigma_{A\infty}$ [Bq]	Φ [n cm $^{-2}$ s^{-1}]	σ_Φ [n cm $^{-2}$ s^{-1}]	E	$\sigma_{reaction}$ [b]
^{116m}In	1	N	281.62	8.47	4.73E+03	0.17E+03	0.025 eV	170
^{56}Mn	1	N	27.48	3.79	2.45E+03	0.34E+03	0.025 eV	13.2
^{56}Mn(Cd)	1	N	24.30	2.30	2.13E+03	0.21E+03	0.025 eV	13.2
^{115m}In	1	N	176.74	8.90	3.02E+07	0.16E+07	>0.5 MeV	0.17
^{116m}In	1	Y	411.06	11.01	6.90E+03	0.11E+03	0.025 eV	170
^{115m}In	1	Y	85.73	4.36	1.46E+07	0.08E+07	>0.5 MeV	0.17
^{116m}In	2	N	150.89	6.51	2.38E+03	0.11E+03	0.025 eV	170
^{56}Mn	2	N	27.20	2.21	2.35E+03	0.19E+03	0.025 eV	13.2
^{56}Mn(Cd)	2	N	24.93	2.20	2.07E+03	0.18E+03	0.025 eV	13.2
^{115m}In	2	N	10.08	0.58	1.62E+06	0.10E+06	>0.5 MeV	0.17
^{116m}In	2	Y	823.15	24.85	1.43E+04	0.05E+04	0.025 eV	170
^{56}Mn	2	Y	267.00	26.01	2.46E+04	0.24E+04	0.025 eV	13.2
^{56}Mn(Cd)	2	Y	271.33	29.35	2.25E+04	0.25E+04	0.025 eV	13.2
^{115m}In	2	Y	4.28	0.34	8.06E+05	0.66E+05	>0.5 MeV	0.17

Table 4.2 Mean saturation activities and neutron flux by product nuclide
Mean saturation activities calculated by for each nuclide, position, and the presence of DU in the system. A rough estimate of the flux required to produce the activity was calculated using the average thermal cross-section or the averaged cross section above the threshold energy.[19]

The thermal flux estimates showed varied levels of agreement depending on location and cavity status. The manganese wires, from both the bare and cadmium covered dysprosium irradiations, produced thermal flux estimates within 1σ of each other under all conditions. However, the ^{116m}In product lines produced a thermal flux estimate ~200% larger than the manganese wires at position 1 in an empty system but only ~60% as large at position 2 in a full system. The cause of this difference was undetermined. Both materials produced an identical thermal flux at position 2 in an empty system. The thermal flux increased with presence of the DU targets at both positions. This was likely due to increased scatter from the target boxes and the minor number of additional neutrons produced by fissions in the system. The ^{115m}In product measured the neutron flux above 0.5 MeV. Higher fast fluxes were observed at position 1 than position 2 and in the empty over the full system. This indicates that there was no significant increase due to fast fissions from the uranium, rather the primary source of high energy neutrons in the system was from the generator itself.

4.2. MCNP Reaction Rate Results

The MCNP simulations were performed to provide two different methods of validation: activation rate calculations and full energy spectra. Reaction rates were calculated using F4 tallies for the aluminum, dysprosium, indium and manganese reactions. The tallies were scaled to the appropriate neutron output for the generator run based on the curve developed in section 3.2.3. Results were listed in Table 4.3 along with the saturation activities calculated from experimental data.

Table 4.3 MCNP reaction rates and saturation activities

Reactiom	Pos.	DU	$MCNP\ RR$ [Bq]	σ_{RR} [Bq]	$\bar{A}_\infty$ [Bq]	$\sigma_{A\infty}$ [Bq]	Ratio $\bar{A}_\infty$:RR	σ_{Ratio}
^{27}Al(n,γ) ^{28}Al	1	N	217	9	-	-	-	
^{27}Al(n,α) ^{24}Na	1	N	0.05	0.00	-	-	-	
^{27}Al(n,p) ^{27}Mg	1	N	0.00	0.00	-	-	-	
^{164}Dy(n,γ) ^{165}Dy	1	N	28.7	1.1	-	-	-	
^{115}In(n,n')^{115m}In	1	N	1.55	0.01	176.74	8.90	114	6
^{55}Mn(n, γ) ^{56}Mn	1	N	73.1	2.4	27.48	3.79	0.376	0.053
^{55}Mn(n, γ) ^{56}Mn(Cd)	1	N	50.7	1.1	24.30	2.30	0.479	0.046
^{27}Al(n,γ) ^{28}Al	2	N	211	11	-	-	-	
^{27}Al(n,α) ^{24}Na	2	N	0.01	0.00	-	-	-	
^{27}Al(n,p) ^{27}Mg	2	N	0.00	0.00	-	-	-	
^{164}Dy(n,γ) ^{165}Dy	2	N	27.5	1.59	-	-	-	
^{115}In(n,n')^{115m}In	2	N	1.45	0.01	10.08	0.58	6.95	0.40
^{55}Mn(n, γ) ^{56}Mn	2	N	68.1	2.86	27.20	2.21	0.399	0.037
^{55}Mn(n, γ) ^{56}Mn(Cd)	2	N	54.5	5.45	24.93	2.20	0.457	0.061
^{27}Al(n,γ) ^{28}Al	1	Y	104	4	-	-	-	
^{27}Al(n,α) ^{24}Na	1	Y	0.17	0.01	-	-	-	
^{27}Al(n,p) ^{27}Mg	1	Y	0.01	0.00	-	-	-	
^{164}Dy(n,γ) ^{165}Dy	1	Y	7.59	0.30	-	-	-	
^{115}In(n,n')^{115m}In	1	Y	14.3	0.04	85.7	4.36	5.99	0.31
^{55}Mn(n, γ) ^{56}Mn	1	Y	38.3	1.28	N.D.	N.D.	-	
^{55}Mn(n, γ) ^{56}Mn(Cd)	1	Y	32.3	0.75	N.D.	N.D.	-	
^{27}Al(n,γ) ^{28}Al	2	Y	349	56	-	-	-	
^{27}Al(n,α) ^{24}Na	2	Y	0.02	0.01	-	-	-	
^{27}Al(n,p) ^{27}Mg	2	Y	0.00	0.00	-	-	-	
^{164}Dy(n,γ) ^{165}Dy	2	Y	48.3	10.6	-	-	-	
^{115}In(n,n')^{115m}In	2	Y	0.69	0.01	4.28	0.34	6.20	0.50
^{55}Mn(n, γ) ^{56}Mn	2	Y	139	14	267.00	26.0	1.92	0.27
^{55}Mn(n, γ) ^{56}Mn(Cd)	2	Y	112	11	271.33	29.35	2.42	0.35

Results for the manganese wires agree within a rounded factor of two. MCNP results overestimate the observed activities for the empty cavity while underestimating the results for a full cavity. The indium results differed by a factor of 6 to 7 except at position 1 in the empty cavity where the MCNP result was 114 times observed. The reason for this large deviation is unclear.

Since no activity from the aluminum and dysprosium reactions was detected, the simulation results could not be directly compared. However, the fast aluminum reactions produced no expected activity in MCNP which would be consistent with the activation levels below the MDA and expectations of a limited fast flux. MCNP appears to have overestimated the thermal aluminum capture rate as simulated reaction rates should have produced a detectable activity level. The low reaction rates for dysprosium were driven by the low atomic density of ^{164}Dy in the alloyed wire, consistent with observed results.

The poor quality of the data precludes more sophisticated analysis. Under ideal circumstances, a larger collection of more massive wires would have been irradiated for a longer time period to obtain higher measurement activities. Increasing wire size would have improved both experimental data and MCNP tally statistics. However, the decommissioning of the system prevented any repeat measurements or acquisition of additional data.

4.3. Unfolded Neutron Energy Spectra

Neutron spectra for the system were unfolded from the available measurements using the SANDII code using the saturation activities in Table 4.2 converted to Bq per target nucleus. Based on recommendations in the software documentation, the solution

criteria was set to a 5 percent difference between successive spectra; calculated and measured activities were required to be within 100 standard deviations to be acceptable. The initial spectra estimate consisted of a large peak flux at 2.45 MeV with a software extrapolated thermal tail. Spectra were computed for both positions and uranium levels and are shown in Figure 4.5. All spectra show near identical structures. Working from high to low energies, there is a large slightly broadened peak at 2.45 MeV which drops to near zero, a rise to a shoulder at 0.5 MeV, and roughly constant epithermal and thermal flux.

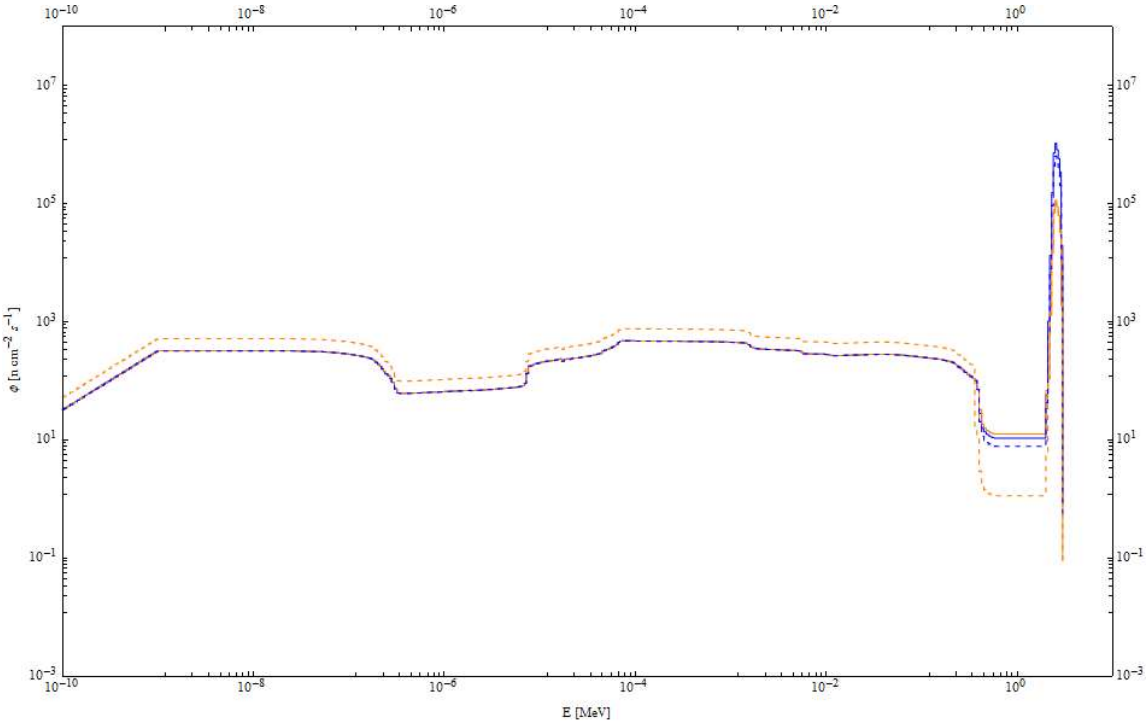

Figure 4.5 SANDII-SNL unfolded neutron spectra. The position 1 wires are shown in blue, position 2 wires are shown in orange, empty cavity lines are dashed, and uranium cavity lines are solid.

These features are due to a combination of two primary factors: the initial spectrum guess and the limited number of reactions available for fitting. The initial spectrum fixed the height of the 2.45 MeV peak, driven by the generator's expected output. The lack of information in the region between 0.5 MeV and 2.45 MeV resulted in slight energy broadening as the code iterated. The ^{115m}In reaction at 0.5 MeV brought the spectrum back up to a baseline level. Any expected scattering behavior was lost because the flux under the 2.45 MeV peak was above the reaction threshold and sufficient to account for the observed activity. Since there was no experimentally determined epithermal ratio due to both the cadmium and thermal dysprosium reactions falling below the MDA, the rest of the spectra was relatively flat with small bumps driven by cross section features until the thermal tail extrapolation began to dominate. Under ideal circumstances, a larger collection of more massive wires would have been irradiated for a longer time period to obtain more useful reactions. However, the operational constraints and decision to decommission the system precluded this option.

Neutron flux spectra were also calculated using MCNP. F4 tallies were used to compute the flux spectra through the activation wire cell using the 621 energy group structure of SAND II. Flux spectra are included in Figures 4.6 to 4.7. Spectra at position 1 are blue while position 2 are orange; the empty and full cavities are dashed and solid lines respectively. Figure 4.8 combines all MCNP spectra on one plot.

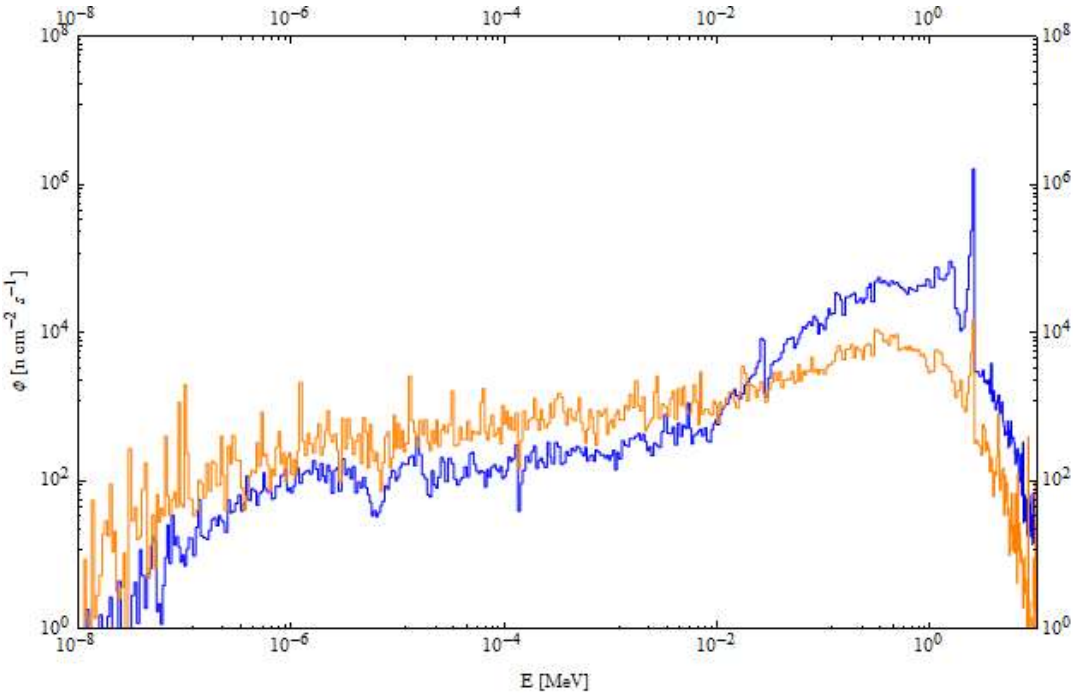

Figure 4.6 MCNP neutron flux spectra for system with DU target boxes. Position 1 is plotted in blue. Position 2 is plotted in orange.

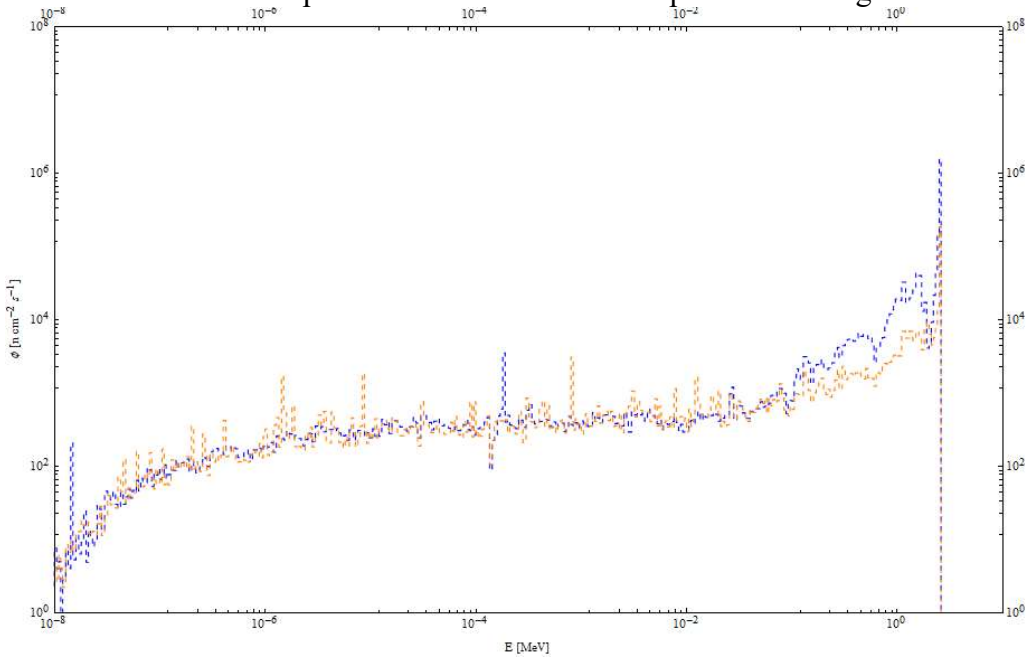

Figure 4.7 MCNP neutron flux spectra for empty cavity system. Position 1 is plotted in blue. Position 2 is plotted in orange.

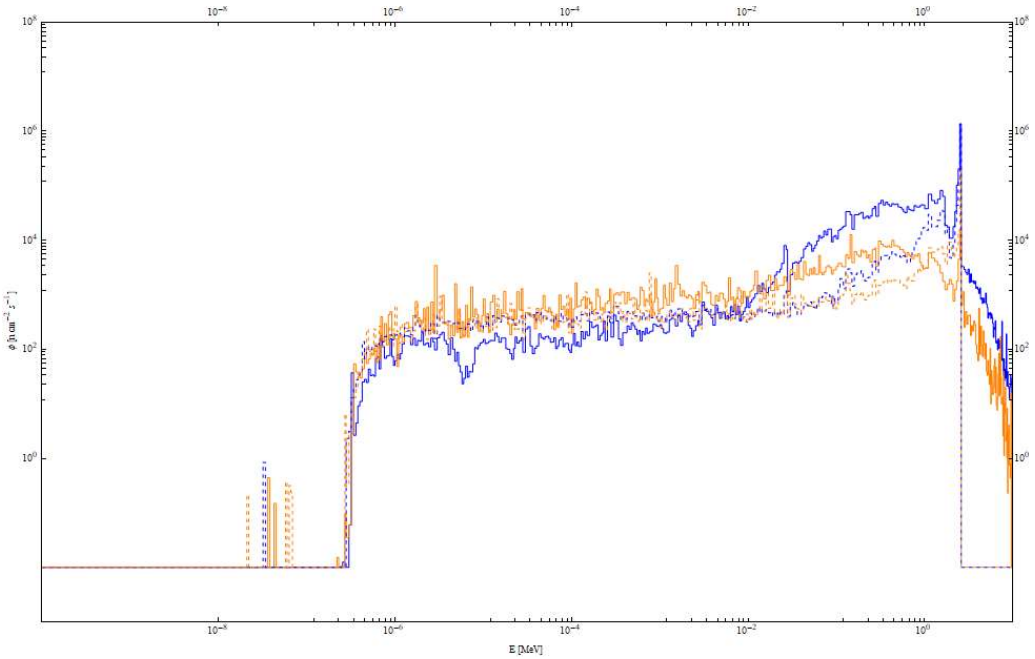

Figure 4.8 Combined MCNP neutron flux spectra for empty (dashed) and full (solid) cavity. Position 1 is plotted in blue. Position 2 is plotted in orange.

Simulation results should be considered with caution. Despite heavy application of variance reduction methods, MCNP had difficulty sufficiently sampling to achieve 10% relative error for all bins. Due to the large number of energy bins and small tally region, several bins recorded no hits particularly at lower energies. This was exaggerated in the cases without the target boxes as the neutrons had fewer opportunities to scatter and were more likely to exit the problem without passing through the tally region. Empty tally bins were set to 0.01 to enable smooth logarithmic plotting of the data.

The MCNP spectra all show consistent features. A large spike is observed from the source neutrons at 2.45 MeV. This is larger at position 1 and in the empty cavity due to the proximity of the source and reduced chances for scatter. A minor fast flux is apparent in the uranium-filled cavities above the 2.45 MeV threshold due to additional

fission neutrons. This not present in the empty cavity. Both cavities configurations show a reduction in flux as neutrons scatter down to 10^{-2} MeV to a relatively stable low level before dying out at low energies. This behavior matches general expectations. The system design offered few opportunities for neutrons to thermalize in the cavity. The majority of the hydrogenous material was located in the shielding walls. Thermalized neutrons would be more likely to escape or be captured by the boron in the shielding than scatter back to the low target volume in the cavity.

MCNP and SANDII spectra are plotted together in Figures 4.9 to 4.12 to enable direct comparisons. Qualitatively, the key features of each are comparable. There is a slight mismatch between 2.45 MeV peaks. The MCNP peaks are taller but thinner, spikes caused by the uncollided neutron flux of the system. The SANDII peaks are shorter in height but broaden in both directions, likely an artifact of the code iterating to a solution flux by testing adjacent energy bins. The SANDII spectra lack the slowing down slope between 2.45 MeV and 0.5 MeV that is visible in the MCNP spectra. In the epithermal to thermal range, the spectra are roughly comparable. At extremely low energies the SANDII spectra remain roughly consistent driven by their extrapolated thermal tail while the MCNP spectra dies off. Integrated fluxes above and below the 0.5 MeV In threshold are tabulated in Table 4.4.

Position	DU	E_{Range} [MeV]	MCNP Flux [n cm $^{-2}$ s^{-1}]	%	SANDII Flux [n cm $^{-2}$ s^{-1}]	%	$\frac{MCNP}{SANDII}$
1	N	Full	2.392E+06	1.00	2.366E+06	1.00	1.01
1	Y	Full	4.574E+06	1.00	3.852E+06	1.00	1.19
2	N	Full	4.801E+05	1.00	5.415E+05	1.00	0.89
2	Y	Full	5.810E+05	1.00	2.681E+05	1.00	2.17
1	N	<0.5	2.191E+05	0.05	1.130E+05	0.09	1.94
1	Y	<0.5	1.414E+06	0.03	1.129E+05	0.31	12.52
2	N	<0.5	1.595E+05	0.33	1.809E+05	0.33	0.88
2	Y	<0.5	4.450E+05	0.42	1.229E+05	0.77	3.62
1	N	>0.5	2.179E+06	0.95	2.253E+06	0.91	0.97
1	Y	>0.5	3.202E+06	0.97	3.739E+06	0.70	0.86
2	N	>0.5	3.222E+05	0.67	3.605E+05	0.67	0.89
2	Y	>0.5	1.422E+05	0.58	1.551E+05	0.24	0.92

Table 4.4 Integral MCNP and SANDII Fluxes

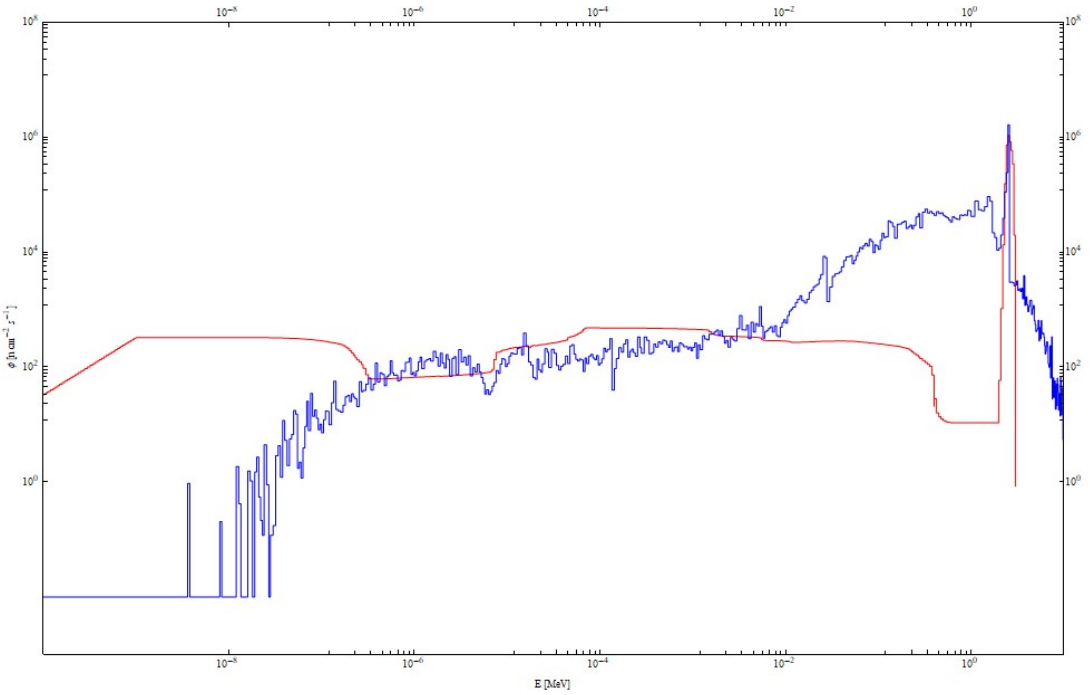

Figure 4.9 MCNP and SANDII neutron flux spectra for full cavity at position 1.MCNP is in blue; SANDII is in red.

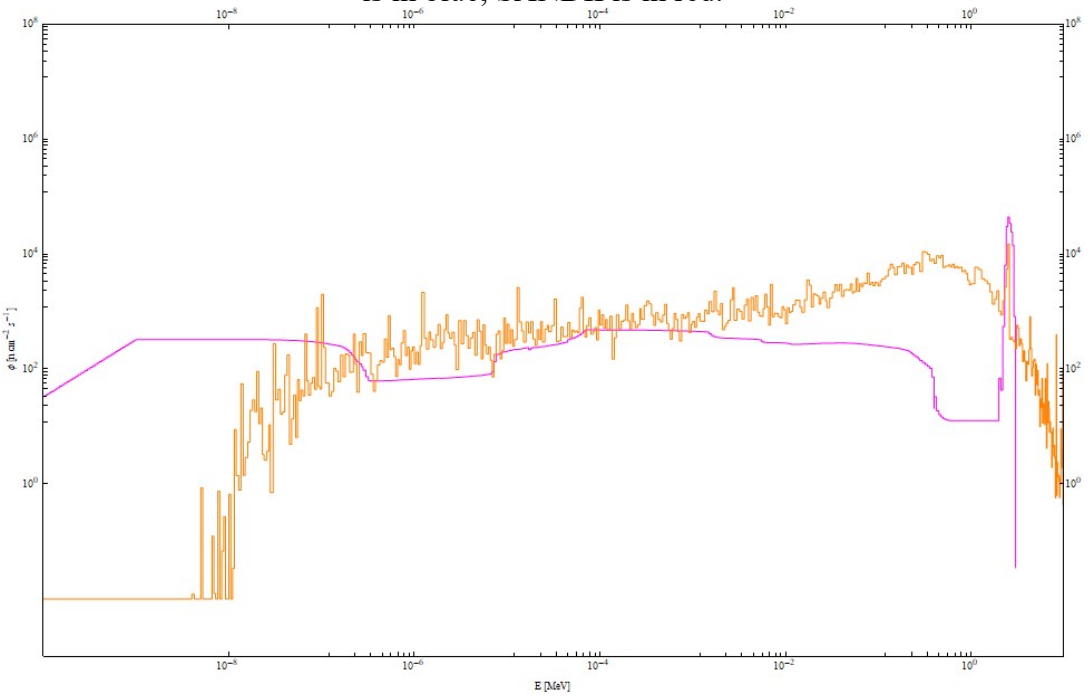

Figure 4.10 MCNP and SANDII neutron flux spectra for full cavity at position 2. MCNP is in orange, SANDII is in magenta.

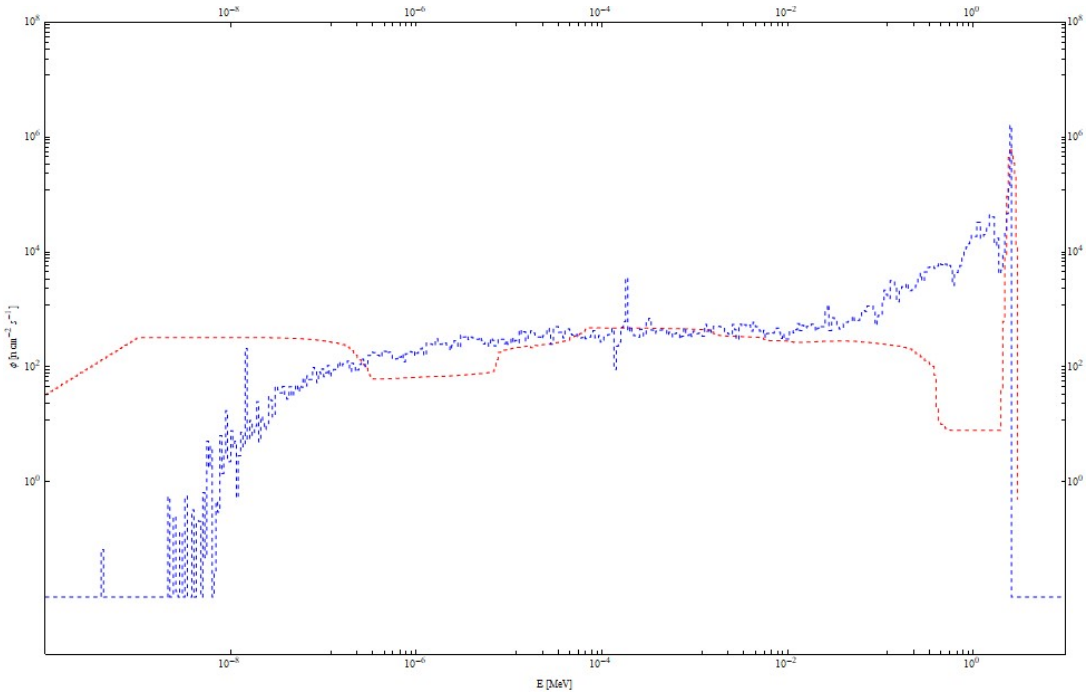

Figure 4.11 MCNP and SANDII neutron flux spectra for empty cavity at position 1. MCNP is in blue; SANDII is in Red.

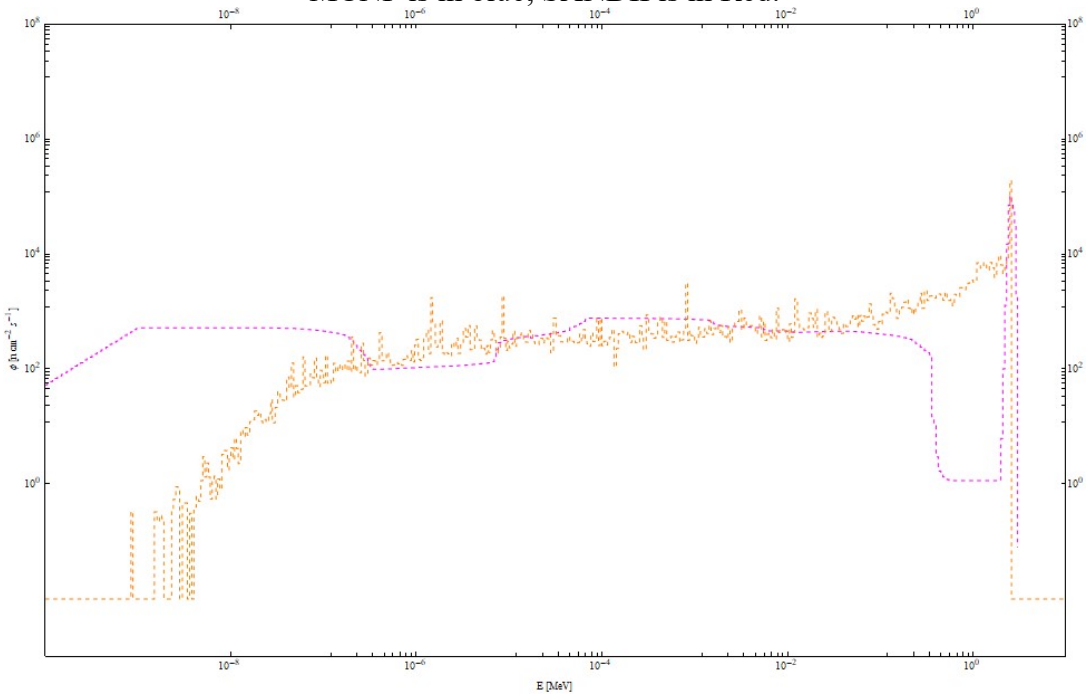

Figure 4.12 MCNP and SANDII neutron flux spectra for empty cavity at position 2. MCNP is in orange; SAND II is in magenta.

The integrated SANDII and MCNP fluxes showed strong agreement driven by the 2.45 MeV peak from the generator neutrons. Three of the total fluxes agreed within 20 % while the fourth agreed within a factor of 2.2. If the flux is divided into regions above and below 0.5 MeV, the majority of the total flux occurs in the higher region, ~95% at position 1 and ~60% at position 2 for both empty and full cavity. This behavior was expected. At position 1, the majority of the neutron flux is driven by the mono-energetic flux from the generator. Any lower energy component would come from scatter and thermalization in the other elements of the systems. At position 2, the generator's flux component would be reduced in both absolute and relative importance due to geometric attenuation and scattering from the hydrogenous shield walls. The high energy fluxes all agree within 15%. The deviation between the SAND and MCNP fluxes is primarily driven by differences in thermal and epithermal fluxes.

Under ideal circumstances, results could be significantly improved by the addition of more foil data. The addition of a threshold detector between 0.5 MeV and 2.45 MeV would help produce a more realistic estimate of the high energy flux as neutrons slow from the D-D peak. Additional thermal and epithermal data would reduce the cross-section-driven structures in the SANDII estimate of those regions. Additionally, the initial flux estimate could be modified to start closer to the MCNP result. However, without any constraints from any additional foil data almost any initial estimate will suffice as a solution. Unfortunately, the limited supply of available wire materials and the sudden and unplanned decommissioning of the system prevented acquisition of any additional data.

4.4. Source Efficiency, System Power, and ^{99}Mo production

The primary purpose of the MCNP model was to provide estimates of the ^{99}Mo production in the driven sub-critical system. By coupling the outputs of a fixed source and criticality mode calculation, φ^*, the efficiency of the source neutrons for causing fissions, was determined. MCNP estimates for k_{eff}, total fissions per source neutron, and total fission produced neutrons per source neutron are listed in Table 4.5 along with calculated values for φ^*, k_s, and system power. It is convenient to also list the number of fissions and fission neutrons that produced only in the target boxes with the reflectors in place to enable a direct comparison.

System Parameter	Boxes (No Reflectors)	Total System (Reflectors)	Boxes (Reflectors)
k_{eff}	0.18007±0.00058	0.24388±0.00085	-
Fissions	0.09248±0.00011	0.12786±0.00018	0.09396±0.00011
Fission Neutrons	0.24672±0.00030	0.34102±0.00048	0.25100±0.00033
φ^*	1.12343±0.00077	1.05730±0.00122	-
k_s	0.19790±0.00063	0.25430±0.00090	-
System Power [mW]	7.08±0.03	9.78±0.05	

Table 4.5 MCNP estimates and derived system parameters
MCNP estimates and derived values for k_{eff}, total fissions per source neutron, total fissions neutrons per source neutron, φ^*, k_s, and system power. Listed errors are propagated solely from MCNP statistical errors. The system power was calculated assuming a source strength of 2.43×10^9 n s^{-1} corresponding to a generator beam power of 1,600 W. In practice, source strength errors due to fluctuations in voltage and beam current would dominate.

The qualitative behavior of the results matches general expectations. The k_{eff} estimate for only the target boxes is lower than that with reflectors since a greater fraction of its fissionable material is comparatively more dispersed. The presence of reflectors does not considerably increase the number of a fissions that occur in the

targets providing only a ~2% increase. Instead, the majority of the additional fissions occur in the reflectors. Both configurations are deeply sub-critical since only DU is present. In both cases, the source efficiency is greater than 1 indicating that source neutrons from the generator are slightly more efficient at causing fission than subsequent fission neutrons. As a result, k_s is significantly greater than k_{eff}, by roughly 15σ for only the target boxes and 6σ with reflectors present. Listed errors are propagated solely from MCNP statistical errors. The importance of the source neutrons is reduced by the presence of the reflectors as the addition of large, dense amounts of fissionable material increases the probability for subsequent fissions.

However, the total number of fissions is still low. Assuming a source strength of 2.43×10^9 n s^{-1}, the system power is only in the milliwatt range which is insufficient to generate appreciable amounts of ^{99}Mo. ^{99}Mo is a fission product with a cumulative yield of 6.181 ± 0.099 % from fast fission in ^{238}U. [30] Total extractable system production can be estimated directly from fission rate for the target boxes over a given irradiation period. Total production estimates for both configurations as a function of time are plotted in Figure 4.13. There is minimal difference between the production curves since the reflectors provide only a minor increase to the fission rate in the targets. At 7 days, there is 11.70±0.02 MBq with reflectors compared to 11.51±0.01 MBq without reflectors. However, this represents the total activity present in the targets. Only a tiny fraction <1% of this amount is extracted by the GMIS procedures. Additionally, ^{99}Tc exists in transient equilibrium with its parent ^{99}Mo and is limited to a saturation activity of ~95% of the ^{99}Mo activity. The average ^{99}Tc imaging dose amount varies by patient

and location. For a 70 kg adult, suggested recommended ^{99}Tc doses range from 370 - 740 MBq for brain imaging or 37-370 MBq for thyroid gland imaging.[31] The entire 7 day output of GMIS system would be insufficient to generate a single dose for either of these procedures. This indicates that the system is not a viable method for ^{99}Mo production as currently designed.

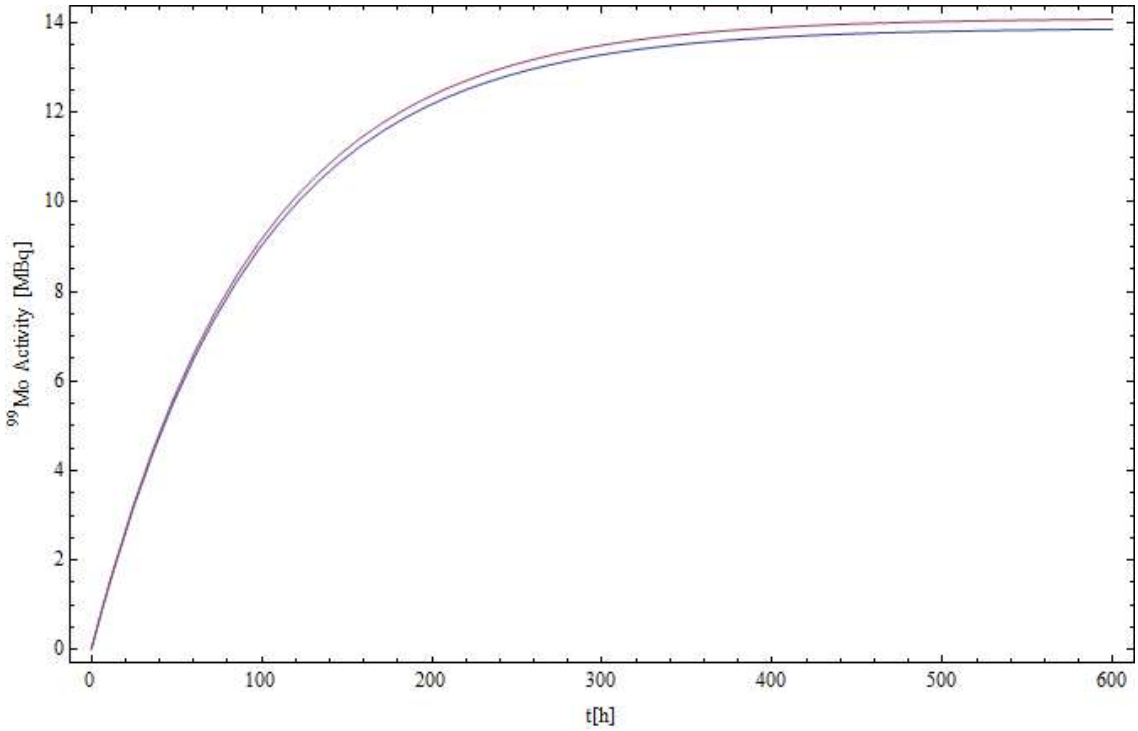

Figure 4.13 Estimated system ^{99}Mo production as a function of time without reflectors in blue, with reflectors in magenta.

.

Based on this result and GMIS's decision to decommission the prototype system, further model validation would be of limited value. Instead, any future work should

return to the system design stage, focus on methods of improving neutron generator yields, or develop viable alternative production methods.

The current fatal flaw of the system is that the fission rate is too low. This problem could be solved by redesigning the system to an appropriate power level required to produce a given amount of ^{99}Mo. If the weekly end-of-process target value is 250 TBq, with a 1% efficient 7-day cycle (6 for production, 1 for extraction) is assumed, then a roughly 20 MW facility would be required. For a 10^{10} n s^{-1} neutron generator, this would require a k_s of ~0.9999995. If the generator strength is increased to 10^{15} n $^{s-1}$, the required k_s is reduced to ~0.95. Any future sub-critical assembly should be designed to reach the appropriate value of k_s, likely requiring the use of NU or LEU.

Alternative research could focus on improving the yield of the neutron generator. The generator involved in this work used a single DD beam on a titanium target. Higher yield generators are already available. Significantly higher fluxes can be reached using a DT gas mixture, although this complicates handling due to environmental concerns. Higher fluxes may also be obtainable by using multiple beam lines on a spherical target. However, this would change the footprint of the system which must be considered in the system design stage. Additionally, alternative generator target materials could be studied. Scandium has higher hydrogen retention rates at high temperatures and may provide a better target material.

Finally, alternative system materials and driving neutron sources could be examined. An aqueous uranium solution would offer inherent advantages for chemical extraction but complicate material handling. It would also necessitate the use of LEU to

reach higher values of k_s. Alternatively, different neutron sources, such as photo-neutron production or photo-fission, can reach the required source strength if driven by sufficiently powerful linear accelerator. These alternatives sources might be more viable than fusion neutron generators with sufficient yield. However, these approaches would require significant changes at the system design level.

5. CONCLUSIONS

Multiple companies have attempted to develop alternatives to reactors for producing ^{99}Mo including driven sub-critical systems. The chief objective of this work was to develop and validate a model of the GMIS prototype system which used a DD neutron generator to drive a DU subcritical assembly for radioisotope production. The model was created using MCNP6.1 and validated by comparison to experimentally collected values.

The GMIS system was described in detail. A review of the underlying principles behind neutron generators and sub-critical multiplication in external-source-driven systems was provided. Summaries of the Monte Carlo methods, foil activation theory, and neutron spectra unfolding code used to construct and validate the model were provided.

An initial MCNP model was constructed to replicate lithium irradiations for tritium production performed by GMIS in 2016. A six order of magnitude difference was observed between GMIS reported results and MCNP predicted results. Exterior dose measurements were performed to provide initial validation. MCNP model and empirical dose measurements showed rough agreement: three of five measurements agreed within 1σ error, the other two agreed within a factor of 2.

Further validation work was performed using activation wires. The planned series of activation wire measurements was cut short by equipment failure and only minimal data was obtained for validation. The prototype system was decommissioned

during the course of this research and further data was unattainable. No activity was detected in aluminum, dysprosium aluminum, and cobalt wires. Activity was observed in indium and manganese wires. Directly calculated MCNP reaction rates differed from measured saturation activities in all cases; by a rough factor of 2 for manganese wires and a rough factor of 6 for indium wires. Unfolded neutron spectra showed rough agreement with MCNP estimated neutron spectra. Integral fluxes agreed within 20% for three of four cases and the fourth differed by a rough factor of 2. The disagreement between integral fluxes was driven by differences in the thermal and epithermal flux. The MCNP model should be utilized with caution given the consistent difference of a factor of 2 between empirical and simulated results.

The MCNP model was used to estimate the source efficiency, sub-critical multiplication factor, and system power of the prototype system in its standard configuration. A subcritical multiplication factor was found to be 0.25430 ± 0.00090 corresponding to a system power of 9.78 ± 0.05 mW at standard operating parameters; errors are solely derived from MCNP statistical error. This corresponds to a total 7 day ^{99}Mo activity production of 11.70 ± 0.02 MBq. This is insufficient to meet any commercial demand.

Based on the results of this study, the current design of the GMIS prototype system is deemed not useful for isotope production. However, the physics of driven sub-critical assemblies are well understood. Neutron generators continue to advance in both reliability and yield. A redesigned system based on a proper understanding of the underlying physics utilizing fissile material may provide a viable alternative.

REFERENCES

[1] Radioisotopes in Medicine | Nuclear Medicine - World Nuclear Association, (n.d.). http://www.world-nuclear.org/information-library/non-power-nuclear-applications/radioisotopes-research/radioisotopes-in-medicine.aspx (accessed January 18, 2019).

[2] A.J. Youker, S.D. Chemerisov, P. Tkac, M. Kalensky, T.A. Heltemes, D.A. Rotsch, G.F. Vandegrift, J.F. Krebs, V. Makarashvili, D.C. Stepinski, Fission-Produced 99Mo Without a Nuclear Reactor, J. Nucl. Med. 58 (2017) 514–517. https://doi.org/10.2967/jnumed.116.181040.

[3] National Academies of Sciences Engineering, Medicine, Molybdenum-99 for Medical Imaging, The National Academies Press, Washington, DC, 2016. https://doi.org/10.17226/23563.

[4] NNSA's Molybdenum-99 Program: Establishing a Reliable Supply of Mo-99 Produced Without Highly Enriched Uranium | Department of Energy, (n.d.). https://www.energy.gov/nnsa/nnsa-s-molybdenum-99-program-establishing-reliable-supply-mo-99-produced (accessed January 18, 2019).

[5] J.T. Goorley, M.R. James, T.E. Booth, F.B. Brown, J.S. Bull, L.J. Cox, J.W. Durkee, J.S. Elson, G.W. McKinney, D.B. Pelowitz, R.E. Prael, J.E. Sweezy, L.S. Waters, T.A. Wilcox, A. Zukaitis, MCNP Users Manual - Code Version 6.1, (2013) 765.

[6] Adelphi Technology Inc., DD110 Operation Manual, Redwood City, CA, n.d. Retrieved from Global Medical Isotopes Systems Intranet (accessed June 30, 2018)

[7] T.P. Lou, Compact D-D/D-T Neutron Generators and Their Applications, University of California, Berkeley, 2003.

[8] J.M. Verbeke, K.N. Leung, J. Vujic, Development of a sealed-accelerator-tube neutron generator, Appl. Radiat. Isot. 53 (2000) 801–809. https://doi.org/10.1016/S0969-8043(00)00262-1.

[9] D.A. Brown, M.B. Chadwick, R. Capote, A.C. Kahler, A. Trkov, M.W. Herman, A.A. Sonzogni, Y. Danon, A.D. Carlson, M. Dunn, D.L. Smith, G.M. Hale, G. Arbanas, R. Arcilla, C.R. Bates, B. Beck, B. Becker, F. Brown, R.J. Casperson, J. Conlin, D.E. Cullen, M.-A. Descalle, R. Firestone, T. Gaines, K.H. Guber, A.I. Hawari, J. Holmes, T.D. Johnson, T. Kawano, B.C. Kiedrowski, A.J. Koning, S. Kopecky, L. Leal, J.P. Lestone, C. Lubitz, J.I. Márquez Damián, C.M. Mattoon, E.A. McCutchan, S. Mughabghab, P. Navratil, D. Neudecker, G.P.A. Nobre, G. Noguere, M. Paris, M.T. Pigni, A.J. Plompen, B. Pritychenko, V.G. Pronyaev, D. Roubtsov, D. Rochman, P. Romano, P. Schillebeeckx, S. Simakov, M. Sin, I. Sirakov, B. Sleaford, V. Sobes, E.S. Soukhovitskii, I. Stetcu, P. Talou, I. Thompson, S. van der Marck, L. Welser-Sherrill, D. Wiarda, M. White, J.L. Wormald, R.Q. Wright, M. Zerkle, G. Žerovnik, Y. Zhu, ENDF/B-VIII.0: The 8th Major Release of the Nuclear Reaction Data Library with CIELO-project Cross Sections, New Standards and Thermal Scattering Data, Nucl. Data Sheets. 148 (2018) 1–142. https://doi.org/10.1016/j.nds.2018.02.001.

[10] Francis Tsang, Mo-99 at EOP, (2016). Retrieved Global Medical Isotopes Systems Intranet (accessed June 30, 2018).
[11] U.S. Government Accountablity Office, GAO-18-126, U.S. Government Printing Office, Washington, DC, 2018. https://www.gao.gov/assets/700/690143.pdf (accessed February 6, 2020).
[12] Francis Tsang, Failure of 4th Irradiation, (2016). Retrieved Global Medical Isotopes Systems Intranet (accessed June 30, 2018).
[13] Francis Tsang, Tritium production from natural lithium metal, (2017). Retrieved Global Medical Isotopes Systems Intranet (accessed June 30, 2018).
[14] J.R. Lamarsh, A.J. Baratta, Introduction to nuclear engineering, 3rd ed., Prentice Hall, Upper Saddle River, N.J., 2001.
[15] H.R. Vega-Carrillo, I.R. Esparza-Garcia, A. Sanchez, Features of a subcritical nuclear reactor, Ann. Nucl. Energy. 75 (2015) 101–106. https://doi.org/10.1016/j.anucene.2014.08.006.
[16] P.W. Mendius, I. Harmon C.D., R.D. Busch, J.F. Briesmeister, R.A. Forster, Criticality calculations with MCNP{sup TM}: A primer, United States, 1994. https://doi.org/10.2172/10171566.
[17] Los Alamos National Laboratory: MCNP Home Page, (n.d.). https://mcnp.lanl.gov/ (accessed January 18, 2019).
[18] X-5 Monte Carlo Team, i, MCNP - Version 5, Vol. I: Overview and Theory, 2003.
[19] G.F. Knoll, Radiation detection and measurement, 4th ed., John Wiley, Hoboken, N.J., 2010. http://catalogimages.wiley.com/images/db/jimages/9780470131480.jpg.
[20] P.J. Griffin, J. G. Kelly, J. W. VanDenburg, User`s manual for SNL-SAND-II code, (2019). https://doi.org/10.2172/10149711.
[21] W.N. McElroy, S. Berg, T. Crockett, R.G. Hawkins, A Computer-Automated Iterative Method for Neutron Flux Spectra Determination by Foil Activation, Vol. I: A Study of the Iterative Method, 1967.
[22] Ludlum Measurements, Inc., Model 2241 General Purpose Ratemeter / Scaler, (2013). https://ludlums.com/images/data_sheets/M2241.pdf (accessed June 12, 2020).
[23] Ludlum Measurements, Inc., M42-31H 9-Inch Moderated Neutron Detector, (2017). https://ludlums.com/images/data_sheets/M42-31H.pdf (accessed June 12, 2020).
[24] Chang, J., Table of Nuclides, KAERI Korea At. Energy Res. Inst. (n.d.). http://atom.kaeri.re.kr/ton (accessed June 12, 2020).
[25] Activation Foils, (n.d.). http://www.shieldwerx.com/activation-foils.html (accessed June 12, 2020).
[26] GammaVision Gamma Spectroscopy, ORTEC, n.d. https://www.ortec-online.com/products/application-software/gammavision.
[27] W. Johnson, InterSpec, n.d. https://github.com/sandialabs/InterSpec.
[28] Mirion Technologies, Spectrum Analysis, (2017). https://www.mirion.com/learning-center/nuclear-measurement-fundamental-principles/nuclear-measurement-fundamental-principle-spectrum-analysis (accessed June 12, 2020).

[29] J.F. Ziegler, J.P. Biersack, The Stopping and Range of Ions in Matter, in: D.A. Bromley (Ed.), Treatise Heavy-Ion Sci. Vol. 6 Astrophys. Chem. Condens. Matter, Springer US, Boston, MA, 1985: pp. 93–129. https://doi.org/10.1007/978-1-4615-8103-1_3.
[30] A. Nichols, E. McCutchan, P. Dimitriou, INDC International Nuclear Data Committee, 2017. https://doi.org/10.2172/1413963.
[31] Lantheus, Technelite Tc 99m yield chart sunday, (n.d.). https://www.lantheus.com/assets/technelite-tc99m-yield-chart-sunday.pdf.

APPENDIX A

SAMPLE MCNP CODE

A sample of the initial annotated MCNP code used for the lithium irradiation showing material compositions and source definition. Full cell and surface definitions are omitted due length.

```
c GMIS Lithium Production Model v0.0.01
c
c This deck models the GMIS Isotope production system. The system
consists of a
c neutron generator surrounded by 4 boxes of target material filled
with sheets
c of parent material. These boxes are surrounded by a Depleted Uranium
(DU)
c reflector. There is additional piping supporting structure that
c will be added as the model progresses. The current structure of the
deck is
c that cells 1000-4000 are
c used to model the 4 target boxes. Cells 5000 are used to model the
generator
c Cells 6000 are used for various air gaps within the system. Cells
7000 will
c be used for supporting structures. Cells 8000 are used for the DU
reflector.
c Cells 9000 are used for the exterior shielding.
c
c The 4 boxes (1-4) are ordered  around the generator (G) as shown
below.
c Physically the -y is into the office building
c
c   +y       233
c -x 0 +x  2S4
c   -y        114
c
c
c Cells 1000 model box 1. Cells in 10xx model the containing box
c (top, sides, and base), the air gaps above and below the sheets
c within the box. Cells above 1100 model the sheets and interior
spacing.
c Box 1 contains 50 sheets each 30 mil (.0762 cm) thick. These are
assumed
c to be evenly spaced throughout
c
 1000     7   -7.99 6000 -6001 6011 -6014 6015 -6018  imp:n=1$Base of
steel box 1
 1001     7   -7.99 6004 -6005 6011 -6014 6015 -6018  imp:n=1$top of
steel box 1
 1002     7   -7.99 6001 -6004 6011 -6012 6015 -6018  imp:n=1$-x of
steel box 1
```

```
 1003     7   -7.99 6001 -6004 6012 -6013 6015 -6016  imp:n=1$-y of
steel box 1
 1004     7   -7.99 6001 -6004 6013 -6014 6015 -6018  imp:n=1$+x of
steel box 1
 1005     7   -7.99 6001 -6004 6012 -6013 6017 -6018  imp:n=1$+y of
steel box 1
c air gaps
 1006     1 -0.001155 6001 -6002 6012 -6013 6016 -6017  imp:n=1$air gap
below sheet
 1007     1 -0.001155 6003 -6004 6012 -6013 6016 -6017  imp:n=1$air gap
above sheet
c
c cells 1100+ are reserved for the sheets. There are 50 sheets
c spaced evenly thoughout the 14.355 cm interior. This results in
c a spacing of ~0.2068 between walls and sheets (rounding difference
c taken from  furthest air gap from source.
c
 1100     1 -0.001155 6002 -6003 6012 -6013 6016 -1000  imp:n=1$ first
air gap
 1101     2 -18.95116 6002 -6003 6012 -6013 1000 -1001  imp:n=1$ sheet
1
 1102     1 -0.001155 6002 -6003 6012 -6013 1001 -1002  imp:n=1$
 1103     2 -18.95116 6002 -6003 6012 -6013 1002 -1003  imp:n=1$ sheet
2
 1104     1 -0.001155 6002 -6003 6012 -6013 1003 -1004  imp:n=1$
 1105     2 -18.95116 6002 -6003 6012 -6013 1004 -1005  imp:n=1$3
 1106     1 -0.001155 6002 -6003 6012 -6013 1005 -1006  imp:n=1$
[…]
c
c
c
c cells 2000 describe box 2. or the removed space of box 2 and the
contained
c experiment. The current uncommented cells describe the initial full
poly
c block run with a lithium foil on axis with the source
c and a second lithium foil located half way into the remaining poly.
c The alternative configurations are
c listed in commented out sections.
c
c cells 20xx define the major features in each case; the poly block or
c air void and the simpler features c of the bottles
c
 2000     4   -0.95 6000 -2001 6021 -6023 6025 -6028  imp:n=1$ poly
beneath bottles
 2001     4   -0.95 2001 -2005 6021 -6023 6025 -6028 2011 2021 2031
2041 imp:n=1$poly around
 2002     4   -0.95 2005 -6005 6021 -6023 6025 -6028  imp:n=1$ poly
above bottles
c
 2010     1 -0.001155 2001 -2005 -2011 2012  imp:n=1$air between glass
& bottle
```

```
 2011     1 -0.001155 2004 -2005 -2012 2014  imp:n=1$air between glass
& bottle top
 2012     8   -2.23 2001 -2002 -2012  imp:n=1$glass bottle base
 2013     8   -2.23 2002 -2004 -2012 2013  imp:n=1$glass side wall
 2014     8   -2.23 2004 -2005 -2014 2015  imp:n=1$glass top side wall
 2015     6 -0.001329 2004 -2005 -2015  imp:n=1$ argon filling the cap,
no plastic
 2016     6 -0.001329 2003 -2004 -2013  imp:n=1$ argon above the foil
c
 2100     6 -0.001329 2002 -2003 -2100  imp:n=1$ argon in center
 2101     5  -0.535 2002 -2003 2100 -2101  imp:n=1$  0
 2102     6 -0.001329 2002 -2003 2101 -2102  imp:n=1$
 2103     5  -0.535 2002 -2003 2102 -2103  imp:n=1$  1
 2104     6 -0.001329 2002 -2003 2103 -2104  imp:n=1$
 2105     5  -0.535 2002 -2003 2104 -2105  imp:n=1$  2
 2106     6 -0.001329 2002 -2003 2105 -2106  imp:n=1$
 [..]


c This block of cells refers to a full poly run. The glass bottles are
c assumed to be perfect cylinders c w/ an argon atmosphere. The box
c consists of a full block of Poly with a hole drilled for the bottle.
c the bottle sits so that the lithium foil is
c Cells 3000 model box 3. Cells in 30xx model the containing box
c (top, sides, and base), the air gaps above and below the sheets
within
c the box. Cells above 3100 model the sheets and interior spacing. Box
c 3 contains 101 sheets 30 mil (.0762 cm) thick. These are assumed to
c be evenly spaced throughout
c
 3000     7   -7.99 6000 -6001 6031 -6034 6035 -6038  imp:n=1$ Base
steel box 3
 3001     7   -7.99 6004 -6005 6031 -6034 6035 -6038  imp:n=1$ top
steel box 3
 3002     7   -7.99 6001 -6004 6031 -6032 6035 -6038  imp:n=1$ -x steel
box 3
 3003     7   -7.99 6001 -6004 6032 -6033 6035 -6036  imp:n=1$ -y steel
box 3
 3004     7   -7.99 6001 -6004 6033 -6034 6035 -6038  imp:n=1$ +x steel
box 3
 3005     7   -7.99 6001 -6004 6032 -6033 6037 -6038  imp:n=1$ +y steel
box 3
c air gaps
 3006     1 -0.001155 6001 -6002 6032 -6033 6036 -6037  imp:n=1$ air
below sheets
 3007     1 -0.001155 6003 -6004 6032 -6033 6036 -6037  imp:n=1$ air
above sheets
c
c cells 3100+ are reserved for the sheets. There are 79 sheets spaced
c evenly thoughout the 14.355 cm  interior. This results a spacing of
c ~0.1042 between walls and sheets (rounding difference taken from
c furthest air gap from source.
c
```

```
c
 3100     1 -0.001155 6002 -6003 6032 -6033 3000 -6037 imp:n=1$
 3101     2 -18.95116 6002 -6003 6032 -6033 3001 -3000  imp:n=1$1
 3102     1 -0.001155 6002 -6003 6032 -6033 3002 -3001 imp:n=1$
 3103     2 -18.95116 6002 -6003 6032 -6033 3003 -3002  imp:n=1$2
 3104     1 -0.001155 6002 -6003 6032 -6033 3004 -3003 imp:n=1$
 3105     2 -18.95116 6002 -6003 6032 -6033 3005 -3004  imp:n=1$3
 3106     1 -0.001155 6002 -6003 6032 -6033 3006 -3005 imp:n=1$
 […]

c Cells 4000 model box 4. Currently empty to represent the fast zone
c normally would contain box 4
c Cells in 40xx model the containing box
c (top, sides, and base), the air gaps
c above and below the sheets within the box. Cells above 4100 model
c the sheets and interior spacing.  Box 4 contains 79 sheets 30 mil
c (.0762 cm) thick. These are assumed to be evenly spaced throughout
c
 4000      1 -0.001155 6000 -6005 6041 -6044 6045 -6047  imp:n=1$ Base
steel box 4
c
c
c
c cells 5000 describe the neutron generator and associated structures
c cells 5001 describe the D-D plasma region (SOURCE), cells 5002/5003
c describe the Cu target
c
 5001    10 -4.407e-010 5009 -5002 5003 -5004 5006 5007  imp:n=1$DD in
wedge
 5002     9  -8.945 5009 -5002 5003 -5004 5005 -5006  imp:n=1$LT target
Wedge
 5003     9  -8.945 5009 -5002 5003 -5004 -5007 5008  imp:n=1$RT Target
Wedge
 5004    11    -2.7 5013 -5014 -5012  imp:n=1$aluminum window
 5005    11    -2.7 5010 -5013 5011 -5012  imp:n=1$Aluminum shroud
 5006    10 -4.407e-010 5001 -5002 -5011 -5005 5003 -5004  imp:n=1$D
fill left wedge
 5007    10 -4.407e-010 5001 -5002 -5011 -5008 5003 -5004  imp:n=1$D
Fill Rt wedge
 5008    10 -4.407e-010 5002 -5013 -5011  imp:n=1$D fill bove wedgec
 5009    10 -4.407e-010 5001 -5002 -5011 -5003 imp:n=1$
 5010    10 -4.407e-010 5001 -5002 -5011 5004 imp:n=1$
 5011     9  -8.945 5010 -5001 -5011  imp:n=1$CU beneath wedge
 5012     9  -8.945 5001 -5009 5008 5005 5003 -5004 imp:n=1$
c
c cells 5100 describe the steel cylinder containing D-D generator and D
fuel
 5100     7   -7.99 5015 -5017 5019 -5020  imp:n=1$steel walls
 5101     7   -7.99 5017 -5018 -5020  imp:n=1$steel top
 5102     7   -7.99 5016 -5015 -5020  imp:n=1$steel bottom
 5103    10 -4.407e-010 5015 -5010 -5019  imp:n=1$d fill below al
 5104    10 -4.407e-010 5010 -5014 -5019 5012  imp:n=1$d fill around al
 5105    10 -4.407e-010 5014 -5017 -5019  imp:n=1$d fill above al
```

```
c
c
c cells 6000 are used for various air groups in the system. Between the
c steel cylinder and the boxes, the gaps in between the plate boxes,
c the gaps between the boxes and DU, and the DU and the walls
c
 6001     1 -0.001155 6000 -6005 6023 -6041 6018 -6035 5020
imp:n=1$air around
 6002     1 -0.001155 6000 -6005 6047 -6035 6041 -6034  imp:n=1$ air
box
 6003     1 -0.001155 6000 -6005 6014 -6041 6015 -6018  imp:n=1$ air
box
 6004     1 -0.001155 6000 -6005 6011 -6023 6018 -6025  imp:n=1$ air
box
 6005     1 -0.001155 6000 -6005 6023 -6031 6035 -6028  imp:n=1$ air
box
c
 6006     1 -0.001155 8101 -8102 8305 -6015 6011 -6034  imp:n=1$air box
and DU
 6007     1 -0.001155 8101 -8102 8305 -8310 6034 -8210  imp:n=1$air box
and DU
 6008     1 -0.001155 8101 -8102 8305 -8310 8205 -6011  imp:n=1$air box
and DU
 6009     1 -0.001155 8101 -8102 6028 -8310 6011 -6034  imp:n=1$air box
and DU
c
 6011     1 -0.001155 6004 -6005 9208 -6011 9308 -9309  imp:n=1$air -x
DU and wall
 6012     1 -0.001155 6004 -6005 6011 -6034 6028 -9309  imp:n=1$air -y
DU and wall
 6013     1 -0.001155 6004 -6005 6034 -9209 9308 -9309  imp:n=1$air +x
DU and wall
 6014     1 -0.001155 6004 -6005 6011 -6034 9308 -6015  imp:n=1$air +y
DU and wall
c
 6021     1 -0.001155 6000 -6004 9208 -8201 9308 -9309  imp:n=1$air -x
DU and wall
 6022     1 -0.001155 6000 -6004 8201 -8206 9308 -8301  imp:n=1$air -y
DU and wall
 6023     1 -0.001155 6000 -6004 8206 -9209 9308 -9309  imp:n=1$air +x
DU and wall
 6024     1 -0.001155 6000 -6004 8201 -8206 8306 -9309  imp:n=1$air +y
DU and wall
c
c
c cells 7000  are reserved for the piping and support structure that
c is not critical to the initial run they are currently used for air
gaps
 7001     1 -0.001155 5018 -9105 9208 -9209 9308 -9309  imp:n=1$air gap
above
 7002     1 -0.001155 6005 -5018 9208 -9209 9308 -9309 5020
imp:n=1$air around
c support table
```

```
 7003     1 -0.001155 7103 -7104 -7401 5020  imp:n=1$air inside cutout
of table
 7004     7   -7.99 7103 -7104 7401 7205 -7206 7305 -7306  imp:n=1$
table
 7005     1 -0.001155 7103 -7104 9208 -7205 9308 -9309  imp:n=1$air -x
of table
 7006     1 -0.001155 7103 -7104 7205 -7206 9308 -7305  imp:n=1$air -y
of table
 7007     1 -0.001155 7103 -7104 7206 -9209 9308 -9309  imp:n=1$air +x
of table
 7008     1 -0.001155 7103 -7104 7205 -7206 7306 -9309  imp:n=1$air +y
of table
c air outside legs and steel cylinder for generator
 7009     1 -0.001155 5016 -7103 9208 -9209 9308 -9309 5020 7402 7403 &
             7404 7405 imp:n=1$ air
 7010     1 -0.001155 7102 -5016 9208 -9209 9308 -9309 7402 7403 7404 &
             7405 imp:n=1$ air
 7011     7   -7.99 7102 -7103 -7402 imp:n=1$
 7012     7   -7.99 7102 -7103 -7403 imp:n=1$
 7013     7   -7.99 7102 -7103 -7404 imp:n=1$
 7014     7   -7.99 7102 -7103 -7405 imp:n=1$
c
 7015     1 -0.001155 7101 -7102 7203 -7204 7303 -7304 imp:n=1$
 7016     7   -7.99 7101 -7102 7201 -7203 7301 -7302 imp:n=1$
 7017     7   -7.99 7101 -7102 7203 -7204 7301 -7303 imp:n=1$
 7018     7   -7.99 7101 -7102 7204 -7202 7301 -7302 imp:n=1$
 7019     7   -7.99 7101 -7102 7203 -7204 7304 -7302 imp:n=1$
 7020     1 -0.001155 7101 -7102 9208 -7201 9308 -9309 imp:n=1$
 7021     1 -0.001155 7101 -7102 7201 -7202 9308 -7301 imp:n=1$
 7022     1 -0.001155 7101 -7102 7202 -9209 9308 -9309 imp:n=1$
 7023     1 -0.001155 7101 -7102 7201 -7202 7302 -9309 imp:n=1$
c cells 8000 describe the DU reflector boxes
c
c cells 01-04 compose the bottom right box of DU decreasing
c distance from the center
 8001     2 -18.95116 8101 -8102 8205 -8206 8301 -8302  imp:n=1$xx
 8002     2 -18.95116 8101 -8102 8205 -8206 8302 -8303  imp:n=1$xx
 8003     2 -18.95116 8101 -8102 8205 -8206 8303 -8304  imp:n=1$xx
 8004     2 -18.95116 8101 -8102 8205 -8206 8304 -8305  imp:n=1$xx
c cells 05-08 compose the top left box of DU decreasing distance from
center
 8005     2 -18.95116 8101 -8102 8201 -8210 -8306 8307  imp:n=1$xx
 8006     2 -18.95116 8101 -8102 8201 -8210 -8307 8308  imp:n=1$xx
 8007     2 -18.95116 8101 -8102 8201 -8210 -8308 8309  imp:n=1$xx
 8008     2 -18.95116 8101 -8102 8201 -8210 -8309 8310  imp:n=1$xx
c cells 11-14 Compose the bottom left box of DU decreasing distance
from center
 8011     2 -18.95116 8101 -8102 8201 -8202 8301 -8310  imp:n=1$xx
 8012     2 -18.95116 8101 -8102 8202 -8203 8301 -8310  imp:n=1$xx
 8013     2 -18.95116 8101 -8102 8203 -8204 8301 -8310  imp:n=1$xx
 8014     2 -18.95116 8101 -8102 8204 -8205 8301 -8310  imp:n=1$xx
c cells 15-18 compose the top light box of DU decreasing distance from
center
```

```
 8015     2 -18.95116 8101 -8102 -8206 8207 8305 -8306  imp:n=1$xx
 8016     2 -18.95116 8101 -8102 -8207 8208 8305 -8306  imp:n=1$xx
 8017     2 -18.95116 8101 -8102 -8208 8209 8305 -8306  imp:n=1$xx
 8018     2 -18.95116 8101 -8102 -8209 8210 8305 -8306  imp:n=1$xx
c
c
c
c
c
c Cells 9000 describe the outer shield layers
c Cells 91xx describe z layer shields, 92xx x shield, 93xx y shield
 9001     3   -1.01 9201 9301 -9216 -9316 9101 -9102  imp:n=1$xx
 9002     3   -1.01 9201 9301 -9216 -9316 9102 -9103  imp:n=2$xx
 9003     3   -1.01 9201 9301 -9216 -9316 9103 -9104  imp:n=4$xx
 9004     3   -1.01 9201 9301 -9216 -9316 9105 -9106  imp:n=8$xx
 9005     3   -1.01 9201 9301 -9216 -9316 9106 -9107  imp:n=16$xx
 9006     3   -1.01 9201 9301 -9216 -9316 9107 -9108  imp:n=16$xx
 9007     7   -7.99 9201 9301 -9216 -9316 9108 -9109  imp:n=16$xx
 9008     4   -0.95 9201 9301 -9216 -9316 9109 -9110  imp:n=32$xx
 9009     4   -0.95 9201 9301 -9216 -9316 9110 -9111  imp:n=32$xx
 9010     4   -0.95 9201 9301 -9216 -9316 9111 -9112  imp:n=32$xx
c
 9101     3   -1.01 9104 -9105 9207 -9209 9307 -9308 imp:n=1$
 9201     3   -1.01 9104 -9105 9206 -9210 9306 -9307 imp:n=2$
 9301     3   -1.01 9104 -9105 9205 -9211 9305 -9306 imp:n=4$
 9401     7   -7.99 9104 -9105 9204 -9212 9304 -9305 imp:n=8$
 9501     4   -0.95 9104 -9105 9203 -9213 9303 -9304 imp:n=16$
 9601     4   -0.95 9104 -9105 9202 -9214 9302 -9303 imp:n=32$
 9701     4   -0.95 9104 -9105 9201 -9215 9301 -9302 imp:n=32$
c
 9102     3   -1.01 9104 -9105 9207 -9208 9308 -9310 imp:n=1$
 9202     3   -1.01 9104 -9105 9206 -9207 9307 -9311 imp:n=2$
 9302     3   -1.01 9104 -9105 9205 -9206 9306 -9312 imp:n=4$
 9402     7   -7.99 9104 -9105 9204 -9205 9305 -9313 imp:n=8$
 9502     4   -0.95 9104 -9105 9203 -9204 9304 -9314 imp:n=16$
 9602     4   -0.95 9104 -9105 9202 -9203 9303 -9315 imp:n=32$
 9702     4   -0.95 9104 -9105 9201 -9202 9302 -9316 imp:n=32$
c
c
 9103     3   -1.01 9104 -9105 9208 -9210 9309 -9310 imp:n=1$
 9203     3   -1.01 9104 -9105 9207 -9211 9310 -9311 imp:n=2$
 9303     3   -1.01 9104 -9105 9206 -9212 9311 -9312 imp:n=4$
 9403     7   -7.99 9104 -9105 9205 -9213 9312 -9313 imp:n=8$
 9503     4   -0.95 9104 -9105 9204 -9214 9313 -9314 imp:n=16$
 9603     4   -0.95 9104 -9105 9203 -9215 9314 -9315 imp:n=32$
 9703     4   -0.95 9104 -9105 9202 -9216 9315 -9316 imp:n=32$
c
c
 9104     3   -1.01 9104 -9105 9209 -9210 9307 -9309 imp:n=1$
 9204     3   -1.01 9104 -9105 9210 -9211 9306 -9310 imp:n=2$
 9304     3   -1.01 9104 -9105 9211 -9212 9305 -9311 imp:n=4$
 9404     7   -7.99 9104 -9105 9212 -9213 9304 -9312 imp:n=8$
 9504     4   -0.95 9104 -9105 9213 -9214 9303 -9313 imp:n=16$
```

```
 9604     4   -0.95 9104 -9105 9214 -9215 9302 -9314 imp:n=32$
 9704     4   -0.95 9104 -9105 9215 -9216 9301 -9315 imp:n=32$
c
c
c
 9999     0         -9101 :9112 :-9201 :9216 :-9301 :9316 IMP:N=0
c

c
c Surfaces
c The Origin for the system is located at the Apex/base of the TiCu V
c target in the neutron generator.
c
c
 1000        py -22.2125
 1001        py -22.1363
 1002        py -21.9295
 1003        py -21.8533
 1004        py -21.6465
 1005        py -21.5703
 1006        py -21.3635
 1007        py -21.2873
 1008        py -21.0805
[…]
c
c surfaces in the 2000 series are used to model the various
experiments.
c We will conduct irradiations under 3 different configurations.
c
c I can't find accurate information on the shape of the bottle. The cap
c is 28mm long. I've decide to model the bottle as 2 cylinders stacked
on
c top of each other. Based on the cap dimensions and assumed
c interior dimensions, I'm assuming the convex bit starts 4.8 cm
c from the top, effects should be minimal
c
 2001        pz 4.45  $ glass exterior/poly cut
 2002        pz 4.75  $ glass interior/foil base
 2003        pz 8.25  $ foil top
 2004        pz 10.15  $ convex
 2005        pz 14.95  $ bottle top
c
c For case 1: position 1 is on axis with generator (y) halfway into
block
c in the x direction; position c 2 is half way into the remaining poly
c block on y axis.
c
 2011       c/z -15.24 3.81 2.85  $ poly hole in position 1
 2012       c/z -15.24 3.81 2.8  $ bottle exterior position 1
 2013       c/z -15.24 3.81 2.5  $ Bottle interior assuming 3 mm thick
pos 1
 2014       c/z -15.24 3.81 2.7  $ Bottle cap exterior position 1
 2015       c/z -15.24 3.81 2.4  $ bottle cap interior position 1
```

```
c
 2021       c/z -15.24 11.33 2.85  $ poly hole in position 2
 2022       c/z -15.24 11.33 2.8  $ bottle exterior position 2
 2023       c/z -15.24 11.33 2.5  $ Bottle interior 3 mm thick pos 2
 2024       c/z -15.24 11.33 2.7  $ Bottle cap exterior position 2
 2025       c/z -15.24 11.33 2.4  $ bottle cap interior position 2
c
c
 2031       c/z -15.24 18.95 2.85  $ poly hole in position 2
 2032       c/z -15.24 18.95 2.8  $ bottle exterior position 2
 2033       c/z -15.24 18.95 2.5  $ Bottle interior 3 mm thick pos 2
 2034       c/z -15.24 18.95 2.7  $ Bottle cap exterior position 2
 2035       c/z -15.24 18.95 2.4  $ bottle cap interior position 2
c
c
 2041       c/z -15.24 -3.81 2.85  $ poly hole in position 2
 2042       c/z -15.24 -3.81 2.8  $ bottle exterior position 2
 2043       c/z -15.24 -3.81 2.5  $ Bottle interior 3 mm thick pos 2
 2044       c/z -15.24 -3.81 2.7  $ Bottle cap exterior position 2
 2045       c/z -15.24 -3.81 2.4  $ bottle cap interior position 2
c
c cylinders for foils 2100 is the first cylinder and filled with argon,
2102
c is the first foil cylinder the cylinders then alternate a .017 cm
radial
c increase for the lithium foil, .0127cm radial increase c for the
argon gap.
c The turn number and circumfence are listed on each foil, total
circumfence
c @ end. The cylinders contain slightly too much lithium so a section
of outer
c ring is removed to correct
 2100       c/z -15.24 3.81 0.15875  $
 2101       c/z -15.24 3.81 0.17575  $    0    1.10
 2102       c/z -15.24 3.81 0.18845  $
 2103       c/z -15.24 3.81 0.20545  $    1    1.29
 2104       c/z -15.24 3.81 0.21815  $
 2105       c/z -15.24 3.81 0.23515  $    2    1.48
 2106       c/z -15.24 3.81 0.24785  $
 […]
c
c
 3000        py 22.3141
 3001        py 22.2379
 3002        py 22.1337
 3003        py 22.0575
 3004        py 21.9533
 3005        py 21.8771
 3006        py 21.7729
 3007        py 21.6967
 3008        py 21.5925
[…]
```

```
c
c Surfaces in group 5000 are used for the neutron generator tube.
c Group 7000 is reserved for supporting
c structures such as the mangentron and piping.
c the following surfaces are used for the Copper target. For the
initial
c run the target is reduced to a capital V wedge with corners at
c (.97,+/-2.86,0),(2.445,+/-2.86,11.21) for the outer R plane
c (-.97,+/-2.86,0),(-2.445,+/-2.86,11.21) for the outer L plane,
c the inner corners are at (0,+/-2.86, 1.83),(1.215,+/-2.86,11.21)
c for inner R plane, (0,+/-2.86, 1.83),(-1.215,+/-2.86,11.21)
c for the inner L plane. A 4 mil layer of Ti coats the interior face of
c the wedge this has not been included for the initial run.
c The target also appears to beveled, this was not included to simpilfy
c the model due to initial time constraints
 5001        pz 0.000001  $base of the accelerator target
 5002        pz 11.21  $Top of the target provides bounding side
 5003        py -2.86  $-Y limit of target provides bounding side
 5004        py 2.86  $+Y limit of target provides bounding side
c
c the equations for the planes follow in cells 4005-4008. This is a
c likely place for sign errors on D
c
 5005         p 64.1212 0 8.437 -62.1297  $L outer plane
 5006         p 53.6536 0 6.9498 12.718134  $L inner plane
 5007         p -53.6536 0 6.9498 12.718134  $R inner plane
 5008         p -64.1212 0 8.437 -62.1297  $R outer plane
c
 5009        pz 1.83  $Height int V, apex provides bouding side for
Source
c
 5010        pz -1.55  $ base of copper disc beneath wedge
 5011        cz 4.3815  $ Aluminum Cylinder containing the wedge
 5012        cz 4.6815  $ Aluminum Cylinder exterior (.118 in thick)
 5013        pz 14.54  $ Top of aluminum cylinder
 5014        pz 14.84  $ Top of aluminum cylinder
 5015        pz -37.73  $ Base of Steel cylinder containing Neutron
generator
 5016        pz -38.03  $ Base of steel cylinder disc
 5017        pz 19.64  $ Top of cylinder containing the Neutron
generator
 5018        pz 19.94  $ Top of cylinder disc replace with joint in 2.0
 5019        cz 7.315  $ Interior of SS cylinder containing neutron
generator
 5020        cz 7.62  $ exterior of S cylinder containing neutron
generator
c
c
c
c Surfaces in group 6000 are used for the boxes and air gaps Surfaces
c in 6000 are used to define the
c sheet containing boxes and the Z limits.
c They are also used to define the air gaps between cells
```

```
c
 6000        pz -14.18  $Exterior Base of box
 6001        pz -13.54  $Interior Base of box
 6002        pz -13.29  $Base of sheets
 6003        pz 14.65  $Top of sheets
 6004        pz 16.3  $Interior Top of boxes
 6005        pz 16.94  $Exterior Top of boxes7
c
 6011        px -22.735  $Exterior -x of box 1
 6012        px -22.4175  $Interior -x of box 1
 6013        px 7.1775  $Interior +x of box 1
 6014        px 7.495  $Exterior +x of box 1
 6015        py -22.735  $Exterior -y of box 1
 6016        py -22.4175  $Interior -y of box 1
 6017        py -8.0625  $Interior +y of box 1
 6018        py -7.745  $Exterior +y of box 1
c
c
 6021        px -22.735  $Exterior -x of box2
 6022        px -22.4175  $Interior -x of box2
 6023        px -7.745  $Exterior +x of box2
 6024        px -8.0625  $Interior +x of box2
 6025        py -7.495  $Exterior -y of box2
 6026        py -7.1775  $Interior -y of box2
 6027        py 22.4175  $Interior +y of box2
 6028        py 22.735  $Exterior +y of box2
c
 6031        px -7.495  $Exterior -x of box 3
 6032        px -7.1775  $Interior -x of box 3
 6033        px 22.4175  $Interior +x of box 3
 6034        px 22.735  $Exterior +x of box 3
 6035        py 7.745  $Exterior -y of box 3
 6036        py 8.0625  $Interior -y of box 3
 6037        py 22.4175  $Interior +y of box 3
 6038        py 22.735  $Exterior +y of box 3
c
 6041        px 7.745  $Exterior -x of box4
 6042        px 8.0625  $Interior -x of box4
 6043        px 22.4175  $Interior +x of box4
 6044        px 22.735  $Exterior +x of box4
 6045        py -22.735  $Exterior -y of box4
 6046        py -22.4175  $Interior -y of box4
 6047        py 7.495  $Interior +y of box4
 6048        py 7.1775  $Exterior +y of box4
c
c
c surfaces in group 7000 are used for the support structures at the
c moment this is limited to the 4 legs and 2 frames
 7101        pz -60.6  $ 68.58base of bottom support frame
 7102        pz -59.64  $ 67.63top of support frame/bottom of legs
 7103        pz -15.45  $ 22.67top of $ylinder/base of top support
 7104        pz -14.18  $ 21.40top of support base/base of DU boxes
c
```

```
c
 7201        px -26.67  $ left ext. side of base support
 7202        px 26.67  $ right ext. side of base support
 7203        px -17.78  $ left int. side of base support
 7204        px 17.78  $ right int. side of base support
c
 7205        px -29.21  $ left side of top support
 7206        px 29.21  $ Right side of top support
c
c
 7301        py -26.67  $left ext. side of base support
 7302        py 26.67  $right ext. side of base support
 7303        py -17.78  $left int. side of base support
 7304        py 17.78  $right int. side of base support
c
 7305        py -29.21  $left side of top support
 7306        py 29.21  $Right side of top support
c
c
 7401        cz 15.24  $cut out on top support D=30.48
 7402       c/z -21.59 -21.59 3.81  $-x -y leg
 7403       c/z -21.59 21.59 3.81  $-x +y leg
 7404       c/z 21.59 -21.59 3.81  $+x -y leg
 7405       c/z 21.59 21.59 3.81  $+x +y leg
c
c surfaces in group in 8000 are used for the DU reflectors
c each reflector is 53.09cm x 7.37cm x 30.48 cm
 8101        pz -14.18  $Top of support base/base of DU boxes
 8102        pz 16.3  $Top of DU Boxes
c
 8201        px -30.355  $lt outer box edge limit
 8202        px -28.5125  $
 8203        px -26.67  $
 8204        px -24.8275  $
 8205        px -22.985  $lt inner box edge limit
 8206        px 30.355  $Rt outer box edge limit
 8207        px 28.5125  $
 8208        px 26.67  $
 8209        px 24.8275  $
 8210        px 22.985  $Rt inner box edge limit
c
 8301        py -30.355  $lt outer box edge limit
 8302        py -28.5125  $
 8303        py -26.67  $
 8304        py -24.8275  $
 8305        py -22.985  $lt inner box edge limit
 8306        py 30.355  $Rt outer box edge limit
 8307        py 28.5125  $
 8308        py 26.67  $
 8309        py 24.8275  $
 8310        py 22.985  $Rt inner box edge limit
c
c
```

```
c surfaces in group 9000 are used to construct the exterior shielding
c layers and the particle kill box. c 91xx is for Z, 92xx for x, 93xx
for y
c
c Z-plane surfaces. 3 layers of shielding below 7 above
c
c
c
 9101        pz -68.22  $base of bottom shield
 9102        pz -65.68  $
 9103        pz -63.14  $
 9104        pz -60.6  $
 9105        pz 61.32  $start of top shielding
 9106        pz 63.86  $
 9107        pz 66.4  $
 9108        pz 68.94  $
 9109        pz 71.48  $
 9110        pz 74.02  $
 9111        pz 76.56  $
 9112        pz 79.1  $
c
c
c X plane surfaces 7 layers on each side, outermost is at 48.26 cm.
c each layer of shield in 2.54cm thi$k
 9201        px -48.26  $
 9202        px -45.72  $
 9203        px -43.18  $
 9204        px -40.64  $
 9205        px -38.1  $
 9206        px -35.56  $
 9207        px -33.02  $
 9208        px -30.48  $
 9209        px 30.48  $
 9210        px 33.02  $
 9211        px 35.56  $
 9212        px 38.1  $
 9213        px 40.64  $
 9214        px 43.18  $
 9215        px 45.72  $
 9216        px 48.26  $
c
c
c Y plane surfaces 7 layers on each side, outermost is at 48.26 cm.
c each layer of shield in 2.54cm thi$k
 9301        py -48.26  $
 9302        py -45.72  $
 9303        py -43.18  $
 9304        py -40.64  $
 9305        py -38.1  $
 9306        py -35.56  $
 9307        py -33.02  $
 9308        py -30.48  $
 9309        py 30.48  $
```

```
 9310        py 33.02  $
 9311        py 35.56  $
 9312        py 38.1  $
 9313        py 40.64  $
 9314        py 43.18  $
 9315        py 45.72  $
 9316        py 48.26  $
c

c material card
c kcode 2000 .27 20 2000 $ kcode term
mode  n
nps 10000000
c
m1    6000.         -0.000124  $ Air, dry (near sea level from PNNL) C
weight
      7014.         -0.755268 8016.         -0.231781 18000.        -
0.012827
c
m2    92234.          -5e-006  $depleted uranium WFs from PNNL handbook
      92235.          -0.0025 92238.        -0.997495
c
m3    1001.          -0.13653  $ H WF 1.01 g/cc 5% borated poly
      5010.           -0.0099 5011.           -0.0401 6000.          -
0.81347
c
m4    1001.         -0.143716  $H WF in Poly (PNNL handbook) density
      6000.         -0.856284
c
m5    3006.           -0.0759  $elemental Li
      3007.           -0.9241
c
m6    18000.               -1  $ Elemental Argon
c
m7    6000.           -0.0041  $ C  WF of SS 316 from PNNL handbook
      14000.         -0.00507 15031.         -0.00023 16000.         -
0.00015
      24000.            -0.17 25055.         -0.01014 26000.
-0.669
      28000.            -0.12 42000.           -0.025
c
c manufactor Borosilicate glass is
c 81% SiO2, 13% B2O3, 4% Na2O, 2% Al2O3 -> 211 O, 81Si, 26B, 8Na, 4A
m8    5010.            0.0156  $ natural B adjusted B-10 atom fraction
      5011.         0.0631879 8016.          0.639394 11023.
0.024242
      13027.         0.021212 14000.         0.245455
c
m9    29000.               -1  $ Elemental Cu
c
m10   1002.               -1  $ Density at 2 mTorr at 35 C is
4.192x10^-10 g/cm
c
```

```
m11   13027.              -1  $ Elemental aluminum
c
f14:n 2101 2103 2105 2107 2109 2111 2113 2115 2117 2119 2121 2123 2125
2127
      2129 2131 2133 2135 2137 2139 2141 2143 2145 2147 2149 2151 2153
2155
      2157 2159 2161 2163 2165 2167 2169 2171 2173 2175 2177 2179 2181
2183
      2185 2187 2189 2191 2193 2195 2197 2199 2201 2203 T
Fm14     (1 5 (105:91))
f24:n 2101 2103 2105 2107 2109 2111 2113 2115 2117 2119 2121 2123 2125
2127
      2129 2131 2133 2135 2137 2139 2141 2143 2145 2147 2149 2151 2153
2155
      2157 2159 2161 2163 2165 2167 2169 2171 2173 2175 2177 2179 2181
2183
      2185 2187 2189 2191 2193 2195 2197 2199 2201 2203 T
Fm24     (-1 5 (105:91))
f34:n 2101 2103 2105 2107 2109 2111 2113 2115 2117 2119 2121 2123 2125
2127
      2129 2131 2133 2135 2137 2139 2141 2143 2145 2147 2149 2151 2153
2155
      2157 2159 2161 2163 2165 2167 2169 2171 2173 2175 2177 2179 2181
2183
      2185 2187 2189 2191 2193 2195 2197 2199 2201 2203 T
c SOURCE DEFINITION
c source is an isotropic volumetric source inside cell 5001,
c mono energetic E=2.45 MeV
c A rectuangular parallelepiped (box) envelops the cell and
c points are randomally selected inside the
c box. They are only accepted as source points IFF they lie inside cell
5001
sdef X=d1 Y=d2 Z=d3 ERG=2.45 CEL=5001
c
si1 -1.215 +1.215      $ x-range limits for the box
sp1 0      1            $ uniform probability over the x range
c
si2 -2.86  +2.86        $ y-range limits for the box
sp2 0      1            $ uniform probability over the y range
c
si3 0      +11.21       $ Z-range limits for the box
sp3 0      1            $ uniform probability over the Z range
```

APPENDIX B

ADDITIONAL ACTIVATION WIRE SPECTRA

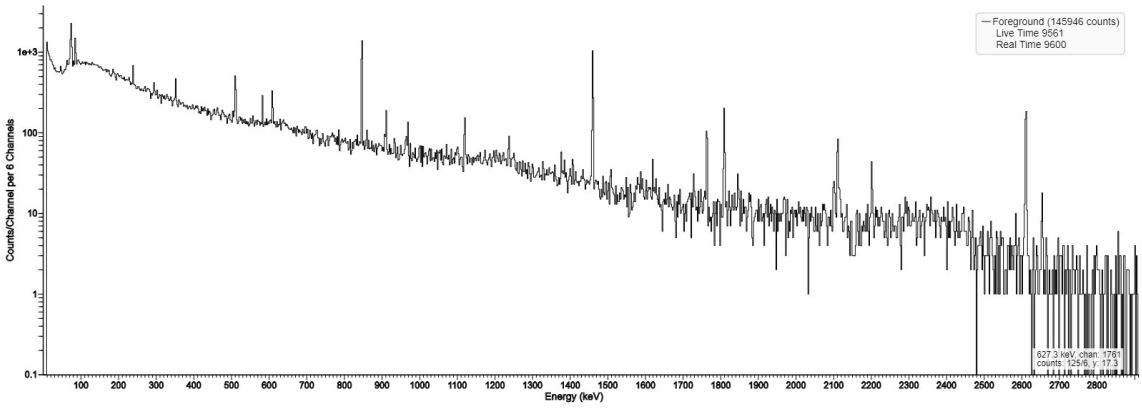

Figure B.1 12-04-2017 ^{152}Eu Energy and Efficiency Calibration

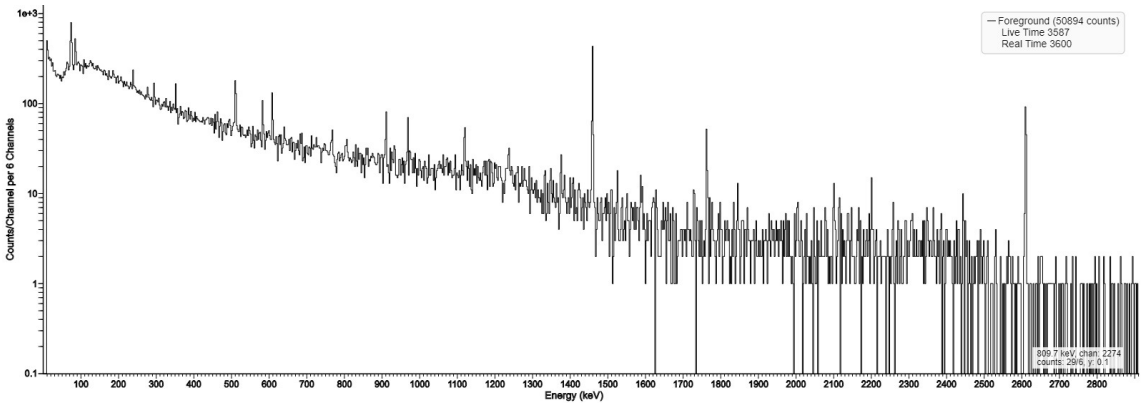

Figure B.2 12-05-2017 Background

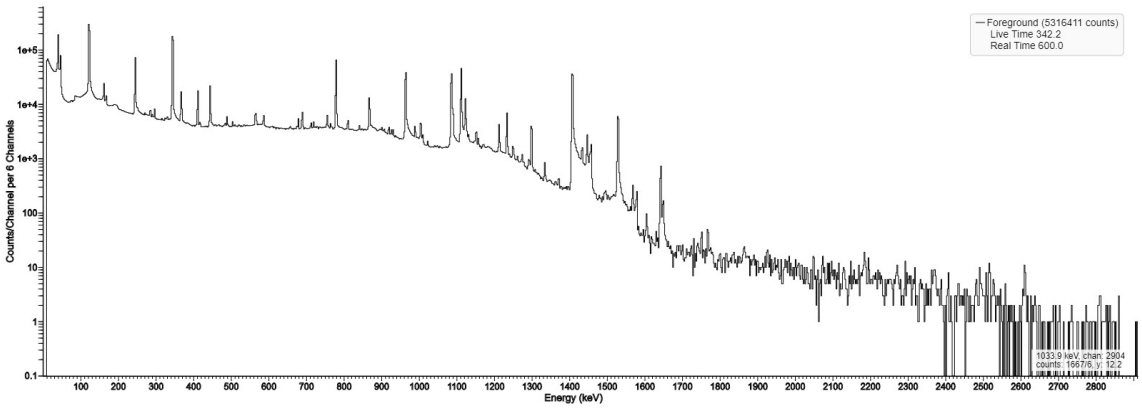

Figure B.4 12-05-2017 Morning ^{152}Eu Calibration

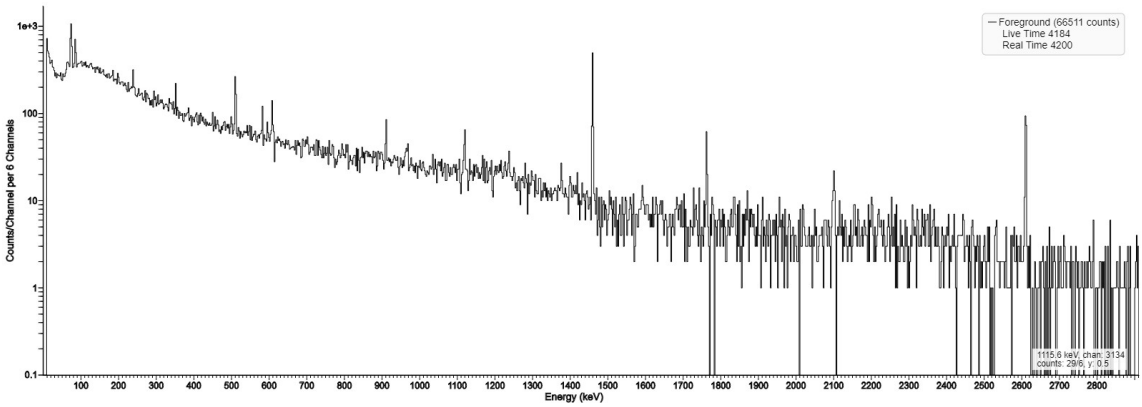

Figure B.5 12-05-2017 Al wire

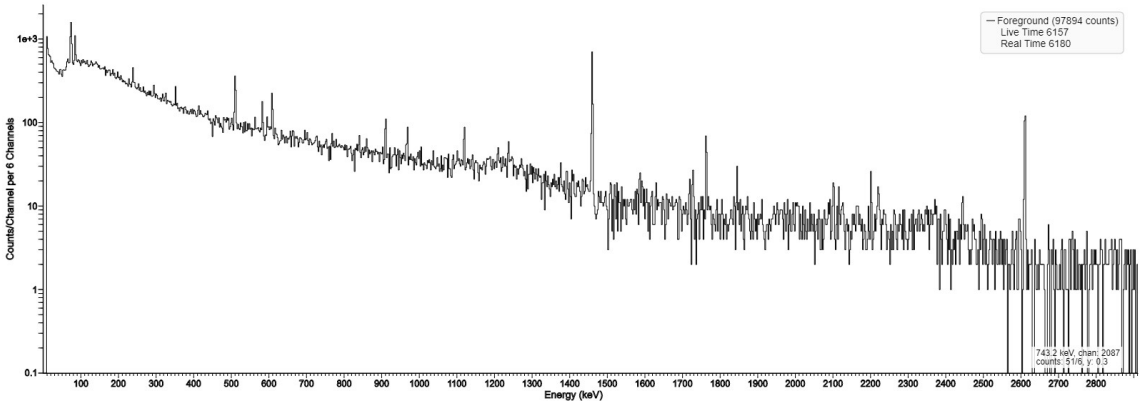

Figure B.6 12-05-2017 Co wire

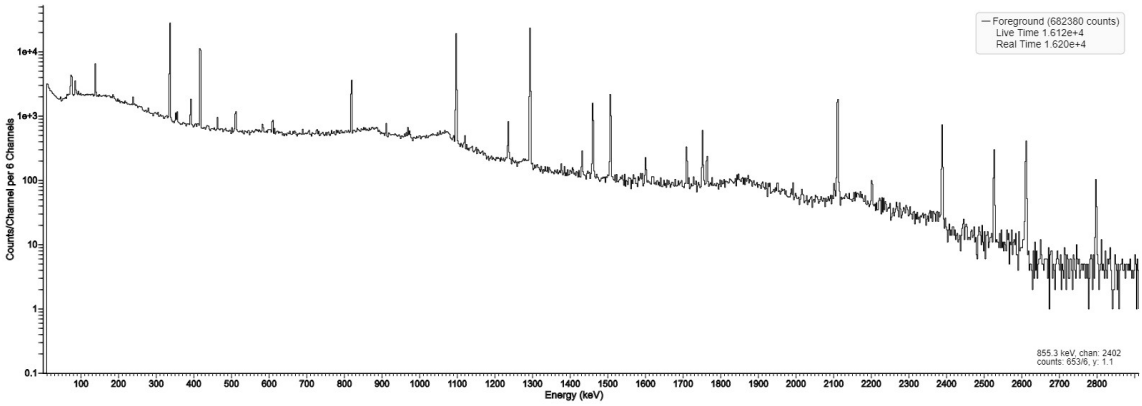

Figure B.7 12-05-2017 In wire

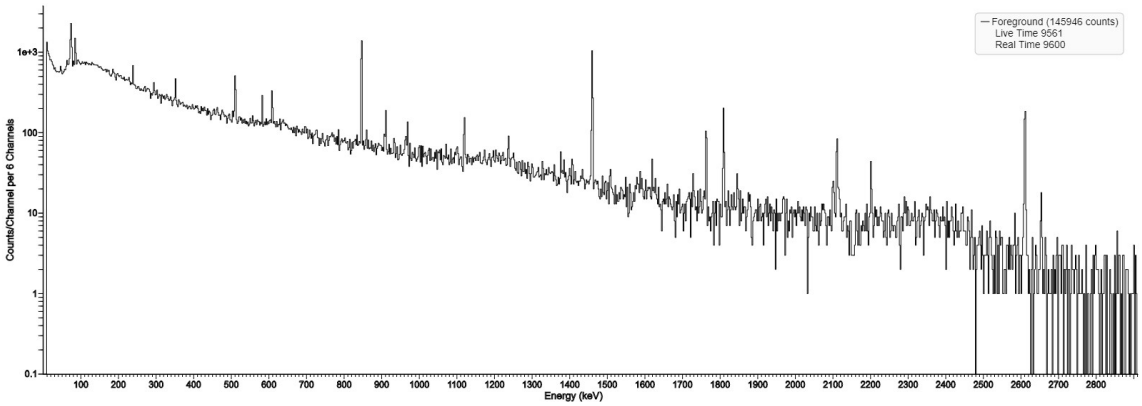

Figure B.8 12-05-2017 Mn & Dy wire

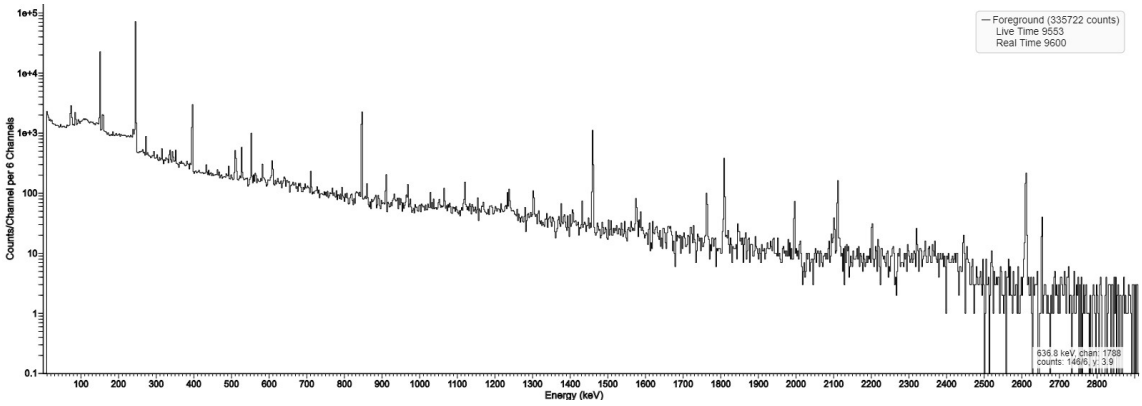

Figure B.9 12-05-2017 Mn & Dy(Cd) wires

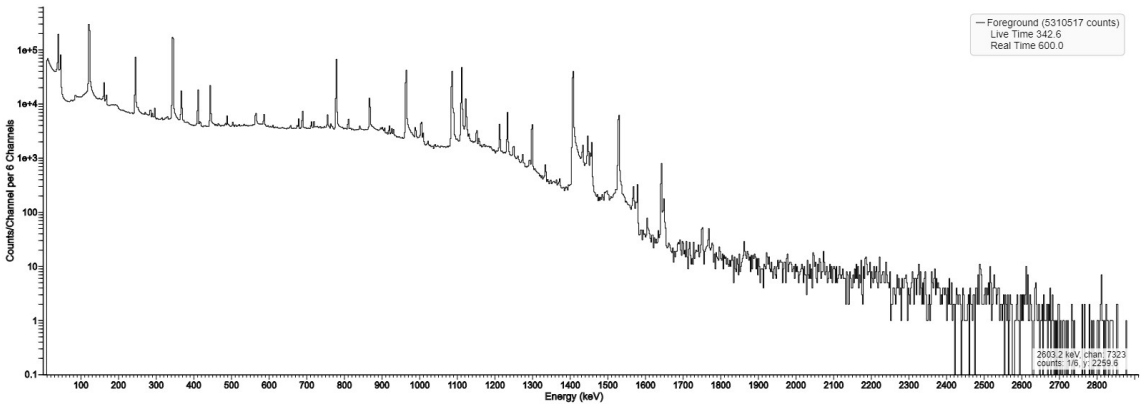

Figure B.10 12-06-2017 Calibration

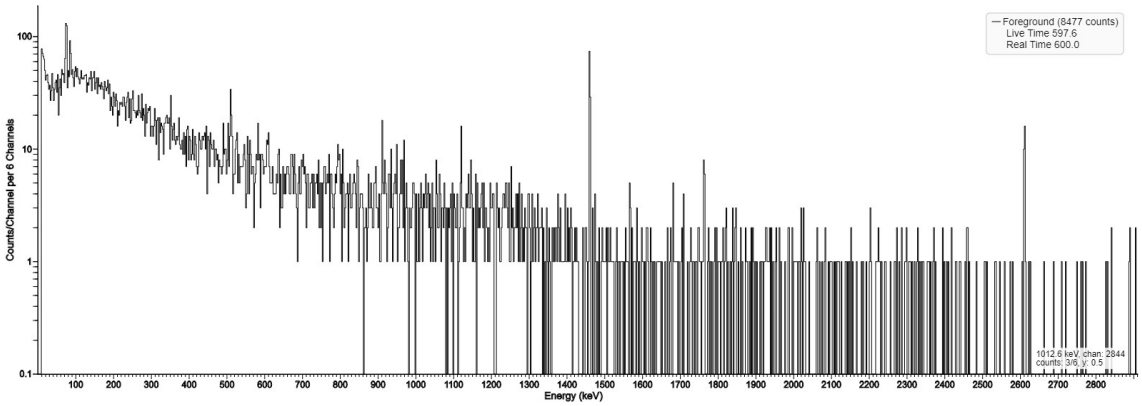

Figure B.11 12-06-2017 Background

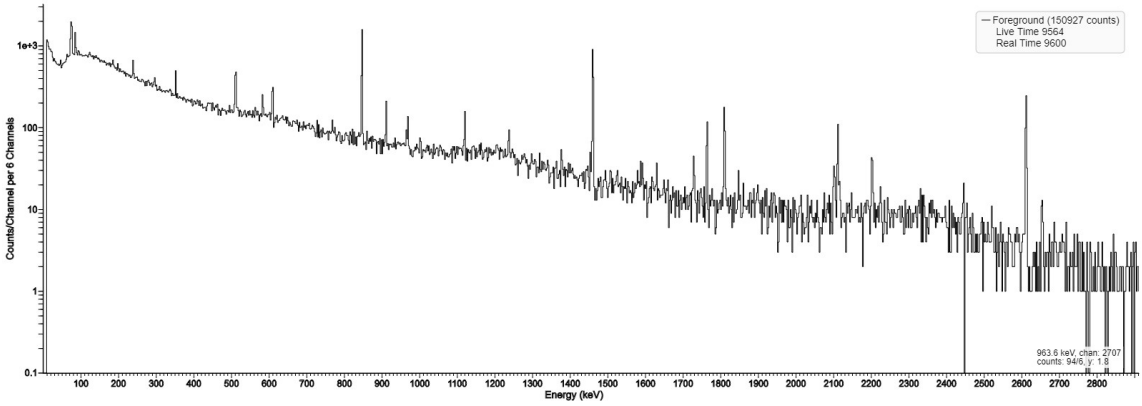

Figure B.12 12-06-2017 Mn & Dy wires

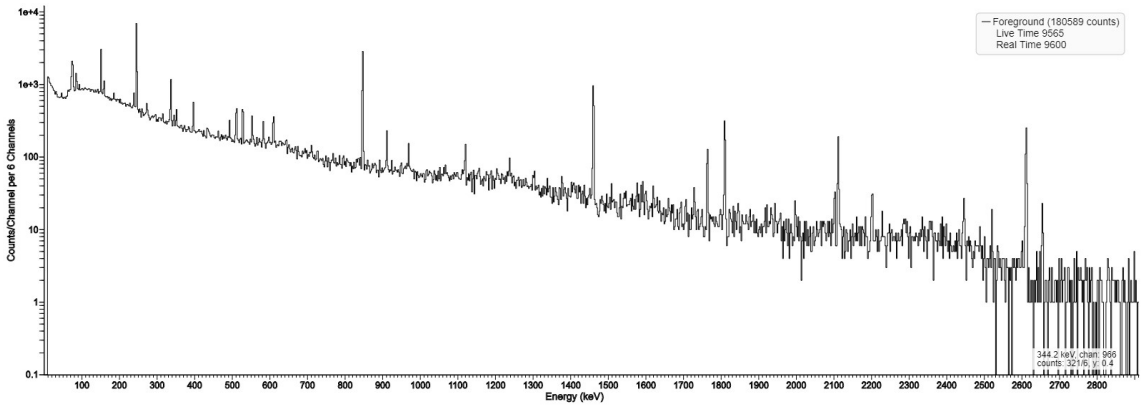

Figure B.13 12-06-2017 Mn & Dy(Cd) wires

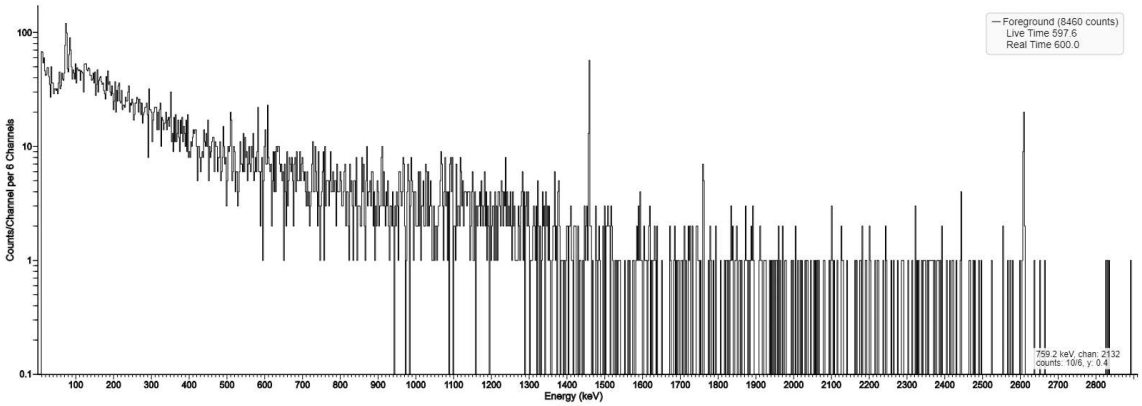

Figure B.14 12-12-2017 Background

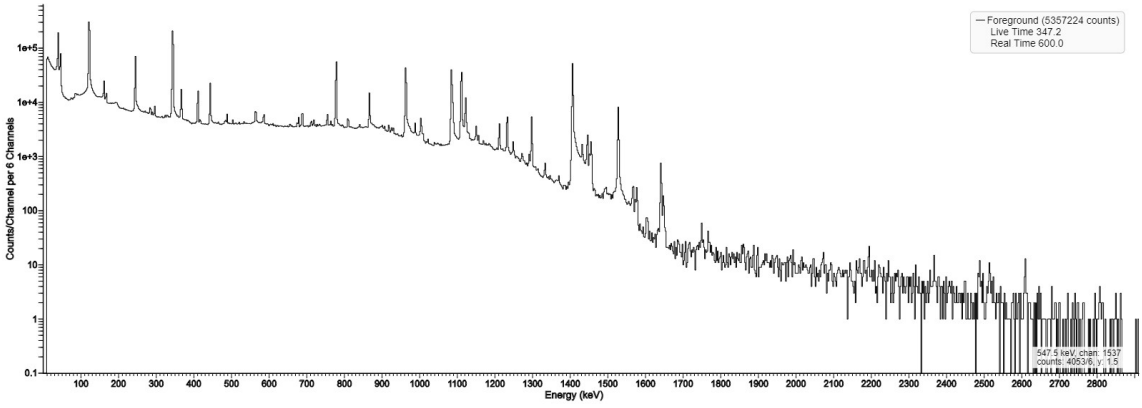

Figure B.15 12-12-2017 Calibration

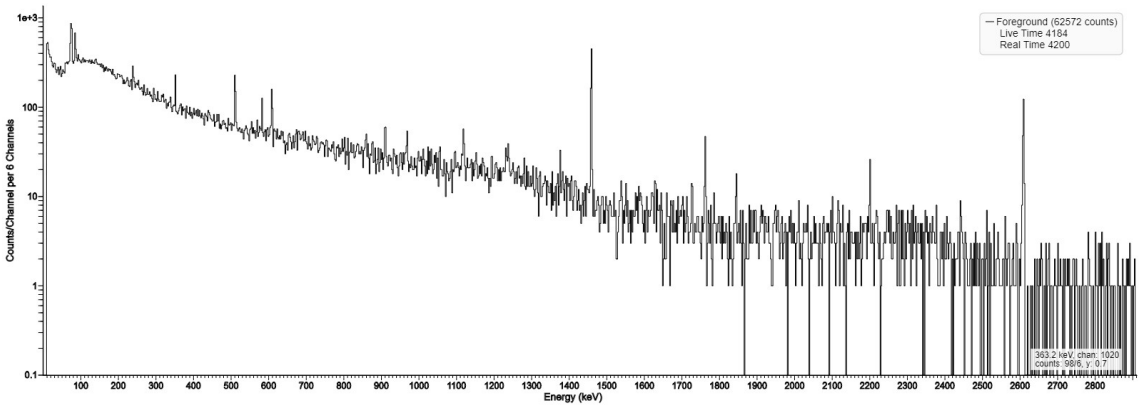

Figure B.16 12-12-2017 Al wire

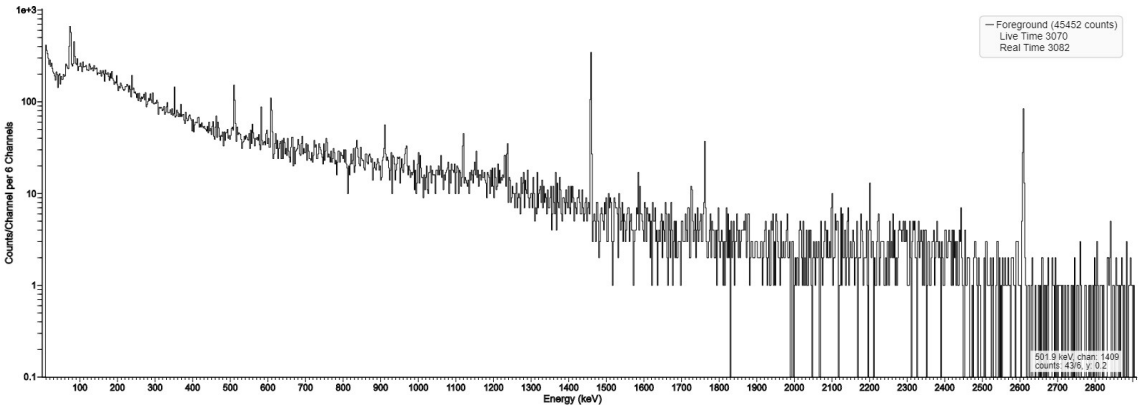

Figure B.17 12-12-2017 Co wire

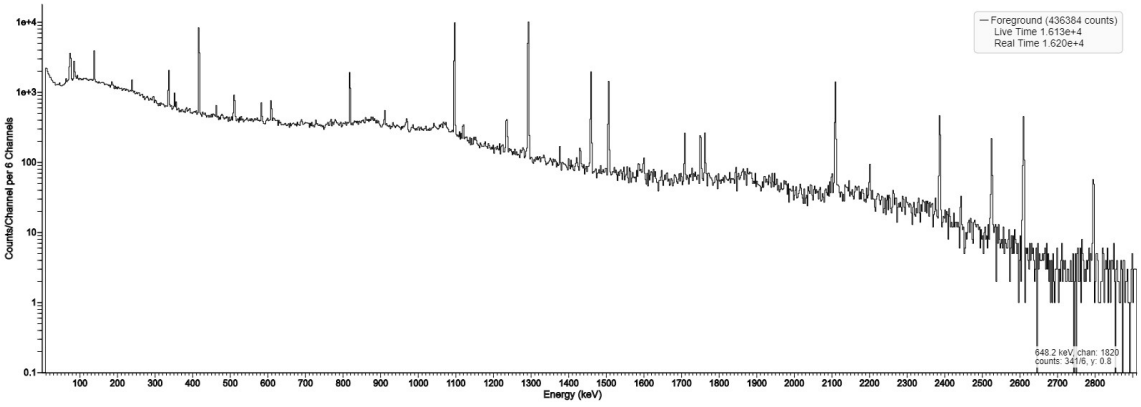

Figure B.18 12-12-2017 In Wire

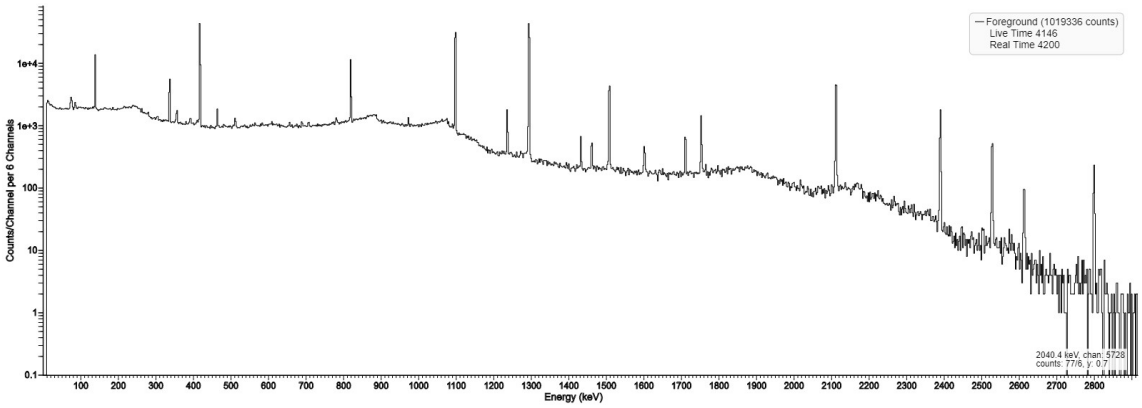

Figure B.19 2-15-2018 Al & In wires (4200 s)

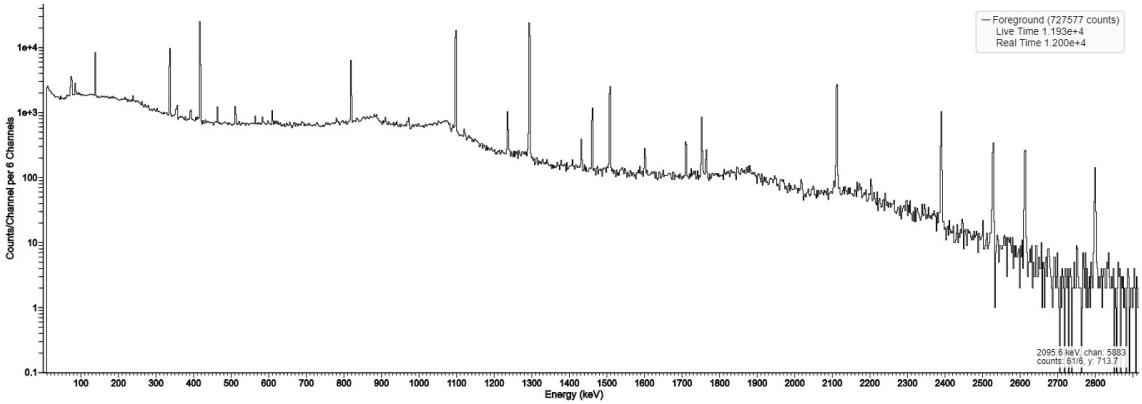

Figure B.20 2-15-2018 Al & In wires (16200 s)

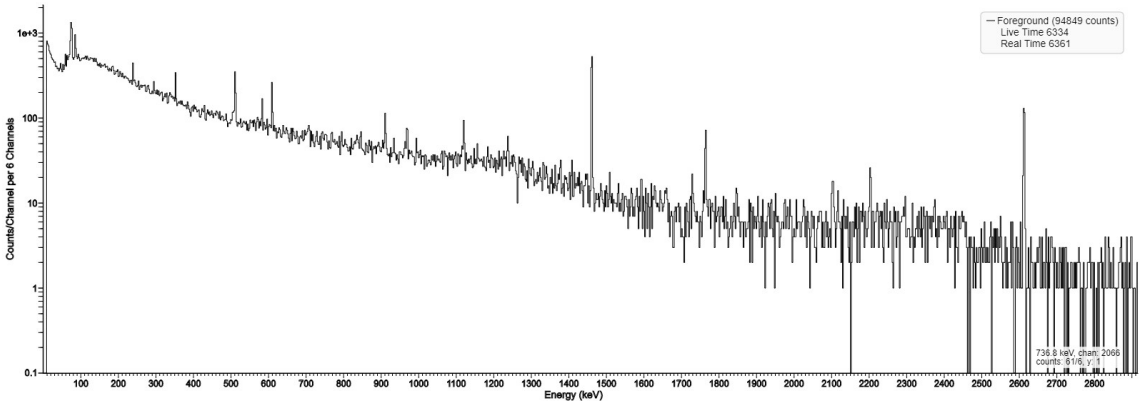

Figure B.21 2-15-2018 Co wire

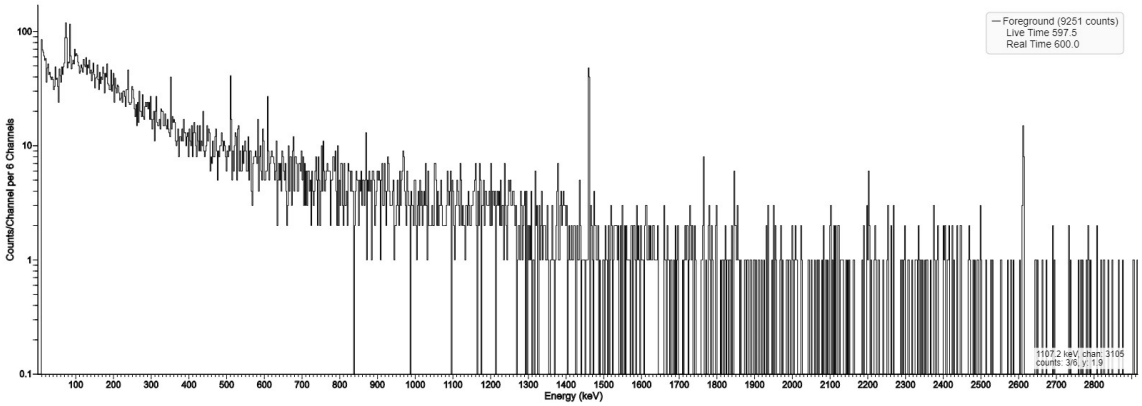

Figure B.22 2-23-2018 Background

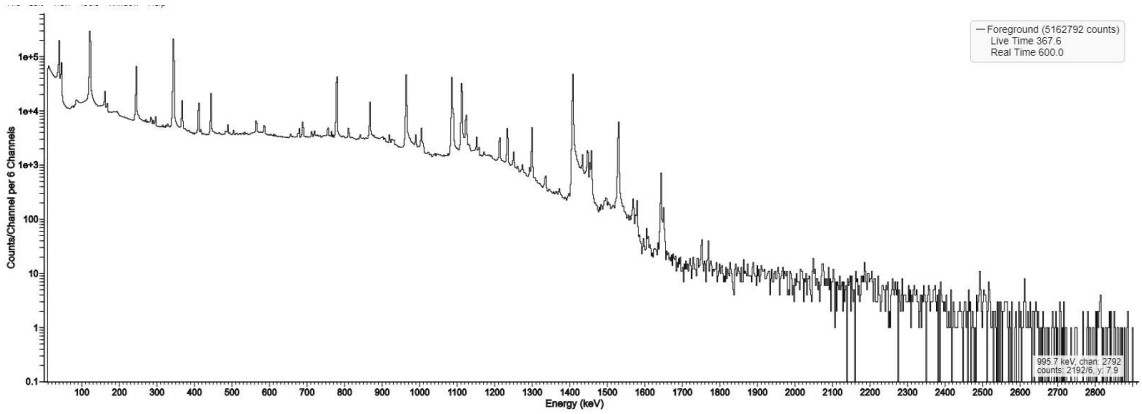

Figure B.23 2-23-2018 Calibration

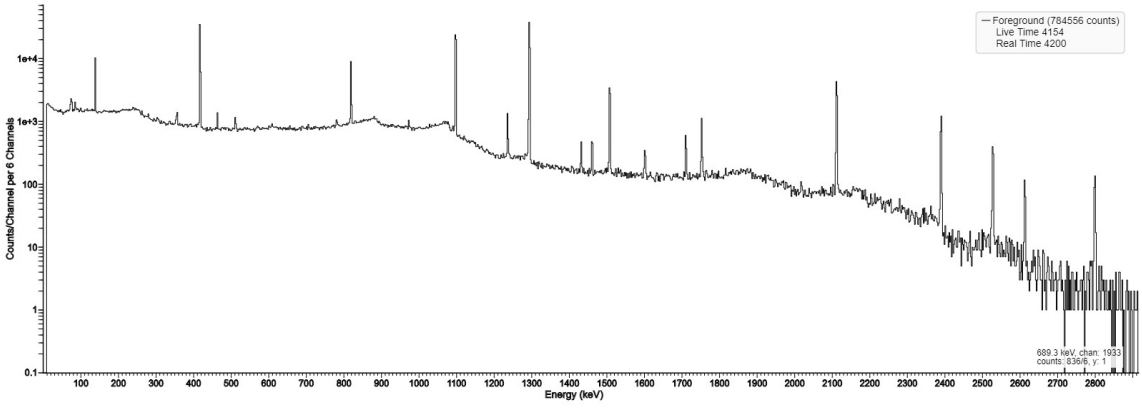

Figure B.24 2-23-2018 Al & In wires (4200 s)

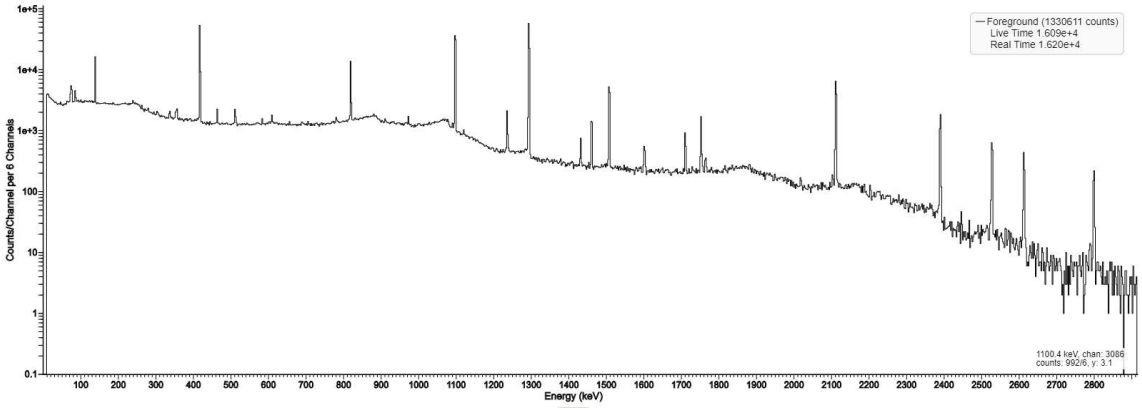

Figure B.25 2-23-2018 Al & In wires (16200 s)

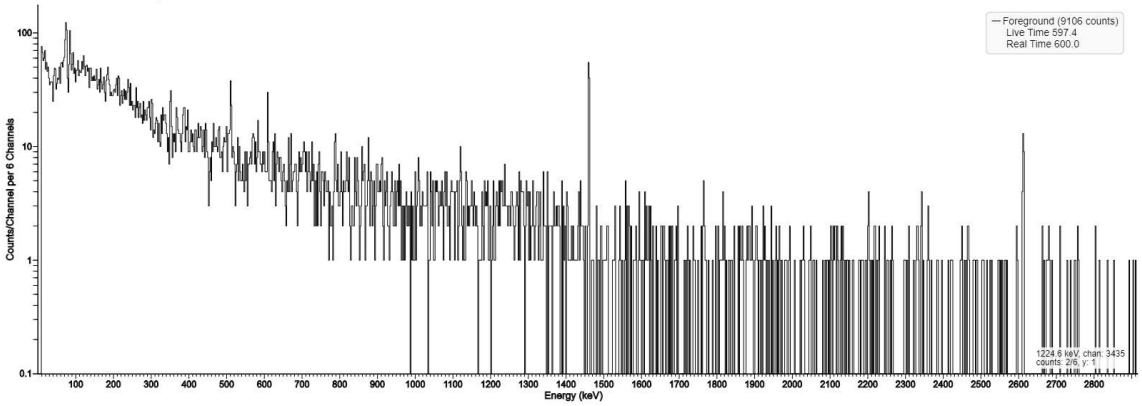

Figure B.26 2-26-2018 Background

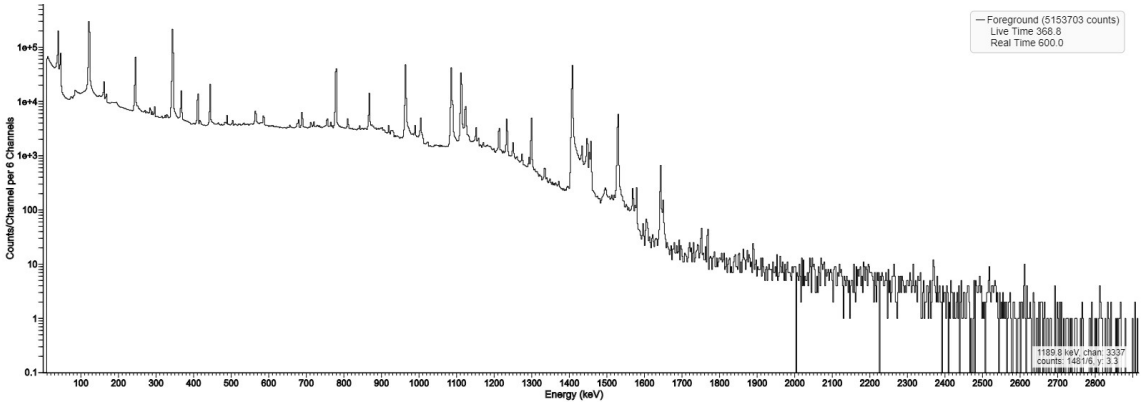

Figure B.27 2-26-2018 Calibration

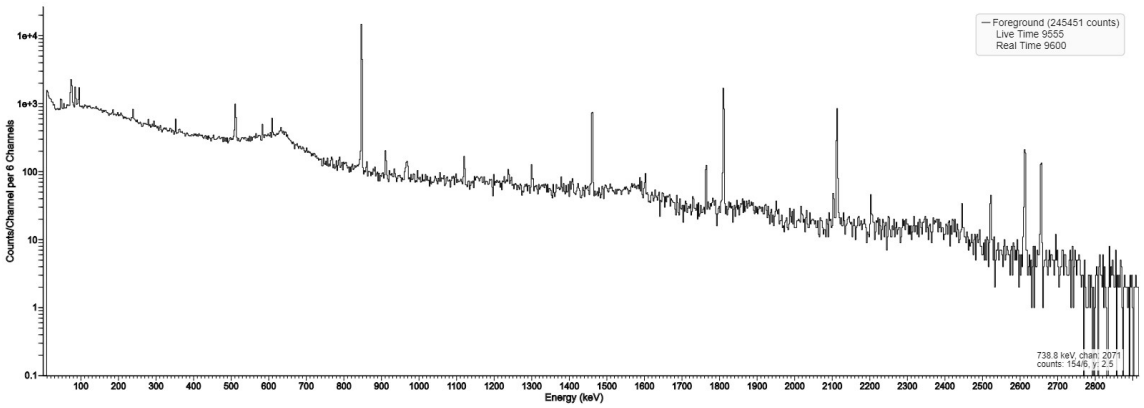

Figure B.28 2-26-2018 Mn & Dy wires

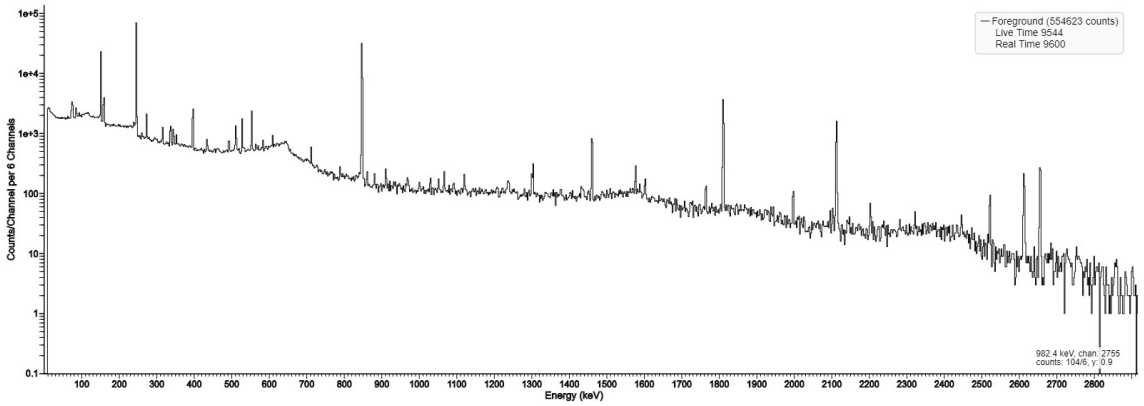

Figure B.29 2-26-2018 Mn & Dy(Cd) wires